UNIVERSIDAD DE GUANAJUATO

DIVISIÓN DE INGENIERÍAS
CAMPUS IRAPUATO-SALAMANCA

"Brain Tumor Tissue Segmentation in Multimodal Images"

Tesis Profesional

QUE PARA OBTENER EL GRADO DE:
DOCTOR EN INGENIERÍA ELECTRICA

PRESENTA:
Elisée Ilunga Mbuyamba

ASESORES:
Dr. Juan Gabriel Aviña Cervantes
Dr. Claire Chalopin

Salamanca Guanajuato Agosto 2017

Dedication

I dedicate my dissertation work to my dear wife Arlette Mbelu Mukendi and our children, Daniella Mbelu Ilunga and Rayan Mukendi Ilunga. Their love and presence are all in my life.

Acknowledgements

I would like to thank my advisors Juan Gabriel Aviña Cervantes from the University of Guanajuato, Engeering Division of the Irapuato-Salamanca Campus for his academic guidance and Doctor Claire Chalopin from the Innovation Center Computer Assisted Surgery of the University of Leipzig, in Germany, for giving me the opportunity to understand the application of image processing in the neurosurgical area. I also want to thank Doctor Dirk Lindner from University Hospital, department of Neurosurgery, Universität Leipzig in Germany for his support to this work.

I also wish to thank my family, my mother Therese Mbelu wa Mpoyi; my brothers and sisters, who never ceased to encourage me. Although he is no longer in this world, my father Charles Mbuyamba was a model, a good guide and a great motivation for me to go further in my studies. I express sincere gratitude to my father in law and mother in law, Patrice Mukendi and Laurianne Mujinga for all they do for us.

Furthermore, I have to thank Dr. Jean Fulbert Ituna Yudonago for the opportunity he gave me to study at the University of Guanajuato. In the same way, I am thankful to Dr. Bernad Ndaye and Dr. Simon Kidiamboko for their support. Even if he is no longer between us, I am very grateful to my professor Augustin Luaba Nfunayi for all he did for me.

My wife Arlette Mbelu Mukendi and our children, Daniella Mbelu Ilunga and Rayan Mukendi Ilunga deserve a big gratitude for their support during this long separation. They have always believed in me, and they are the reason of my success.

Institutional Acknowledgements

I express my sincere gratitude to the University of Guanajuato, in particularity the Engineering Division of the Irapuato-Salamanca Campus for the formation and the support that I received. All of my professors deserve my gratefulness for their huge work during these two years allowing me to obtain the master degree. In the same way, I also wish to thank the DAIP (Direccion de Apoyo a la Investigacion y al Posgrado) for its financial support.

This work has been supported by the National Council of Science and Technology of Mexico (CONACyT) under the grant number 493442. Here we want to express our gratefulness for the funding received.

I would like to thank the Innovation Center Computer Assisted Surgery, University of Leipzig, for the acceptance to work within its laboratories and to make available the database for the researches.

Contents

List of Figures

List of Tables

Abstract

Brain tumor is one of the main cause of death in the world. Its possible treatment consists in a surgery performed by neurosurgeons who open the skull (called craniotomy) for removing abnormal cells. After tumor resection, patients benefit of improved survival and life quality. Multimodal images, preoperative Magnetic Resonance Imaging (MRI) and intraoperative Ultrasound (iUS) data, are in general used to support this complex surgical operation. Preoperative images allow the tumor diagnosis and the surgery planning. Intraoperative data provide an update in the visualization of the brain during the operation and enable the control of resection. Indeed, geometrical parameters like tumor volume, position and distance to risk structures are needed for the success of the surgery. Thus, the detection and extraction of tumorous tissues are important. In this work, the brain tumor segmentation in multimodal images is addressed. Tumorous tissue extraction consists in three main stages. First, alternative methods for brain tumor segmentation in MRI are proposed. Second, the tumor delineation in iUS using a patient specifc MR tumor model is suggested. Third, an approach based on the fusion of intraoperative B-mode and contrast-Enhanced Ultrasound (CEUS) data is suggested for detection of tumor residuals in iUS.

Chapter 1

General introduction

This first chapter presents the basic concepts related to the brain tumor resection, and used in imaging assisted diagnosis and surgery. These concepts include some medical definitions and an overview of the brain tumor surgery context. Indeed, the problematic of brain tumor tissue segmentation in medical applications is described. Then, the goal of this study with its applications in clinical setting is clearly presented. The originality of methodologies used for segmenting brain tumor in magnetic resonance imaging and ultrasound data is highlighted. The similarity measures employed for supporting the claims of this work, the quantitative evaluation and the materials involved are described. Finally, the structure of the manuscript is presented.

1.1 Brain tumor surgery context

1.1.1 Definitions

- Tumor: a mass of tissue that grows out of control of the normal forces that regulates growth [2]. Tumors can be benign or malignant (cancerous).
- Metastasis: according to the Nactional Cancer Institut (NCI) dictionary, in metastasis, cancer cells break away from the original (primary) tumor, travel through the blood or lymph system, and form a new tumor in other organs or tissues of the body. The new, metastatic tumor is the same type of cancer as the primary tumor.
- Glioblastoma: also known as glioblastoma multiforme (GBM), is the most common and most aggressive primary brain tumor [3]. And, according to the NCI, the GBM is a fast-growing type of central nervous system tumor that forms from glial (supportive) tissue of the brain and spinal cord and has cells that look very different from normal cells.

1.1.2 Background

Patients with brain tumors benefit of improved survival after surgical resection of the tumor. This complex operation is in general supported by multimodal images including preoperative (MRI) and intraoperative (iUS) data in order to reach optimal results. An adequate medical decision for the treatment planning depends on the diagnosis performed before the surgery and based on MRI data. Intraoperative ultrasound images provide an update representation of the current state of the tumor during the surgery.

1.2 Problems and research topic

1.2.1 Preoperative MR data

Geometrical parameters like tumor volume, position and distance to risk structures are needed to plan the operation. These parameters are qualitatively assessed in the preoperative MR data in clinical routine. Specially, the tumor volume is employed to analyze quantitatively the tumor and to study its growth over a period of time. It is extracted by segmentation approaches. Hence, the accuracy of this task is required in clinical setting in order to have reliable results that will lead to an adequate medical decision or treatment. Although the manual tracing of human organs or tissues by experts has been accepted as ground truth in medicine, the increasing of the patient datasets turns this practice in a less recommendable routine [4]. Faced with a big MR images database, the manual tumor delineations performed by neurosurgeons or radiologists suffer of the subjectivity of visual perception, errors caused by the tiredness and it is a time-consuming task. Due to this, the automatic segmentation methods are needed and they are selected according their capabilities to achieve results more similar to those obtained by experts.

1.2.2 Intraoperative US data

Medical image processing on US images is in general a difficult task and still under improvement because of the low signal noise ratio. Thus, the identification of tumor boundary and detection of tumor residuals are complex in the intraoperative ultrasound data. In the context of brain tumor surgery, residual tumors are still a problem for neurosurgeons. Due to the invasiveness of the treatment and the fact that tumor remnant cells are potential sources of new tumor growth; the removal of the maximum quantity of these abnormal cells is important to save lives. Therefore, after initial resection, the tissue analysis is fundamental for supporting the physician decision about the presence or absence of residual tumor cells. Furthermore, at this stage, the big problem for physician is the differentiation of residual tumors from other hyperechogenic structures, such as blood vessels.

1.3 Aims and motivations

The goal of this work can be split in three major steps. the development and optimization of segmentation methods to automatically extract brain tumor tissue in the preoperative MR data. Second, the implementation of an intraoperative technique using a specific patient MRI model-based for US brain tumor segmentation. Third, the study and implementation of a tissue classification method for the detection of tumor remnants so as to optimize the brain tumor resection.

1.4 Originality and methodology

The originality of this work consists in providing alternative methods for brain tumor tissue segmentation in MR data. Moreover, in iUS, there is no work on the automatic identification of brain tumor boundary and tumor residuals in the literature. In the context of brain tumor surgery, the proposed methodology for brain tumor tissue segmentation in multimodal images can be grouped and described by the following three key points.

1.4.1 MRI brain tumor segmentation

Alternative approaches for MR brain tumor segmentation using active contour models (ACM) based on region and edge information were proposed. First, a Localized Active Contour Model (region-based technique) integrating an additional step of background intensity compensation was presented [1]. This localized active contour model was automatically initialized via the hierarchical centroid shape descriptor that we employed for tumor localization in [5]. Finally, in the edge-based technique, a snake energy-minimization type approach based on a nature-inspired optimization (cuckoo search strategy) method was introduced [6].

1.4.2 US brain tumor segmentation

Specific patient model from MRI will was used for brain tumor segmentation in intraoperative ultrasound images. The tumor model is obtained from preoperative MRI by using a semi-automatic technique. Indeed, the method consisted of registering the model with the 3D-iUS data due to the brain tissue deformation. The transformation in the registration stage will be based on image gradients.

1.4.3 Identification of residual brain tumors

The development of a medical image-processing tool to support surgeons with the identification of residual brain tumor based on both 3D iB-mode and 3D-iCEUS (Contrast-Enhanced Ultrasound) imaging was addressed. This approach consisted in extracting relevant information from both iB-mode and CEUS modalities using automatic segmentation techniques. And, the extracted structures were fused according to proposed rules to keep only the residuals of tumor.

1.5 Materials and metrics

Two databases were considered in this work. First, an image database of patients with different kind of tumors collected at the Department of Neurosurgery at the University Hospital of Leipzig, Germany in the context of a previous research project funded by the German Research Society (Deutsche Forschungsgemeinschaft) and accepted by the ethics commission of the University of Leipzig was available. Tumor operations were guided by using a neuronavigation system (SonoNavigator, Localite, Sankt Augustin, Germany) including an AplioXG ultrasound device (Toshiba Medical Systems Europe, Zoetermeer, Netherland) with 2D ultrasound transducers that were tracked using an optical tracking system. Then, 3D ultrasound volumes were reconstructed from the 2D slices by the neuronavigation system. These volumes, the 3D iB-mode and 3D iCEUS data, were acquired before and at the end of brain tumor operations. In the original 2D ultrasound images, the pixel size is 0.422 $mm\times$ 0.422 mm and the voxel size of the reconstructed 3D volumes is $1\times1\times1$ mm^3.

Second, the database known as MICCAI 2012 Challenge on Multimodal Brain Tumor Segmentation Benchmark organized by B. Menze, A. Jakab, S. Bauer, M. Reyes, M. Prastawa, and K. Van Leemput (`http://www.imm.dtu.dk/projects/BRATS2012`, [7]) was used in this work. This challenge contains real data, simulated data and their gold standards (ground truths). It includes several MR image modalities such as T1, T2, T1C and FLAIR. The parameters T1 and T2 are relaxation times that enable to discriminate some body tissues and highlight a specific target. The T1C

(T1 contrast-enhanced MRI) and T2 modalities enhances the visualization of the tumor while the edema is better visualized in the T2 and FLAIR (Fluid-Attenuated Inversion-Recovery) modalities. Several works use two or three of these MRI data. In [8] the authors showed that T1C, T2 and FLAIR are the useful modalities for tumor and edema segmentation.

The quantitative evaluation was performed by using metrics such as: Jaccard index (J), Dice index (D), Hausdorff distance (d_H), sensitivity (Sen), specificity (Spe), accuracy (Acc), area under the ROC curve (AUC) [9], error rate (Err) or percentage of wrong classifications [10] and overlap ($Overlap$).

The perfect segmentation is obtained when the measures J, D, Sen, $Spe \in [0,1]$ are equal to 1 and d_H achieves the 0 value. Moreover, a sensitivity value of 1 means that all pixels belonging to the tumor region in the ground truth are correctly detected in the test image. Likewise, a specificity value of 1 indicates that none pixel of the healthy tissue according to the ground truth is misclassified as tumorous tissue in the test image. The metrics used are defined as follows:

$$J = \frac{|A \cap B|}{|A \cup B|}, \tag{1.1}$$

$$D = \frac{2|A \cap B|}{|A| + |B|}, \tag{1.2}$$

$$Overlap = \frac{|A \cap B|}{min(|A|, |B|)}, \tag{1.3}$$

$$d_{\mathrm{H}} = \max\left\{ \max_{a \in A} \min_{b \in B} \|a - b\|, \max_{b \in B} \min_{a \in A} \|b - a\| \right\}, \tag{1.4}$$

where A is the handwork segmentation result (ground truth or gold standard) and B the automatic obtained contour.

$$Sen = \frac{TP}{TP + FN} \tag{1.5}$$

$$Spe = \frac{TN}{TN + FP} \tag{1.6}$$

$$Acc = \frac{TP + TN}{TP + TN + FP + FN} \tag{1.7}$$

$$AUC = \frac{1}{2}\left(\frac{TN}{TN + FP} + \frac{TP}{TP + FN}\right) \tag{1.8}$$

$$Err = \frac{FP + FN}{TP + TN + FP + FN} \tag{1.9}$$

where TP, TN,FP and FN are:
True Positive (pixels correctly classified as tumorous tissue), True Negative (pixels correctly classified as healthy tissue), False Positive (normal tissue misclassified as tumor region) and False Negative (undetected tumorous tissue), respectively.

1.6 Outline

This thesis is structured in order to allow the understanding of the problems to be addressed, the goals and the motivation of the work, and the proposed methods as expected solution. The results are provided for supporting the claims of the study. This manuscript is organized as follows:

Chapter 1: General introduction
This chapter provides the basic concepts used in the context of brain tumor surgery. In addition, the problems addressed this study, related works to the segmentation of brain tumor in MRI and US images, the goals of the work and the methodology used to achieve the results are presented. The database and metrics used for supporting our claims are described, and follows the structure of the thesis.

Chapter 2: Brain tumor segmentation in preoperative MR data
Brain tumor segmentation by using alternative approaches based on active contour models is presented. First, a Localized Active Contour Model with background intensity compensation applied to MR brain tumor segmentation is proposed. The automatic initialization of ACM via the hierarchical centroid shape descriptor is described. Finally, the active contours driven by Cuckoo Search Strategy for brain tumor images segmentation were introduced.

Chapter 3: Brain tumor segmentation in intraoperative US data
A summary of the brain tumor surgery process is presented in this chapter as well as the functioning of the neuronavigation system. As image-guided surgery has become a standard in medicine, the image registration methods are also described in this chapter to understand how the points on a patient are aligned with those on the preoperative image (MRI).

Chapter 4: Automatic identification of residual brain tumors
In this chapter, an image processing approach is presented for identifying residual brain tumors. The method is based on the fusion of intraoperative 3D B-mode and Contrast-Enhanced Ultrasound Data.

Chapter 5: General conclusions and future perspectives
Finally, this chapter gives the conclusions of the study and the possible future works. Furthermore, it lists also the fruits of this work in term of published papers in conference and journals.

Chapter 2

Brain tumor segmentation in preoperative MR data

2.1 Introduction

This chapter presents proposed segmentation methods and their application on preoperative MR images. These methods are mainly active contour models grouped in two categories, region-based active contour models (RBACM) and edge-based active contour models (EBACM). In the case of RBACM, a Localized Active Contour Model (LACM) integrating an additional step of background intensity compensation is introduced. This technique allows to address the problem of high mean intensity distance between the foreground and background that leads to an incorrect delineation of the target. Images with large black background region, as common in MRI data, are sensitives to this problem. Thus, the aim is to minimize the attraction effect of the active contour model to the undesired borderlines defined by these two mentioned image regions. In addition, the Hierarchical Centroid Shape Descriptor (HCSD) was used for detecting the region of interest i.e. abnormal tissue so as to automatically initialize the active contour. With respect to the edge-based technique, a snake energy-minimization type approach based on a nature-inspired optimization (cuckoo search strategy) method is introduced. This strategy assists the converging of control points towards the global minimum of the energy function, unlike the traditional ACM version which is often trapped in a local minimum.

2.2 Related works

In recent years, many segmentation approaches have been proposed with the goal to develop human-free intervention methods and to improve the result quality achieved by these segmentation techniques. In the case of a brain tumor, the Magnetic Resonance Imaging is used as a standard modality for tissue analysis because it offers the advantage of being a noninvasive technique [11]. They are mainly categorized in five groups: Threshold-based, Edge-based, Region-based, learning-based and energy-based segmentation techniques [12]. One of the powerful image segmentation methods, from the second and fifth groups, the Active Contour Model (ACM) in a parametrical formulation was introduced by Michael Kass et al.[13]. Its energy has to become minimal so as to ensure that the active contour is located on the object boundaries. The energy minimization is achieved by the iterative gradient descent method to solve the Euler equation. Then, a famous global region-based ACM was proposed by Chan and

Vese [14]. It uses image content to find the optimum of an energy function that guides the contour evolution in the separation of regions having different statistical information. Instead of using global image information, Lankton et al. [15] suggested to reformulate the Chan-Vese model and the Yezzi model [16] in localized methods. Likewise, Li et al. [17, 18] introduced a Local Binary Fitting (LBF) model that use a kernel function for embedding local intensity image information. Unlike this previous localized scheme based on mean intensity, Wang et al. [19] modeled the local neighborhood by a Gaussian distribution and their model is called Local Gaussian Distribution Fitting (LGDF). It enables the regions separation based on the mean intensity and variance of the local region.

The segmentation via active contours is an immense area where many efforts have been performed and applied on medical images. In [20], an edge-based active contour model with flexible initialization is presented and it showed its ability of handling images with weak and broken edges. The edge and region-based models have each of them some advantages and drawbacks. For this reason, some models have combined region and edge information for obtaining an improved model [21, 22]. More recently, a two-stage image segmentation method was introduced [23]. This technique associates the advantage of the local and global region fitting energies by performing the segmentation using successively the global and local approaches. Additionally, Zhang and Xie [24] proposed a deformable model based on a gradient convolution field and its divergence (external force) that attracts the contour to the boundary. The global minima is achieved by using convex relaxation in the energy functional minimization problem. This method was tested on a set of 2D and 3D data and, it demonstrated that it can achieve better results on images with intensity inhomogeneity, noise, weak edge, complex geometry and even in the case of arbitrary initializations. Also, a Self-Organizing Active Contour based on region information and region-based ACM based on local and global intensity statistic were presented and tested on medical images in [12] and [25], respectively. In order to reach the global minimization, Wu et al [26] used the Gabor and GLCM (gray level co-occurrence matrix) features for avoiding local minima in the contour evolution toward the target object boundary. Above all, other energies based local image information were employed in models such as: local image fitting [27] and local likelihood image fitting [28]. Where, the first method takes into account only the local means intensity, while the second considers both the local intensity and variance in order to separate distinct regions.

2.3 Contributions

2.3.1 Region-base ACM

In this part of the study, three main contributions have been proposed. First, an alternative scheme for brain tumor detection based on HCSD is introduced. Second, a reformulation of the Localized Mean Separation (LMS) energy of Lankton is proposed in order to improve the accuracy and to reduce the computation time in handling images specially with large black background. The proposed method is called LACM-BIC i.e, Localized Active Contour Model with Background Intensity Compensation. Third, these previous approaches are then integrated in a two stage framework for automatic brain tumor segmentation in MR data. These stages are: (1) use the Hierarchical Centroid Shape Descriptor in order to localize the region of interest (ROI) containing the abnormal target tissue. The tumor is enclosed in a bounding box which allows to reduce the operational image area to focus the algorithm on the target tissue to be

segmented. (2) Apply the active contour technique initialized by the ROI coordinates determined in the first stage for delineating tumorous area. The ACM is initialized by a circle whose its center and radius are the centroid and the sides average of the ROI bounding box, respectively. Compared to the selected state of the art ([18], [19], [15]), the LACM-BIC showed the capability of reaching highest accuracy in a lowest computation time for the brain tumor segmentation.

2.3.2 Edge-based ACM

Regarding the edge-based technique, a snake driven by Cuckoo Search strategy for brain tumor MR images segmentation is proposed. This method deals with the ACM evolution as a functional optimization problem, whose energy contour minimization is solved by using the Multi-population Cuckoo Search Strategy (MCSS). The aim is to find accurately the targeted object edges through a two non-sequential stages algorithm. In the first stage local search spaces (or windows) are set for each control point from the current contour (or initial contour, as the case may be). The second phase consists of placing randomly such control points inside each search window, in order to obtain new ones by the aid of the CS strategy. Moreover, two different search window geometries were considered: Rectangular Shaped Search Windows (RSSW) and Pizza-slice Shaped Search Windows (PSSW).

2.4 Foundations

The Hierarchical Centroid Shape Descriptor and the relevant Active Contour Models are described in this section.

2.4.1 Hierarchical Centroid Shape Descriptor

The HCSD is a shape descriptor for binary images based on centroid coordinates extracted from a binary image. It is extracted recursively by decomposing the image in sub-images [29, 30]. This descriptor uses spatial pixels distribution of a binary image as features and it is based on its decomposition by using the k dimensional tree (kd-tree) algorithm. The centroid coordinates of sub-regions are extracted for each decomposition level. They contain neighborhood information useful for describing an object shape. Furthermore, the descriptor length is $2 \times (2^d - 2)$ where d is the depth of the features extraction process. Fig. 2.1 illustrates how an image decomposition in 4 levels (from 0 to 3) is performed through the kd-tree algorithm. Let I the $M \times N$ binary image with foreground I_f and background I_b, the HCSD is built as follows

1. Read the binary image I and compute its transposed I^T,
2. Calculate for each of them the centroids $C(x_c, y_c)$ at the root level by using the Eq (2.1).

$$x_c = \frac{m_{10}}{m_{00}} \quad , \quad y_c = \frac{m_{01}}{m_{00}} \tag{2.1}$$

   where m_{10}, m_{01} and m_{00} are the first order moment along the x-axis, the first order moment along the y-axis and the area of I_f, respectively. The raw moments

m_{pq} of a digital image with pixel intensities $I(i,j)$ are calculated by

$$m_{pq} = \sum_{i=0}^{M} \sum_{j=0}^{N} i^p j^q I(i,j) \tag{2.2}$$

3. Divide recursively the image in two sub-images based on the centroids by using the lines $x = x_c$ or $y = y_c$ until the desired depth of decomposition is reached. At each consecutive level, the axis of coordinates captured is alternated.

4. Normalize the obtained vector in the range of [-0.5,0.5] where the point 0 corresponds to the centroid of the root level. The negative values are features of the left image part while the positives describe the right side relative to the root level (Fig. (2.1)).

5. Concatenate the features extracted from images I and I^T.

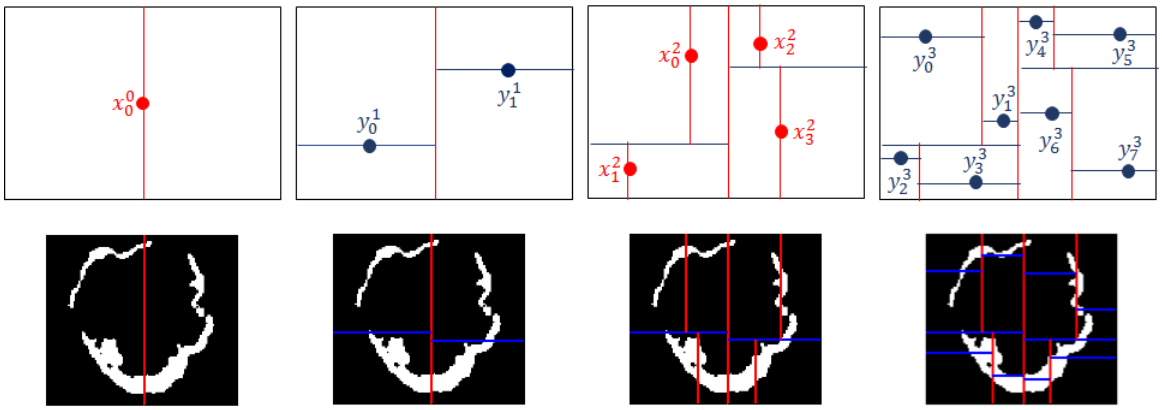

Figure 2.1: *Illustration of the binary image decomposition via the kd-tree structure: from the root level (level 0) to the level 3.*

The vector obtained through the kd-tree decomposition for the previous process is described as

$$v = (x_0^0, y_0^1, y_1^1, x_0^2, x_1^2, x_2^2, x_3^2, y_0^3, y_1^3, \ldots y_7^3) \tag{2.3}$$

where x_0^0 represents the root level coordinate, y_m^n the mth y coordinate at level n and x_m^n the mth x coordinate at level n.

At the root level, a centroid $C(x_0^0, y_0^0)$ is computed from the entire binary image, but only its x_c coordinate is captured ($x_c = x_0^0$) and the image is divided in 2 parts by the line $x = x_0^0$. Then, at the level 1 two centroids are calculated from each divided parts and their y_c coordinates are captured ($y_{c1} = y_0^1$ and $y_{c2} = y_1^1$). This process is performed recursively until to reach the desired depth of decomposition.

2.4.2 Active contour model: Snake

The basic idea of Active Contour Model is the dynamic motion of a parametric curve under the action of certain control forces present in the image spatial domain, [13]. These forces are summarised in two types: internal and external forces. The internal force is responsible of the contour (or snake) smoothness, and the external one of pushing the snake towards the object boundary. According to the above mentioned,

the ACM curve is described by $\mathbf{P}(s,t) = (x(s,t), y(s,t))^T$, where $s \in [0,1]$ and t is the discrete time between two consecutive steps. The cost function is the snake total energy, and its minimum is found when the snake evolves close to the desired contour, it is given by next equation

$$E_{snake} = \int_0^1 (E_{int}(\mathbf{P}(s,t)) + E_{ext}(\mathbf{P}(s,t)))ds, \tag{2.4}$$

since E_{int} and E_{ext} are respectively the internal and external energy terms. They are described as follows,

$$E_{int}(\mathbf{P}(s,t)) = \frac{1}{2}\left[\alpha(s,t)\left\|\frac{\partial \mathbf{P}(s,t)}{\partial s}\right\|^2 + \beta(s,t)\left\|\frac{\partial^2 \mathbf{P}(s,t)}{\partial s^2}\right\|^2\right], \tag{2.5}$$

$$\begin{aligned} E_{ext}(\mathbf{P}(s,t)) =& \gamma_{line}E_{line}(s,t) + \gamma_{edge}E_{edge}(s,t) + \gamma_{term}E_{term}(s,t), \\ =& \gamma_{line}C(s,t) - \gamma_{edge}|\nabla G * I(\mathbf{P}(s,t))|^2 + \gamma_{term}\left.\frac{C_{yy}C_x^2 - 2C_{xy}C_xC_y + C_{xx}C_y^2}{(C_x^2+C_y^2)^{3/2}}\right|_{(s,t)}, \end{aligned} \tag{2.6}$$

where the curve tension is controlled by the elasticity component α, the bending by the rigidity component β and, the external energy by the components γ_{line}, γ_{edge} and γ_{term}. The external energy term is composed by line (E_{line}), edge (E_{edge}) and termination (E_{term}) energy functions, determined using $C(s,t) = G * I(\mathbf{P}(s,t))$ and its first and second order partial derivatives (i.e., C_x, C_y, C_{xx}, C_{xy} and C_{yy}), where G is the Gaussian function and I is the image. The traditional solution of this problem consists on the numerical computing of the Euler equation in (2.7), until the equality is satisfied,

$$\nabla E_{ext} - \alpha(s,t)\frac{\partial^2 \mathbf{P}(s,t)}{\partial s^2} + \beta(s,t)\frac{\partial^4 \mathbf{P}(s,t)}{\partial s^4} = 0 \tag{2.7}$$

This condition corresponds to the minimum energy solution related with the energy stability state. In other words, the external energy component becomes equal to the internal one or *vice versa*.

2.4.3 Chan-Vese model

Chan and Vese (C-V) proposed an active contour model based on region statistical information [14] integrating the simplified Mumford-Shah model [31]. Their energy functional takes into account global statistics and it is written in the level set formulation as:

$$\begin{aligned} E^{C-V}(c_1, c_2, \phi) = \lambda_1 \int_{C_{in}} |I(x) - c_1|^2 H_\epsilon(\phi)dx \\ + \lambda_2 \int_{C_{out}} |I(x) - c_2|^2 (1 - H_\epsilon(\phi))dx \\ + \nu \int |\nabla H(\phi)|dx \end{aligned} \tag{2.8}$$

where c_1 and c_2 are two constants related to the average intensity inside (C_{in}) and

outside (C_{out}) of the contour C, respectively. As well, λ_1, λ_2 and ν are nonnegative parameters. The level set function ϕ [32] and the Heaviside function $H(.)$ [14] are described as follows:

$$\phi(x) = \begin{cases} > 0 & \text{if } x \text{ is inside } C \\ = 0 & \text{if } x \ \in C \\ < 0 & \text{if } x \text{ is outside } C \end{cases}$$

$$H(z) = \begin{cases} 1 & \text{if } z \geq \ 0 \\ 0 & \text{if } z < 0 \end{cases}$$

The derivative of the Heaviside function, called Dirac delta function $\delta(z)$, is defined by the equation:

$$\delta(z) = \frac{d}{dz} H(z) \tag{2.9}$$

With ϵ a positive constant, the implementation of H and δ functions are approximated by

$$H_\epsilon = \frac{1}{2}\left[1 + \frac{2}{\pi}\arctan\left(\frac{\mathrm{x}}{\epsilon}\right)\right] \quad , \quad \delta_\epsilon = \frac{1}{\pi}\frac{\epsilon}{\epsilon^2 + \mathrm{x}^2} \tag{2.10}$$

2.4.4 Mean Separation Energy method

A global image segmentation approach via Coupled Curve Evolution Equations was introduced by Yezzi et al. [16]. Based on the mean intensity for separating regions, it is also called mean separation energy (MS) [15]. This model allows extracting a target object from its surrounding regions based on the maximal mean intensity separation. Yezzi et al. defined their MS energy as

$$E = -\frac{1}{2}\|u - v\|^2 + \alpha \int_C ds \tag{2.11}$$

where $\alpha \geq 0$ and s is the arc length parameter of the curve C. Variables u and v denote the average values of statistics data inside and outside C, respectively.

The gradient flow is computed by the following equation

$$\frac{dC}{dt} = (u - v)\left(\frac{I - u}{A_u} + \frac{I - v}{A_v}\right)\overrightarrow{N} - \alpha k \overrightarrow{N} \tag{2.12}$$

where $\overrightarrow{N}$ ($\overrightarrow{N} = \nabla A_u$), k and I represent the outward unit normal, the signed curvature of C and the image vector, respectively. A_u represents the interior area of the contour C and A_v denotes its exterior area. The average values of statistics data u and v are given by

$$u = \frac{\int_{\Omega_y} H\phi(y) \cdot I(y) dy}{\int_{\Omega_y} H\phi(y) dy} \tag{2.13}$$

and

$$v = \frac{\int_{\Omega_y} (1 - H\phi(y)) \cdot I(y) dy}{\int_{\Omega_y} (1 - H\phi(y)) dy} \tag{2.14}$$

2.4.5 Localizing Region-based Active Contour Model

A well-known framework used for localizing any region-based energy was proposed by Lankton [15]. The use of localized energy enables to overcome the global energy drawbacks that fails in segmentation of images with intensity inhomogeneity and discontinuous boundaries.

Let $I \in \Omega$ a gray level image, such that $\Omega \subset \mathbb{R}^2$ is a 2D image space. The closed contour C is represented here by the zero level set of a signed distance function ϕ, with $C = \{x|\phi(x) = 0\}$. Any region-based energy can be formulated in localized way by this framework as follows:

$$E(\phi) = \int_{\Omega_x} \delta\phi(x) \int_{\Omega_y} B(x,y) \cdot F(I(y), \phi(y)) dy dx + \lambda \int_{\Omega_x} \delta(\phi(x)) ||\nabla\phi(x)|| dx \tag{2.15}$$

where $F(I(y), \phi(y))$ is a generic internal energy measure and $B(x, y)$ represents a characteristic function defining the local region according to a parameter r (radius). The second term aims to penalize the curve arc-length in a weighting defined by the parameter λ.

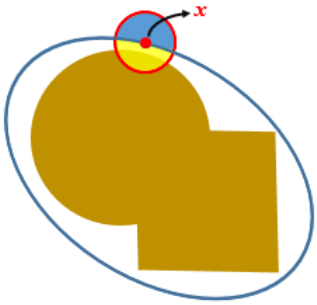

Figure 2.2: *Graphical representation of Localized active contour models.*

The mentioned function $B(x, y)$ is described by the red circle in Fig. 2.2 and the blue curve represents the zero level set function. The blue area depicts the exterior local region whereas the yellow part is the interior local region. A big radius allows embedding more global information while a smaller value takes into account more details. $B(x, y)$ takes the value of 1 when the evaluated points y are located inside of a circle of center x and radius r. It is defined as follows:

$$B(x,y) = \begin{cases} 1, & ||x-y|| < r \\ 0, & \text{otherwise.} \end{cases} \tag{2.16}$$

Finally, the evolution equation is formulated as follows:

$$\frac{\partial\phi}{\partial t}(x) = \delta\phi(x) \int_{\Omega_y} B(x,y) \cdot \nabla\phi(x) \cdot F(I(y), \phi(y)) dy + \lambda\delta(\phi(x)) \text{div}\left(\frac{\nabla\phi(x)}{|\nabla\phi(x)|}\right) \tag{2.17}$$

The proposed method and the materials used in this study are described in the next

section.

2.5 Proposed method I: localized active contour model with background intensity compensation

2.5.1 Patient image dataset

The experiments were carried out on a total of 312 slice images (3 real data: 79 slices and 8 simulated data: 233 slices) from the MICCAI 2012 Challenge database. Tab. 4.1 shows in detail these data. Indeed, an enhanced visualization of the tumor and edema edge or area is achieved by combining the information provided by the multimodal images from this database. However, it is important to note that only T1C and T2 were used here because this study was solely focused on brain tumor segmentation. As the tumorous tissue and edema are highlighted in T2, a low percentage of T2 (defined by κ) is necessary for enhancing the tumor visualization while limiting the increase of edema intensity in T1C. Hence, they were fused by using the following equation

$$I = T1C + \kappa T2 \tag{2.18}$$

In this work a value of $\kappa = 0.2$ was experimentally selected in order to constraint the edema contribution information.

Dataset	N^o Patient	Slices	Total slices
BRATS	1	57 - 100	44
	2	58 - 70	13
	3	79 - 100	22
SimBRATS	4	75 - 105	31
	5	105 -135	31
	6	105 - 130	26
	7	115 -135	21
	8	75 - 110	36
	9	95 - 120	26
	10	80 - 110	31
	11	86 - 116	31
Total	11 cases	—	312

Table 2.1: *Data from MICCAI 2012 Challenge on Multimodal Brain Tumor Segmentation Benchmark used in this work. Patients 4 to 11 correspond to numbers 1, 2, 3, 5, 6, 7, 8, 9 in the SimBRATS.*

2.5.2 Segmentation approach

Let I a given image to segment, I_f its foreground region and I_b its background region. An additive region I_t i.e. $I_t \subset I_f$ is referred as a target region. Fig. 2.3 presents these regions and two possible configurations of the target placement.

The proposed model uses mean intensity for segmenting images. In fact, it is a reformulation of the Lankton MS [15] model in which this study proposes to compensate the background intensity in order to reduce the mean difference between I_f and I_b. The intensity value used for compensation purpose is computed by using Eq. (2.25). When the distance $||E(I_f) - E(I_b)||$ increases (e.g. $||E(I_f) - E(I_b)|| > ||E(I_f) - E(I_t)||$ and $||E(I_f) - E(I_b)|| > ||E(I_b) - E(I_t)||$), the maximal intensity separation is found on

their common boundary. In that case, the extraction of the target fails if it shares the same boundaries with I_f and I_b as depicted in Fig. 2.3(a). There is not a big difference between the results of Lankton MS model with the LACM-BIC when I_t is not close to the borderline of I_f and I_b (Fig. 2.3(b)). However, by compensating the background intensity the attracting force to the foreground-background separation was reduced, and consequently, the active contour is quickly attracted to the desired border and the computation time is reduced. This framework is robust and can handle properly images with these illustrated configurations and magnetic resonance images in general. In addition, the proposed approach is suitable for medical image segmentation that have a high mean intensity distance between the foreground and the background. Generally they have a similar black background like in Fig. 2.3.

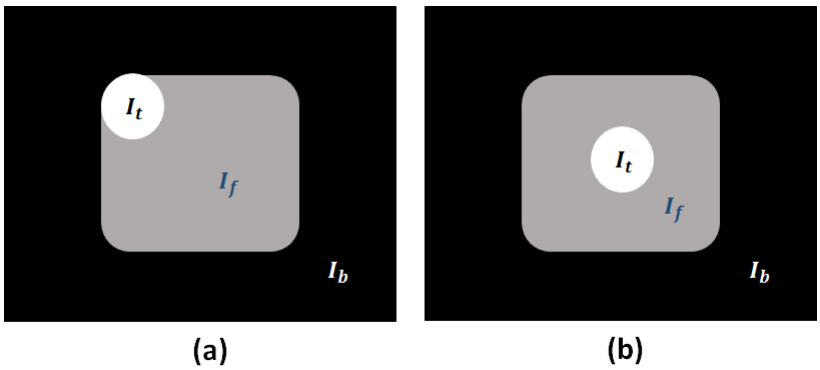

Figure 2.3: *Illustration of 2 kinds of configuration: (a) the target region is located on the boundary of the background and foreground. (b) it is situated on the center of the foreground.*

The MS evolution equation can be reformulated in the localized way (LMS) i.e., in the Lankton framework as follows:

$$\frac{\partial \phi}{\partial t}(x) = \delta\phi(x) \int_{\Omega_y} B(x,y)\delta\phi(y). \left(\frac{(I(y)-u_x)^2}{A_u} - \frac{(I(y)-v_x)^2}{A_v} \right) dy + \lambda\delta(\phi(x))\mathrm{div}\left(\frac{\nabla\phi(x)}{|\nabla\phi(x)|} \right) \tag{2.19}$$

where u_x and v_x are the localized mean intensities such as:

$$u_x = \frac{\int_{\Omega_y} B(x,y) \cdot H\phi(y) \cdot I(y) dy}{\int_{\Omega_y} B(x,y) \cdot H\phi(y) dy} \tag{2.20}$$

and

$$v_x = \frac{\int_{\Omega_y} B(x,y) \cdot (1 - H\phi(y)) \cdot I(y) dy}{\int_{\Omega_y} B(x,y) \cdot (1 - H\phi(y)) dy} \tag{2.21}$$

A_u and A_v represent the local areas of the interior and exterior regions respectively. They are defined by

$$A_u = \int_{\Omega_y} B(x,y) \cdot H\phi(y) dy \tag{2.22}$$

$$A_v = \int_{\Omega_y} B(x,y) \cdot (1 - H\phi(y))dy \tag{2.23}$$

We propose an alternative model less sensitive to the intensity distance between the image foreground and background. The evolution equation of the proposed model is formulated as follows:

$$\begin{aligned} \frac{\partial \phi}{\partial t}(x) = \delta\phi(x) \int_{\Omega_y} B(x,y)\delta\phi(y). \\ \left(\frac{(I(y) + \gamma M - u_x)^2}{A_u} - \frac{(I(y) + \gamma M - v_x)^2}{A_v} \right) dy \\ +\lambda\delta(\phi(x))\text{div}\left(\frac{\nabla\phi(x)}{|\nabla\phi(x)|} \right) \end{aligned} \tag{2.24}$$

where γ is the background compensation parameter and M a binary mask. These parameters are defined as follows:

$$\gamma = E\{I_f - I_t\} - \rho|E\{I_f\} - E\{I_t\}| \tag{2.25}$$

$$M = \begin{cases} 1, & I(i,j) \in I_b \\ 0, & \text{otherwise.} \end{cases} \tag{2.26}$$

where $\rho \in [0,1]$ is a weighting compensation parameter and $I(i,j)$ represents a pixel of the image I at the coordinate (i,j). The proposed LACM-BIC becomes equal to the Lankton MS model when γ is tuned as a zero constant value. In fact, I_f and I_b are easily separable in MR images by using an automatic thresholding method because of their high intensity difference. Therefore, due to its low computation time, the popular Otsu thresholding algorithm [33] is used to obtain M.
The proposed method can be implemented by using the following algorithm:

Data: Parameters such as current iteration (It) and maximum iteration number (It_{max})
Result: Final updated level set function
Initialize $It = 0$
Extract I_f and I_b by using an automatic thresholding method (e.g. Otsu Method[33])
while *($It \leq It_{max}$) and (convergence criterion is not reached)* **do**
  Initialize the level set function ϕ
  Update the local interior mean intensity by using Eq. (2.20)
  Update the local exterior mean intensity by using Eq. (2.21)
  Compute the intensity background compensation parameter γ by using Eq. (2.25)
  Update the level set function according to Eq. (2.24)
  $It = It + 1$
end

Algorithm 1: Algorithm of the proposed LACM-BIC in the level set formulation

2.5.3 Contour initialization and brain tumor segmentation

A special framework is introduced in this work with the aim to perform properly the brain tumor segmentation task. It is composed by two main steps: (1) the abnormal

growth cells detection by using the HCSD preceded by k-means algorithm and (2) its contour delineation via the proposed LACM-BIC. A proper initialization of the ACM is important so as to reach a good performance.

The HCSD is a binary shape descriptor based on hierarchical centroid. Proposed by [30] for handwriting recognition, this descriptor was used in [34] for automatic brain tumor detection in MRI data. As in [35, 36], for distinguishing structures based on their forms, present approach considered that tumors have in general an ellipsoidal shape compared to other brain structures. The HSCD was extracted from a cropped image containing tumor and was considered as reference. Consequently, given a new input image, after binarization step, the image was scanned by using a sliding window of 20% of the image size. The sliding window was moved forward in the manner to reach an overlap of 50% between adjacent windows in rows and columns. The HSCD was extracted from each window at every new position. Moreover, at the same time, the Euclidean distance was computed between the obtained descriptor and the reference. Finally, the tumor position was defined by the window that corresponds to the smallest distance. In a similar context, HCSD is applied here for the ACM initialization as in [1]. More specifically, only the two biggest binary structures are retrieved from the images. Then, based on their extracted HCSD, tumor structures are detected. Therefore, the same technique will be used in this work for the LRACM initialization.

The aim of the clustering stage is to classify the MR image structures into 4 regions such as: (a) Gray Matter (GM), (b) White Matter (WM), (c) black background and Cerebrospinal Fluid (CSF), and (d) tumor. The choice of the k-means technique was motivated by the a priori knowledge of cluster number and its low computational complexity. Next, the image was binarized by keeping only pixels classified in the high intensity cluster. But in general the obtained image contains other structures different from the tumorous tissues, hence an additional step is necessary for selecting only tumor structures in a binary image. At last, based on their pixel densities distribution, only tumor structures were kept by using the HCSD. As soon as the tumor location is detected, it is enclosed in a bounding-box. Then the ACM is initialized by a circular curve centered on the bounding-box centroid c and with a radius equal to $P/4$, where P is the perimeter of the bounding-box. Fig. 2.4 shows the tumor detection steps followed by the active contour initialization.

The outline of the abnormal tissue is given by the final result of the active contour model. By taking the advantage of using consecutive 3D slices, the final segmentation result of one slice is used as the initialization of the next slice for boosting the speed. However, additional steps are needed via a feedback process to ensure the ACM convergence to the targeted object. Fig. 2.5 depicts the proposed segmentation scheme using active contour models.

According to the previous description, the segmentation framework can be imple-

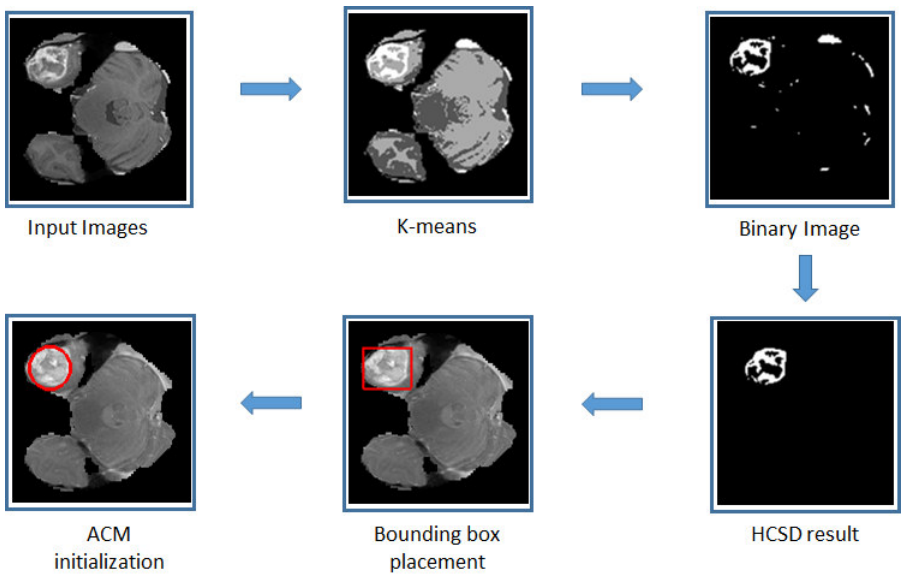

Figure 2.4: *Tumor detection and ACM initialization in the tumor segmentation process.*

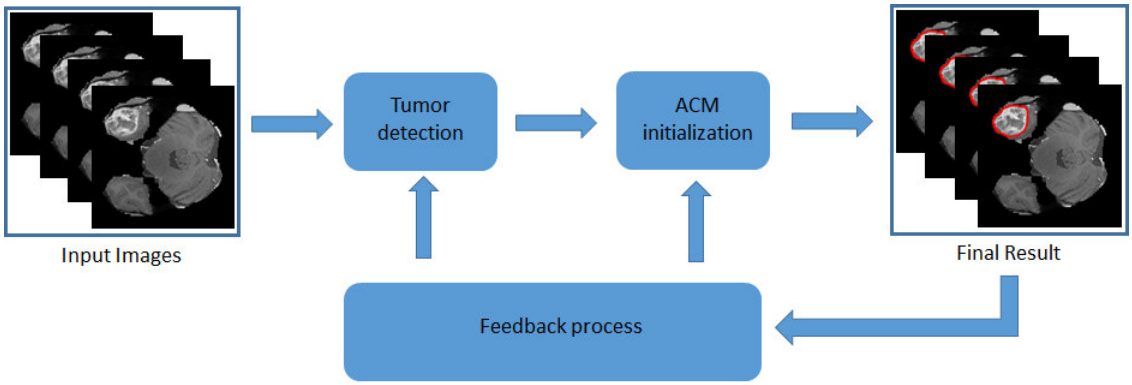

Figure 2.5: *Flowchart of the segmentation process.*

mented by using the algorithm presented below:

Data: Parameters such as current slice number (N_s), maximum slice number (M_s), deformability degree allowed (t_h) and the Dice coefficient (D)
Result: Final contour
Initialize $t_h = 0.8$, $D = t_h$
while ($N_s \leq M_s$) **do**
  if (N_s *is the number of the first slice) or* ($D < t_h$) **then**
    Use k-means and HCSD to detect tumor region
    Initialize de ACM with a circle $O(c, P/4)$
    Find the final contour
  else
    Initialize de ACM with the anterior final contour
    Find the new final contour
    Compute the Dice coefficient D between the new and the anterior final contour
  end
  $N_s = N_s + 1$
end

Algorithm 2: Proposed segmentation approach algorithm

The value of t_h defines the degree of deformability allowed between consecutive slices. The value of 0.80 was experimentally selected in order to maintain the active contour close to the desired region.

2.5.4 Experimental Results

In this section, the obtained results from segmentation approach that incorporate the proposed active contour model formulation are discussed. The implementation was done with an Intel Core i5 processor, 4 GB of memory using Matlab v.2011 tool. The experiments were carried out on synthetic and medical images. Medical experiments were carefully performed on the "BRATS 2012" database from the MICCAI 2012 Challenge on Multimodal Brain Tumor Segmentation Benchmark.

Four metrics were used for quantitatively evaluate the results i.e. the Dice coefficient (D), the Sensitivity (Sen), the Specificity (Spe) and the Hausdorff distance (d_H).

The majority of segmentation methods fails in extracting the desired region on images with background-foreground high mean intensity distance. Due to this, two synthetic images were neatly selected with the goal to demonstrate how the proposed method performs this task. In Fig. 2.6, an image with two possible targets on a low intensity background is presented. The LACM-BIC approach enables to separate perfectly these two regions of interest according to the contour initialization. The fourth column illustrates the results achieved by the proposed algorithm while the third presents the Lankton MS method results. These outcomes show better performance of the LACM-BIC compared to the Lankton model. Not only it outperforms the former, but also it is more flexible in adequate target selection.

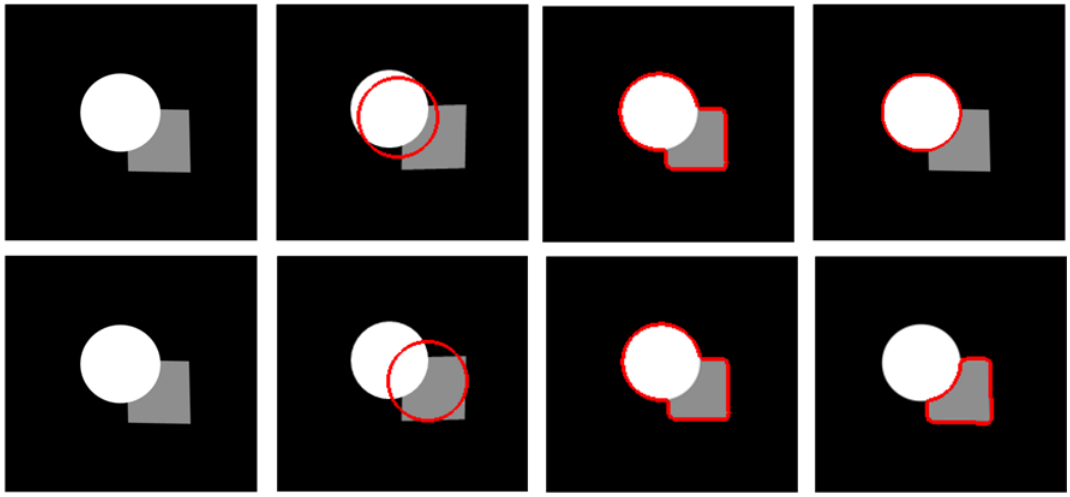

Figure 2.6: *Synthetic image with two target regions: (from left to right) input image, contour initialization, Lankton MS result and proposed*

Furthermore, another configuration is presented in Fig. 2.7. It is more similar to the brain tumor image where there is a low intensity background, a foreground and finally a target. The scalable and final results of the former LACM method are shown in the first row and the proposed LACM-BIC are presented in the second. The columns one, two and three show the contour initialization, the performance achieved on 10 iterations and those reached in 50 iterations, respectively. We observed that the proposed model find the desired area after 100 iterations whereas the LMS model was not able to find it after 1000 iterations.

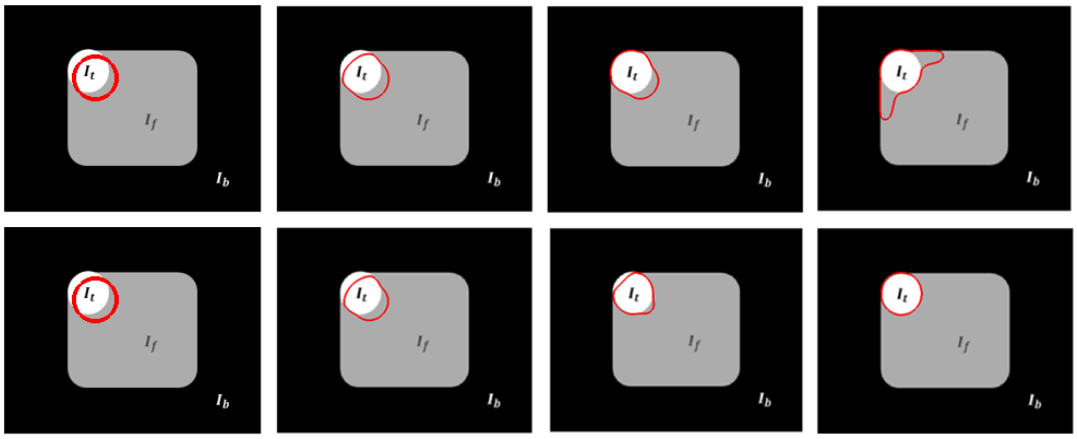

Figure 2.7: *Synthetic image illustrating a brain tumor. In row 1: (Lankton MS results from left to right) the contour initialization, the result after 10 iterations, the result after 50 iterations and the result after 1000 iterations. In rows 2: (Proposed results from left to right) the contour initialization, the result after 10 iterations, the result after 50 iterations and the final result after 100 iterations.*

The last phase of the experiment was carried out on simulated and real patient data with single tumor apparition. With the purpose to obtain results with a fair comparison, the same automatic active contour initialization as proposed in this study was used for all experiments. The parameters setting of the localized C-V [15], localized MS [15] and the LACM-BIC methods was done by using: $\alpha = 0.3$, $\epsilon = 1$, $r = 8$ and the maximal number of iteration equal to 500. Moreover, the proposed method computes automatically the background intensity compensation parameter γ (Eq. 2.25) and the weighting value was tuned as $\rho = 0.25$. The LGDF and LBF were settled as recommended in [37] and [18] for white matter segmentation in MR image, respectively.

Accuracy evaluation

Fig. 2.14 present some results obtained from real patient data with: (from left to right) the Local Binary Fitting (LBF), the Local Gaussian Distribution Fitting (LGDF), the localized Chan-Vese, the localized MS, and the proposed algorithm. It can be observed that the final delineations of the proposed method is robust against the background attraction where almost all the algorithms fails. The LBF method is not only sensitive to the background attraction, but also to the tuning parameters (specially the kernel scale parameter σ). In Fig. 2.15 other cases with simulated data are depicted. This experiment reveals that the suggested model was again able to segment the tumorous tissue more accurately than the comparative methods. We can clearly noticed that when the tumor is located far away from the brain boundary, the segmented images by the proposed LACM-BIC are almost the same with the traditional LMS model and in some cases with the Localized C-V model (e.g. rows 1-4 for real patient data and rows 2-4, 6 for simulated data). The LBF outputs are in many cases differents from the other methods (see Fig. 2.14 rows 1, 2, 3, 5, 6 and Fig. 2.15 rows 1, 4, 5, 7) because this model separates the non uniform tumor masses in different parts.

Table 3.2 summarizes the results obtained for each comparative methods in the segmentation of 11 patient data i.e. 3 real data and 8 simulated data (a total of 312 images). In majority of cases, the results obtained are similar for all the methods. Particularly, when the tumor is located close to the background region, the suggested method has demonstrated the capability of extracting accurately the target. It can be observed

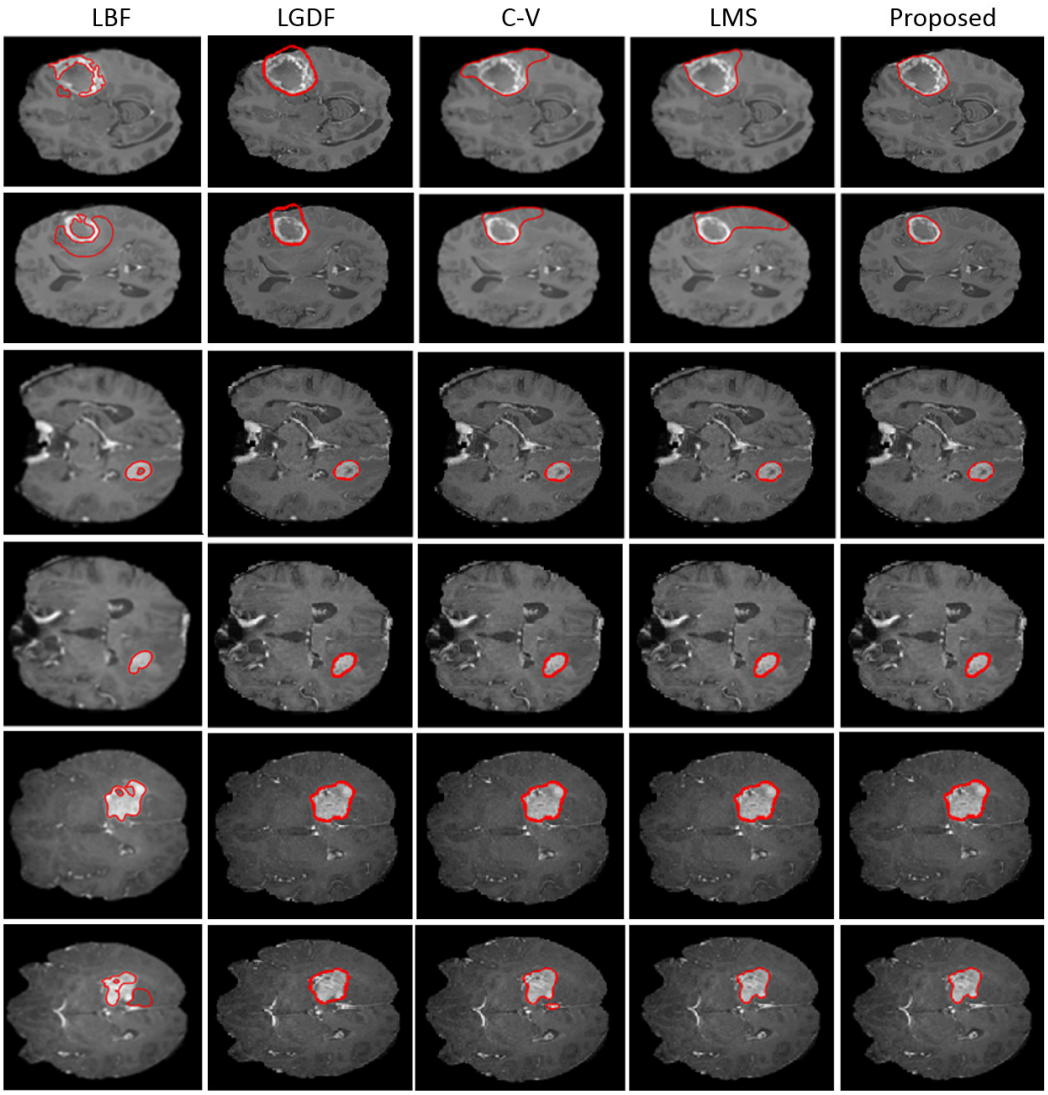

Figure 2.8: *Segmentation results of real patient data: (from left to right) the Local Gaussian Distribution Fitting (LGDF), the localized Chan-Vese, the localized MS, and the proposed algorithm.*

for patient 1 from real data (BRATS) where the proposed approach provides the best rate of segmentation. The reached Dice measure was 0.9585 and the Hausdorff distance was 2.2976. However, the Dice rate values achieved by the comparative methods were 0.5286, 0.8109, 0.8023 and 0.8577 for the LBF, the LGDF, Localized C-V and Localized MS models, respectively; whereas their distances were 4.9470, 3.6048, 4.9108 and 3.9766. In addition, although the LACM-BIC outperforms the LBF, LMS and Localized C-V models in the segmentation case of the patient 8 of simulated data ($D = 0.8548$ and d_H=2.8271), the LGDF performs better with the values of $D = 0.8943$ and d_H=2.5759. Similar results are observed for patient 2 of real data where $D = 0.9393$, $d_H = 1.8491$ for LGDF and $D = 0.9078$, $d_H = 1.8571$ for the LACM-BIC. In general, the LGDF is more complex than the MS model by the fact that it takes into account the local mean intensity value and the corresponding standard deviation while the second considers only the local mean intensity value. Nevertheless, the LGDF is more sensitive to its parameters setting face up to a lot of heterogeneous image data. For this reason it outperforms the proposed method and others mentioned only in particular cases of these

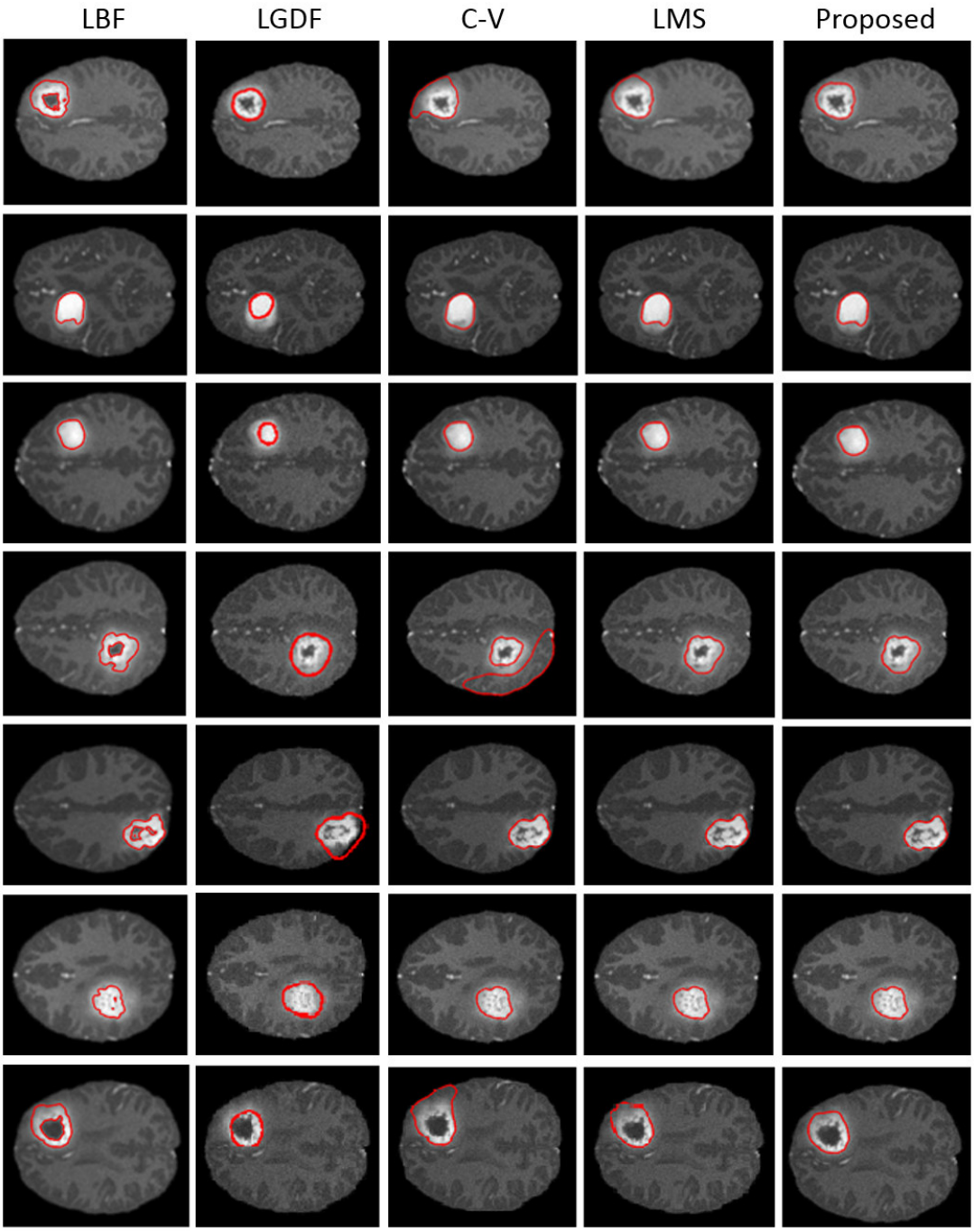

Figure 2.9: *Segmentation results of simulated patient data: (from left to right) the Local Binary FItting (LBF), the Local Gaussian Distribution Fitting (LGDF), the localized Chan-Vese, the localized MS, and the LACM-BIC method.*

experiments. Even if the LGDF can improve its performance by adapting its parameters to each images kind, the background attraction will continue playing an important role.

Table 2.10 presents the average and standard deviation (mean $\pm$ standard deviation) of the performance of the suggested model and the comparative models. It can be clearly seen that the proposed LACM-BIC achieves better performance than the LBF, LGDF, localized C-V and, LMS models. For instance, the Dice coefficient value of 0.9102 reached by the LACM-BIC was the highest obtained and its Hausdorff distance of 2.2968 was the lowest. Also, the experiments show that the proposed model is characterized by the lowest standard deviation of the Dice index and the Hausdorff distance what means that the results from all experiments are clustered around the mean value. Additionally, its highest mean specificity value ($Spe = 0.9980$) reveals that it can correctly classify healthy tissue more than the comparative methods. Its mean sensitivity value ($Sen = 0.9501$) indicates that it can detect true tumor regions in a competitive manner. On the whole, the LBF method is the technique that reached poor results in these experiments.

The use of clustering techniques such as k-means, Fuzzy C-Means (FCM) and Expectation maximization (EM) is sufficient for the initialization step (preprocessing stage), but it is not enough for the brain tumor segmentation task in general. Table 2.4 shows the obtained average results by using the EM and FCM, and the outcome reveals their lower accuracy rate versus to the proposed method. On the other hand, this table indicates also that the problem of high mean intensity distance between an image foreground and its background cannot be resolved just by the image intensity normalization. Although the intensity is normalized in the range of [0,255], the LACM-BIC method still outperforms the LMS model.

Computation time comparison

It is visually presented in Fig. 2.10 and quantitatively in Table 2.5 that the intensity background compensation allows to reduce the computation time (expressed in seconds). Precisely, the proposed LACM-BIC consumes lesser time versus to the comparative methods for accomplishing the required tumor segmentation task (an average of 448.5725 seconds per patient and 15.8150 seconds per image slice). The LBF was the slowest method in suggested tests followed by the LGDF. In fact, due to its low delineation accuracies and based on the Algorithm 2, the HCSD initialization is several times performed and it has a consequence of increasing the computation time. The image number label 1 to 3 in Fig. 2.10 refers to real patient data and from 4 to 11 the simulated patient data. The curve behavior depicted in this figure shows the cumulative computation time, which means the total time spent for segmenting the brain tumor in patients data from image number 1 to 11.

2.5.5 Conclusions

In this work a framework for brain tumor image segmentation in multimodal MRI data is presented. Specially, we proposed a localized active contour with background intensity compensation (LACM-BIC) method which is adapted for handling images with high mean distance between an image background and its foreground as in the case of medical images. This technique was integrated in the previous framework for extracting brain abnormal tissue. Unlike many approaches, a proper and automatic

Table 2.2: *Accuracy comparison of each patient (real and simulated) with different methods by using: Dice, Sensitivity, Specificity and Hausdorff distance metrics. Patients 1 to 3 are from real data while Patients 4 to 11 correspond to patient 1, 2, 3, 5, 6, 7, 8 and 9 from simulated data.*

Patient	Metric	LBF [18]	LGDF [19]	C-V [15]	LMS [15]	Proposed
Patient 1	D	0.5286	0.8109	0.8023	0.8577	0.9585
	Sen	0.5672	0.8844	0.9936	0.9904	0.9723
	Spe	0.9777	0.9903	0.9751	0.9845	0.9979
	d_H	4.9470	3.6048	4.9108	3.9766	2.2976
Patient 2	D	0.8931	0.9393	0.9246	0.9077	0.9078
	Sen	0.8084	0.8975	0.8652	0.8342	0.8345
	Spe	1.0000	0.9999	1.0000	1.0000	1.0000
	d_H	1.8370	1.8491	1.8403	1.8816	1.8571
Patient 3	D	0.9045	0.9225	0.9590	0.9588	0.9588
	Sen	0.8688	0.9466	0.9482	0.9368	0.9368
	Spe	0.9987	0.9979	0.9994	0.9996	0.9996
	d_H	2.6060	2.4738	2.1230	2.0551	2.0551
Patient 4	D	0.9567	0.8055	0.9637	0.9671	0.9671
	Sen	0.9222	0.7230	0.9834	0.9641	0.9641
	Spe	0.9999	0.9996	0.9990	0.9995	0.9995
	d_H	2.0020	2.7570	2.0369	1.9429	1.9429
Patient 5	D	0.9528	0.8164	0.9498	0.9451	0.9454
	Sen	0.9215	0.7627	0.9559	0.9343	0.9338
	Spe	0.9999	0.9993	0.9993	0.9995	0.9995
	d_H	1.9620	2.6456	2.0149	2.0161	1.9817
Patient 6	D	0.7435	0.7265	0.7427	0.7617	0.7612
	Sen	0.9460	0.9986	0.9998	0.9997	0.9997
	Spe	0.9918	0.9909	0.9917	0.9925	0.9925
	d_H	3.1870	3.2321	3.1089	3.0071	3.0171
Patient 7	D	0.1066	0.7608	0.8212	0.8802	0.8802
	Sen	1.0000	0.9865	0.9930	0.9825	0.9825
	Spe	0.8342	0.9938	0.9960	0.9975	0.9975
	d_H	10.220	3.2169	2.6757	2.2684	2.2684
Patient 8	D	0.8394	0.8394	0.9302	0.9244	0.9289
	Sen	0.7494	0.8929	0.8949	0.8748	0.8766
	Spe	0.9997	0.9933	0.9991	0.9995	0.9997
	d_H	3.5620	3.5085	2.9224	2.8834	2.8691
Patient 9	D	0.8637	0.7923	0.8439	0.8850	0.8850
	Sen	0.9824	0.9711	0.9938	0.9851	0.9851
	Spe	0.9960	0.9933	0.9952	0.9969	0.9969
	d_H	2.6770	3.0520	2.6254	2.2987	2.2987
Patient 10	D	0.8406	0.8943	0.7495	0.8018	0.8548
	Sen	0.9853	0.9752	0.9928	0.9887	0.9887
	Spe	0.9952	0.9973	0.9895	0.9932	0.9957
	d_H	2.9590	2.5779	3.5954	3.2820	2.8271
Patient 11	D	0.9581	0.7266	0.9601	0.9642	0.9648
	Sen	0.9322	0.5929	0.9865	0.9771	0.9771
	Spe	0.9998	0.9997	0.9987	0.9990	0.9991
	d_H	1.8440	3.3147	1.9604	1.8639	1.8501

Average and standard deviation of similarity measures				
Methods	Dice coefficient	Sensitivity	Specificity	Hausdorff distance
LBF [18]	0.7807 ± 0.2556	0.8803± 0.1291	0.9812± 0.04919	3.4363 ± 2.4320
LGDF [19]	0.8213 ± 0.0725	0.8756± 0.1298	0.9959± 0.0036	2.9302 ± 0.5232
C-V [15]	0.8770 ± 0.0869	0.9643± 0.0452	0.9948 ± 0.0074	2.7104 ± 0.9187
LMS [15]	0.8958 ± 0.0676	0.9516± 0.0532	0.9965± 0.0048	2.4978± 0.6942
Proposed	0.9102 ± 0.0627	0.9501 ± 0.0518	0.9980 ± 0.0023	2.2968 ± 0.4248

Table 2.3: *Average and standard deviation of similarity measures: the Dice index, Sensitivity, Specificity and Hausdorff distance*

Similarity measures				
Methods	Dice coefficient	Sensitivity	Specificity	Hausdorff distance
EM	0.7867 ± 0.1536	0.7556± 0.1470	0.9985± 0.0015	3.0480 ± 0.7542
FCM	0.7967 ± 0.1424	0.8275± 0.1550	0.9969 ± 0.0033	3.2823 ± 0.8320
LMS [0,255]	0.8980 ± 0.0679	0.9516± 0.0532	0.9972± 0.0030	2.4644± 0.5813
Proposed	0.9102 ± 0.06271	0.9501 ± 0.0518	0.9980 ± 0.0023	2.2968 ± 0.4248

Table 2.4: *Average and standard deviation of similarity measures: the Dice index, Sensitivity, Specificity and Hausdorff distance of the EM, FCM, LMS with the intensity normalized in the range of 0-255 and the proposed method*

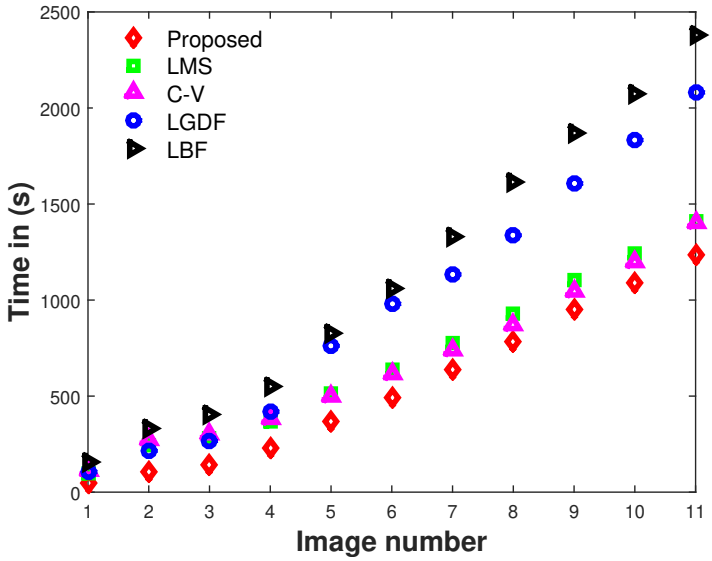

Figure 2.10: *Cumulative computation time comparison of different methods on a set of 11 patient data (in seconds).*

Average of computation time in (s)					
Measures	LBF [18]	LGDF [19]	C-V [15]	LMS [15]	Proposed
Time/patient	849.8082	781.5818	455.7580	485.5883	448.5725
Time/image	29.9610	27.5558	16.0684	17.1201	15.8150

Table 2.5: *Average computation time*

contour initialization was introduced by using the k-means algorithm followed by the Hierarchical Centroid Shape Descriptor (HCSD). Firstly, the tumor location is automatically detected and it is enclosed in a bounding-box. The box centroid and a quarter of its perimeter value are respectively used as center and radius of a circle used as ini-

tial contour. Then, the segmentation is carried out via the proposed LACM-BIC. This model is flexible and able to select an object target in presence of an imprecise initialization. In this last case, the area highly covered by the initial contour is selected as region to delineate.

Several experiments were carefully performed on a set of synthetic and medical images. The influence of a high mean distance between an image background and its foreground has been specially analyzed on the synthetic images for the segmentation of a given target. The obtained results show that the proposed active contour model achieves better performance than the local binary fitting, Chan-Vese and Yezzi models in the localized formulation of Lankton. We also compared the proposed model against the comparative models on medical images from the widely known database "BRATS2012". Four metrics were used for this purpose: the Dice coefficient, the specificity, the sensibility, and the Hausdorff distance. In spite of the visual inspection that was in many cases enough for the evaluation, the quantitative assessment was performed through the selected metrics. The outcomes demonstrate that the accuracy of the proposed model outperforms the Chan-Vese, the Yezzi and the Wang models for the tumor segmentation task. Moreover, it is important to notice that the LACM-BIC formulation was able to perform the brain tumor segmentation task in the lowest computation time compared to the former methods. Additional experiments were done for comparing the clustering methods EM and FCM versus to the LACM-BIC, and the results demonstrated that the proposed method achieves higher performance than the clustering techniques. Also, it outperforms the LMS model even if the image intensity is normalized. The proposed segmentation framework has advantages of being fast for segmenting brain tumor in consecutive slices of a 3D volume and it can found an application in images of other modalities such as computed tomography and ultrasound that also have large black backgrounds. Thanks to the professor Lankton, Wang and Li together with their co-authors for making available their source codes.

2.6 Proposed method II: Automatic selection of LRACM using image content analysis for brain tumor segmentation

2.6.1 System description

The proposed system is based on the fact that the outcomes reached by different LRACM, under the same conditions, are not the same. For instance, let Ω be the global dataset $s.t.$ $\Omega = A_1 \cup A_2 \cdots \cup A_i$ where A_i represents the image subsets of Ω and i the subset index. It is observed that one method can be better than the others for the given subset A_1 and another one could be the best for the subset A_2 and so on. Likewise, the segmentation results achieved in our previous work [1] showed that the LACM-BIC outperforms in general comparative methods. However, for the images of the considered patients, the Localized C-V [15] and LGDF [19] methods reached the best results in three and two patient cases, respectively. Therefore, the automatic selection task of an active contour model for a given input image set can allow to improve the segmentation outcomes. Hence, a system that has to perform this selection based on supervised learning techniques is proposed. It consists in two main stages, which denoted as training and testing steps. In the same fashion, the used dataset is split into two parts, namely, training and testing sets. Sixty percent of dataset images is used for training and the remainder forty percent for testing the designed system. Data are grouped into three classes or subsets A_i ($\forall\, i = 1, 2, 3$) based on the ACM segmentation

results achieved in [1]. Let I denote an input image, the selection of the algorithm with the best expectation performance is achieved by extracting first n image features $\{\alpha_j\}_{j=1}^{n}$ from I. Then, a classifier is employed to analyze the feature vector $y \in \Re^n$ in order to predict the class to whom each I belongs. Any classifier can be integrated in this framework, but currently the experiment will be carried out using the k-NN and random forest (RF) classifiers. The system receives an input image I, then it extracts the vector y that includes eight image features ($y = \alpha_1, \ldots, \alpha_n, n = 8$) to describe the image content. Lastly, the system has an output $Z \in \{1, 2, 3\}$ that corresponds to the label of the selected LRACM (1: LACM-BIC, 2: C-V and 3: LGDF).

Moreover, in the design of the system, it is assumed that 2D images of a 3D volume acquired from a specific patient ($i.e.$ under the same conditions, with the same scanner, imaging protocol and acquisition parameters) share the same features. Consequently, they can be grouped in the same subset A_i for which one a LRACM should be automatically selected. In supervised learning, A_i is known as actual class or ground truth (GT). Even if each 2D slice image will be separately classified in a predicted class C_i via a label $z \in \{1, 2, 3\}$, the selection rule of the LRACM by the system should be carried out in function of the 3D volume (image patient dataset). Let P^m be the image set of the m-th patient and h_i^m the number of samples (slices) in a predicted class C_i^m subject to

$$P^m = \{I_1^m, \ldots, I_k^m\} \tag{2.27}$$

$$C_i^m = \{I_k^m | g : I_k^m \rightarrow y_k^m \quad and \quad f : y_k^m \rightarrow z_{|z=i}\} \tag{2.28}$$

$$h_i^m = \#C_i^m \tag{2.29}$$

where, k is the number of 2D images I^m in the volume P^m, $\#C_i^m$ the cardinality of C_i^m, g the function that extracts feature vectors $y_k^m = \{y_1^m, \ldots, y_k^m | g : I_k^m \rightarrow y_k^m\}$ and the f the decision function that attaches to y_k^m a class z. Two notations of labels are used, z is the label of a slice I_k^m (or partial label), while Z is the final label assigned to the volume P^m. Fig. 2.11 describes the selection process of the LRACM for brain tumor segmentation in MRI data. Firstly, based on selection rules, the proposed system selects the LRACM considered as the best for handling the volume P^m. Secondly, slices of P^m are segmented by using the selected LRACM.

The class membership of P^m will be performed by using majority vote among images $I_k^m, (m = 1, \ldots, k)$, $i.e.$ by looking for the largest h_i^m. This last part can be found by computing the index of the most populous predicted class as

$$q = \underset{z \in \{1,2,3\}}{\arg\max} \{h_z^m\} \tag{2.30}$$

Also, the index q can be computed by using the prediction classification rate as

$$q = \underset{z \in \{1,2,3\}}{\arg\max} \{h_z^m / \sum_{i=1}^{3} h_i^m\} \tag{2.31}$$

For example, the label $Z = 1$ will be attached to P^m if $q = 1$, and in details when

$$h_1^m > h_2^m \quad \cap \quad h_1^m > h_3^m \tag{2.32}$$

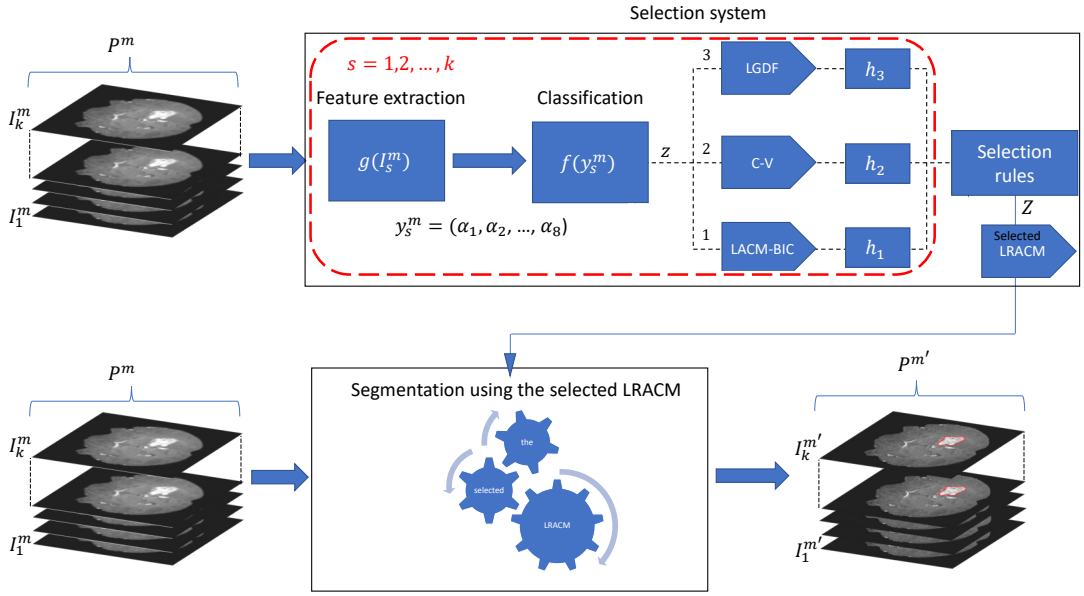

Figure 2.11: *Flowchart of the LRACM selection for brain tumor segmentation in MRI data. First, the selection system selects the LRACM considered as the best for processing the volume P^m. Second, slices of P^m are segmented by using the selected LRACM. $I^{m'}$ are the segmented images and $P^{m'}$ the output volume.*

or by using the prediction classification rate as

$$h_1^m / \sum_{i=1}^{3} h_i^m > h_2^m / \sum_{i=1}^{3} h_i^m \quad \cap \quad h_1^m / \sum_{i=1}^{3} h_i^m > h_3^m / \sum_{i=1}^{3} h_i^m \tag{2.33}$$

These last two rules (Eq. 2.32-2.33) are equivalents and they will lead to the same result. However, the former equation (based on Eq. 2.30) is simple and faster than second one in implementation, while the latter (based on Eq. 2.31) is preferred when the classification rate evaluation is needed. In special cases, when no class receives a majority of vote h_i^m, the selection rule will assign to P^m a class membership based on prior probability. This last part is related to the class size. Moreover, by referring to Table 4.1, it is clear that the size of class 1 is the biggest and the size of class 2 is bigger than that of class 3. To illustrate this, if $h_1^m = h_2^m > h_3^m$ or $h_1^m = h_3^m > h_2^m$ or $h_1^m = h_2^m = h_3^m$, the selection rule will assign to P^m a class membership Z=1. Besides, if $h_2^m = h_3^m > h_1^m$, a label Z=2 will be then attached to P^m.

The selection rules of the proposed system can be implemented by using the following algorithm:

Data: Parameters such as total patient number (p_{max}), current patient volume ($P^m, m = 1, \ldots, p_{max}$), total slice number ($k$), current slice ($I_s^m, s = 1, \ldots, k$), slice classification label (z) and the class index (i)
Result: the patient classification label (Z)
Initialize $m = 1$, $s = 1$, $C_i^m = 0$, $h_i^m = 0$
while *($m \leq p_{max}$)* **do**
  Read volume P^m
  Extract k
  while *($s \leq k$)* **do**
    Extract feature vector y_s^m
    Classify y_s^m by using the decision function f, s.t. $f : y_k^s \rightarrow z$ via a classifier
    Update C_i^m by using Eq. (2.28) with $i = z$
  end
  for *i=1,2,...,3* **do**
    Update $h_i^m = \#C_i^m$, see Eq. (2.29)
  end
  Find q, the index of the largest h_z^m, by using Eq. (2.30) or Eq. (2.31)
  Find the subset w that satisfy $h_q^m = h_z^m$, $s.t.\ z \in w \subseteq \{1, 2, 3\}$
  if $z = 1 \in w$ **then**
    $Z = 1$
  else if $z = 2 \in w$ **then**
    $Z = 2$
  else
    $Z = 3$
  end
  $m = m + 1$
end

Algorithm 3: Algorithm of the proposed LRACM selection system where selection rules are described

2.6.2 Feature extraction

Statistical features are used to numerically describe images and, they should provide information to represent an overall scene. If the computed features are chosen carefully to obtain the most representatives and discriminants, it is expected that the feature set will extract the relevant information from the image. These features allow performing the desired task exploiting a reduced representation instead of using the full image. The features considered for this work are mainly related to the description of statistical moments; eight features are then selected and evaluated. These statistical moment features are listed in Table 2.6.

Table 2.6: *Statistical features calculated on the $M \times N$ monochromatic image $I(x, y)$*

Feature	Name	Mathematical description
f_1	Mean	$\frac{1}{MN}\sum_{x=1}^{M}\sum_{y=1}^{N} I(x,y)$
f_2	Harmonic mean	$\frac{MN}{\sum_{x=1}^{M}\sum_{y=1}^{N} 1/I(x,y)}$
f_3	Trimmed mean	$\frac{1}{M_{90\%}N_{90\%}}\sum_{x=P_5}^{M_{P_{95}}}\sum_{y=P_5}^{N_{P_{95}}} I(x,y)$
f_4	Maximum value	$\max\{I(x,y)\}$
f_5	Median	$\left(\frac{MN+1}{2}\right)^{th} term$
f_6	Standard deviation	$\sqrt{\frac{1}{MN}\sum_{x=1}^{M}\sum_{y=1}^{N}\left(I(x,y) - f_1\right)^2}$
f_7	Skewness	$\sqrt{MN}\frac{\sum_{x=1}^{M}\sum_{y=1}^{N}(I(x,y)-f_1)^3}{\left(\sum_{x=1}^{M}\sum_{y=1}^{N}(I(x,y)-f_1)^2\right)^{3/2}}$
f_8	Kurtosis	$MN\frac{\sum_{x=1}^{M}\sum_{y=1}^{N}(I(x,y)-f_1)^4}{\left(\sum_{x=1}^{M}\sum_{y=1}^{N}(I(x,y)-f_1)^2\right)^2}$

2.6.3 Patient Image Dataset

A total of 605 images were used in this study. These data consist in 312 images (or set Γ_1) from 11 patients taken into account in [1] and 293 additional images (Γ_2) carefully selected from the same patients. As previously mentioned, the data were divided into two groups, training and testing sets. The testing image set (Γ_{test}) is composed by data from Γ_1 excepting 70 images (Γ_3) that were moved into the training set Γ_{train}. These moved data concern patients for which ones most of all images containing the tumor were already used in Γ_1 ($e.g.$ patients 1, 4, 5, 8, 9, 10 and 11). Thus, some data describing the tumor were needed for the training set Γ_{train}. The training set includes Γ_2 and Γ_3. The details of the dataset are presented in Table 4.1. It is important to note that our dataset consists in a couple of MRI data from the MICCAI 2012 Challenge on Multimodal Brain Tumor Segmentation Benchmark database organized by B. Menze, A. Jakab, S. Bauer, M. Reyes, M. Prastawa, and K. Van Leemput (`http://www.imm.dtu.dk/projects/BRATS2012`, [7]).

Table 2.7: *Data from MICCAI 2012 Challenge on Multimodal Brain Tumor Segmentation Benchmark used in this work. The testing image set Γ_{test} is a part of Γ_1, which represents the number of images per patient as used in [1]. Furthermore, Γ_3 shows how many images were moved from Γ_1 to the training set Γ_{train}. Finally, it can be seen that $\Gamma_{train} = \Gamma_2 + \Gamma_3$.*

Patient	Γ_1 [1]	Γ_3	Γ_{test}	Γ_{train}
1	44	15	29	49
2	13	-	13	19
3	22	-	22	33
4	31	10	21	34
5	31	10	21	32
6	26	-	26	39
7	21	-	21	21
8	36	10	26	32
9	26	5	21	24
10	31	10	21	45
11	31	10	21	35
Total images	312	70	242	363

2.6.4 Experimental Results

This section provides and discusses the experimental results obtained in the segmentation of brain tumors with the proposed ACM selection system. Experiments were carefully conducted on the "BRATS-2012" database from the MICCAI 2012 Challenge on Multimodal Brain Tumor Segmentation Benchmark. Moreover, two binary metrics were used for quantitatively evaluate the segmentation results, the Dice coefficient (D) and the Hausdorff distance (d_H).

Selection system evaluation

As already mentioned, the K-NN and RF methods were employed for image classification by using the extracted features. Furthermore, the evaluation of the selecting system was carried out by using the success rate (SR) [38] of image classification per patient. Whereas, the number of samples misclassified was assessed by using the failure rate (FR). Largely used in supervised learning, confusion matrices were employed to compute the SR and FR for each patient. In the confusion matrix, the predictions are

found in the columns and the ground truth (GT) class in the rows. The GT indicates the class of patient's data based on the best ACM segmentation result reached in [1]. The percentages of classification rates are defined by

$$SR = 100 \times (N_{correct}/N) \tag{2.34}$$

$$FR = 100 \times (N_{wrong}/N) \tag{2.35}$$

where $N_{correct}$, N_{wrong} and N are the instances correctly classified, the instances misclassified and the total number of samples, respectively.

Figures. 2.12 and 2.13 present the confusion matrices of the patient image set classification by using the k-NN and RF classifiers, respectively. The bold values in the main diagonal represent all instances correctly classified ($N_{correct}$). The row under each confusion matrix indicates the classification rate in percentage ($h^m_{i=z}/\sum_{i=1}^{3} h^m_i$, $z \in \{1, 2, 3\}$) of image instances in each predicted class. The bold values represent the success rates (in percentage) achieved in the images classification process. The other values are the failure rates (in percentage and per class). The total FR is the sum of failure rate of each class. Indeed, the selection made by the proposed system is successful when SR is the highest classification rate value for a specific patient. On the other hand, in the cases of system failure, the underlined value (FR) corresponds to the selected class.

Table 3.1 describes the successes and failures of the automatic selector for the patient classes compared to the ground truth by using the k-NN and RF classifiers. The class with the highest classification rate is selected as the expected prediction. Besides, the selection is successful when the prediction is equal to the GT. Almost all patients except patient 8, have been correctly classified by using the k-NN method. Additionally, with the RF algorithm, eight out of eleven patients were properly chosen. In this configuration, the selector based on k-NN showed better success rate than which based on RF classifier. Nevertheless, the objectives of this research is not oriented to testing classifiers but on the ACM selection system. By the way, another classifier ($e.g.$ Adaboost, Bayessian-based classifiers, Neural Networks, etc) can be integrated in this framework. Notice that their performances rely mainly on the training samples quality and the discriminant features extracted from the image [39, 40, 41].

Performance of the ACM selection system in brain tumor segmentation

The aim of this work was to show that object segmentation by using ACM is image content dependent. A system for the selection of the best ACM based on image content was designed. Experiments were conducted in two main steps. Firstly, brain tumors were segmented in the image set of each patient by using the LGDF, C-V and LAC-BIC methods. Thenceforth, for the same patient image set, the selection of the best method among the three was performed. Table 3.2 presents the quantitative results reached by the ACM selection method and the ACM individually considered. These results come from the selection task achieved by the automatic selector and previously listed in Table 3.1. It is clearly observed that, in the majority of cases, the best method for a specific patient is correctly selected by the system. In order to have a global view of the outcomes, the average values (mean $\pm$ standard deviation) are showed in Table 2.10.

The results reveal that the proposed selection system achieves higher performance than comparative methods (i.e. $D = 0.9115 \pm 0.0702$, $d_H = 2.3288 \pm 0.4411$ with RF and $D = 0.9160 \pm 0.0654$, $d_H = 2.2985 \pm 0.4265$ with k-NN). Figs 2.14 and 2.15 depict the

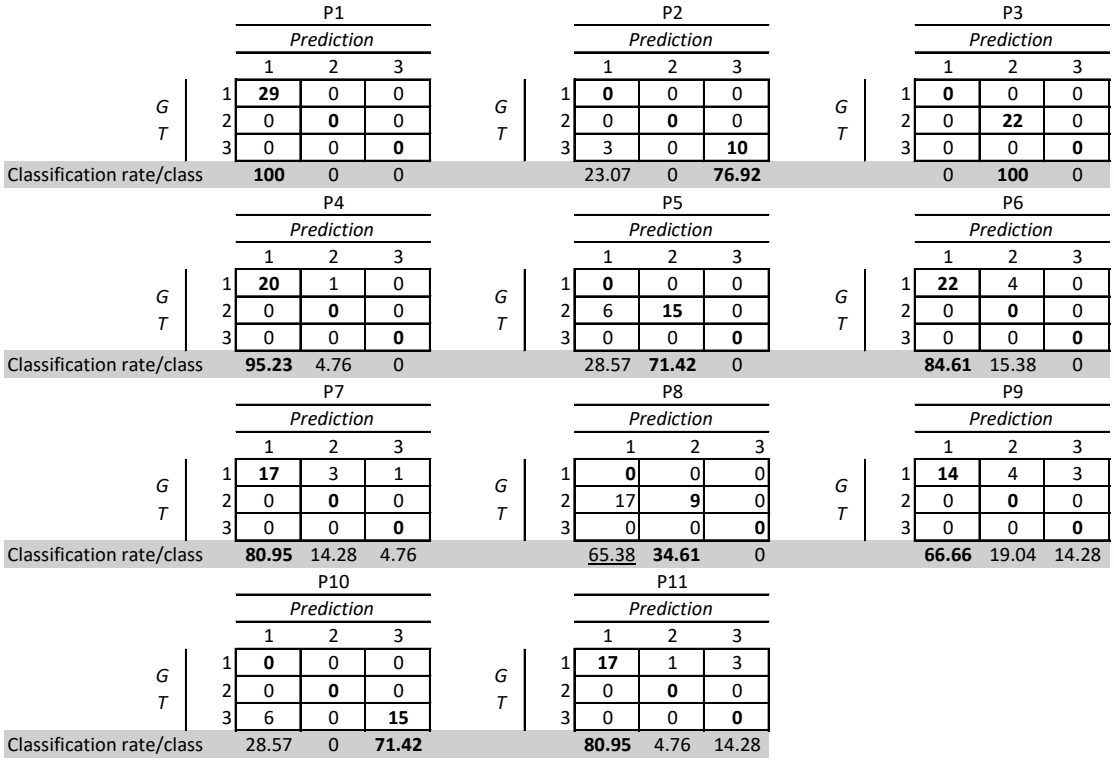

Figure 2.12: *Confusion matrix of patient image set classification using k-NN algorithm where the labels represent 1: LACM-BIC, 2: C-V and 3: LGDF. The bold values in the main diagonal represent all instances correctly classified. The row under each confusion matrix shows the classification rate achieved for each predicted class.*

Table 2.8: *Classification rate used to find the predicted class for each patient. The class with the highest classification rate is selected as the estimated prediction. Likewise, the selection is successful when prediction is equal to GT. The bold values represent the highest classification rate reached among the three classes and they define the class to be selected.*

	Classification rate/class			Classification rate/class					
Patient	RF			k-NN			Predictions		GT
	1	2	3	1	2	3	RF	k-NN	
1	**96.55**	0.000	3.400	**100.0**	0.000	0.000	1	1	1
2	15.38	0.000	**84.61**	23.07	0.000	**76.92**	3	3	3
3	0.000	**100.0**	0.000	0.000	**100.0**	0.000	2	2	2
4	**80.95**	19.04	0.000	**95.23**	4.760	0.000	1	1	1
5	**66.66**	33.33	0.000	28.57	**71.42**	0.000	1	2	2
6	**100.0**	0.000	0.000	**84.61**	15.38	0.000	1	1	1
7	**85.71**	14.28	0.000	**80.95**	14.28	4.760	1	1	1
8	**92.30**	7.69	0.000	**65.38**	34.61	0.000	1	1	2
9	**100.0**	0.000	0.000	**66.66**	19.04	14.28	1	1	1
10	**61.90**	0.000	38.09	28.57	0.000	**71.42**	1	3	3
11	**85.71**	4.760	9.500	**80.95**	4.760	14.28	1	1	1

results achieved by using the LGDF, C-V, LAC-BIC and the selecting system. The label of the selected active contour method is showed on the images in the selector column. Visual results sustain the quantitative evaluation where the LACM-BIC, followed by the C-V method, reached better performances than the LGDF model. Especially, in the

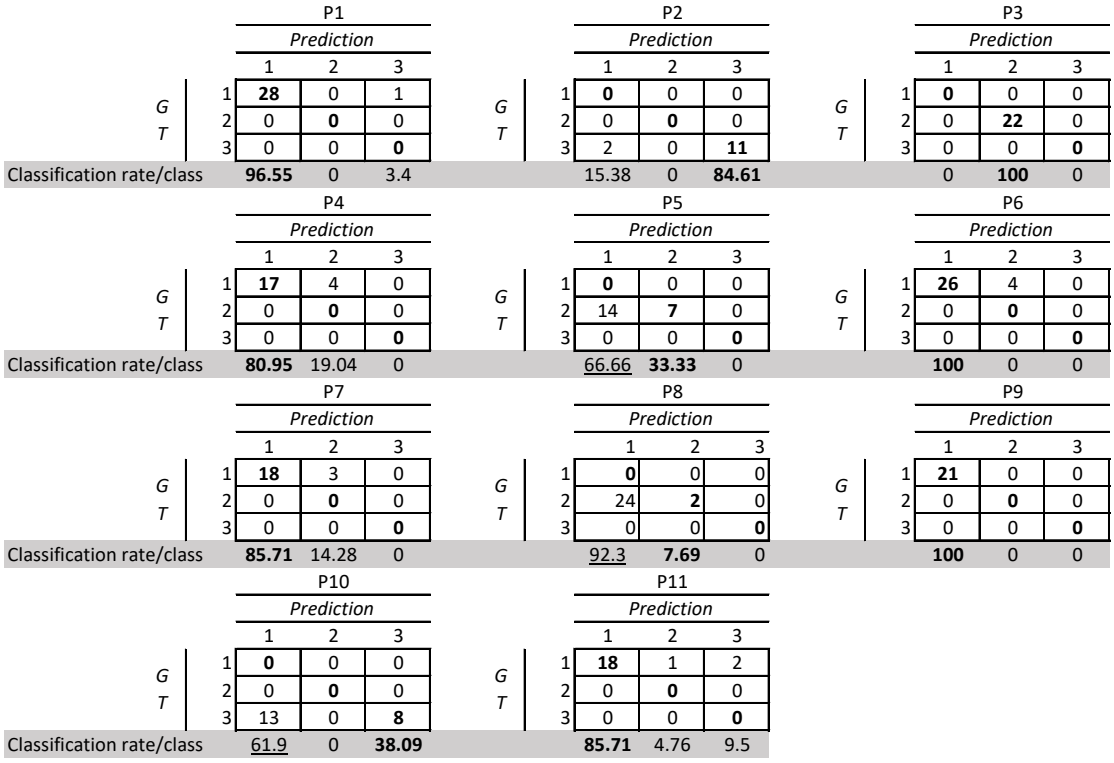

Figure 2.13: *Confusion matrix of patient image set classification using random forest algorithm where the labels represent 1: LACM-BIC, 2: C-V and 3: LGDF. The bold values in the main diagonal represent all instances correctly classified. The row under each confusion matrix shows the classification rate achieved for each predicted class.*

case of patient 1, it can be clearly observed that LACM-BIC is suitable for handling images where the target shared the border with the background and foreground.

2.7 Proposed method III: Active Contours Driven by Cuckoo Search Strategy for Brain Tumor Images Segmentation

2.7.1 Cuckoo Search algorithm

Cuckoo Search is a bio-inspired optimisation technique that mimics the brood parasitism behaviour of many species of cuckoos. CS was proposed by [42] as a way to exploit some features from swarm intelligence, such as diversification and intensification, through random walks and Lévy flights. The basic idea of CS consists in the laying of an egg by each cuckoo and hides it in an alien nest. At the beginning, a given number of nests are randomly chosen. Thereafter, only the best nest (with luckiest egg or best solution) shall prevail for next generation, $\mathbf{x}^*$. Nests with poorer solutions ($\mathbf{x}_i^t$) are replaced with new eggs, or with solutions from some available nests ($\mathbf{x}_i^{t+1}$) using a Lévy flight, as

$$\mathbf{x}_i^{t+1} = \mathbf{x}_i^t + \zeta\nu(\mathbf{x}_i^t - \mathbf{x}^*), \tag{2.36}$$

where $\zeta > 0$ is the step size and its value is related to the size of the search space of the problem; $\mathbf{x}_i^t = (x_{i,1}^t, \ldots, x_{i,d}^t)^T$ is the i-th solution at generation t with d components (or dimensions of the search space); and ν is a random number obtained from Mantegna's

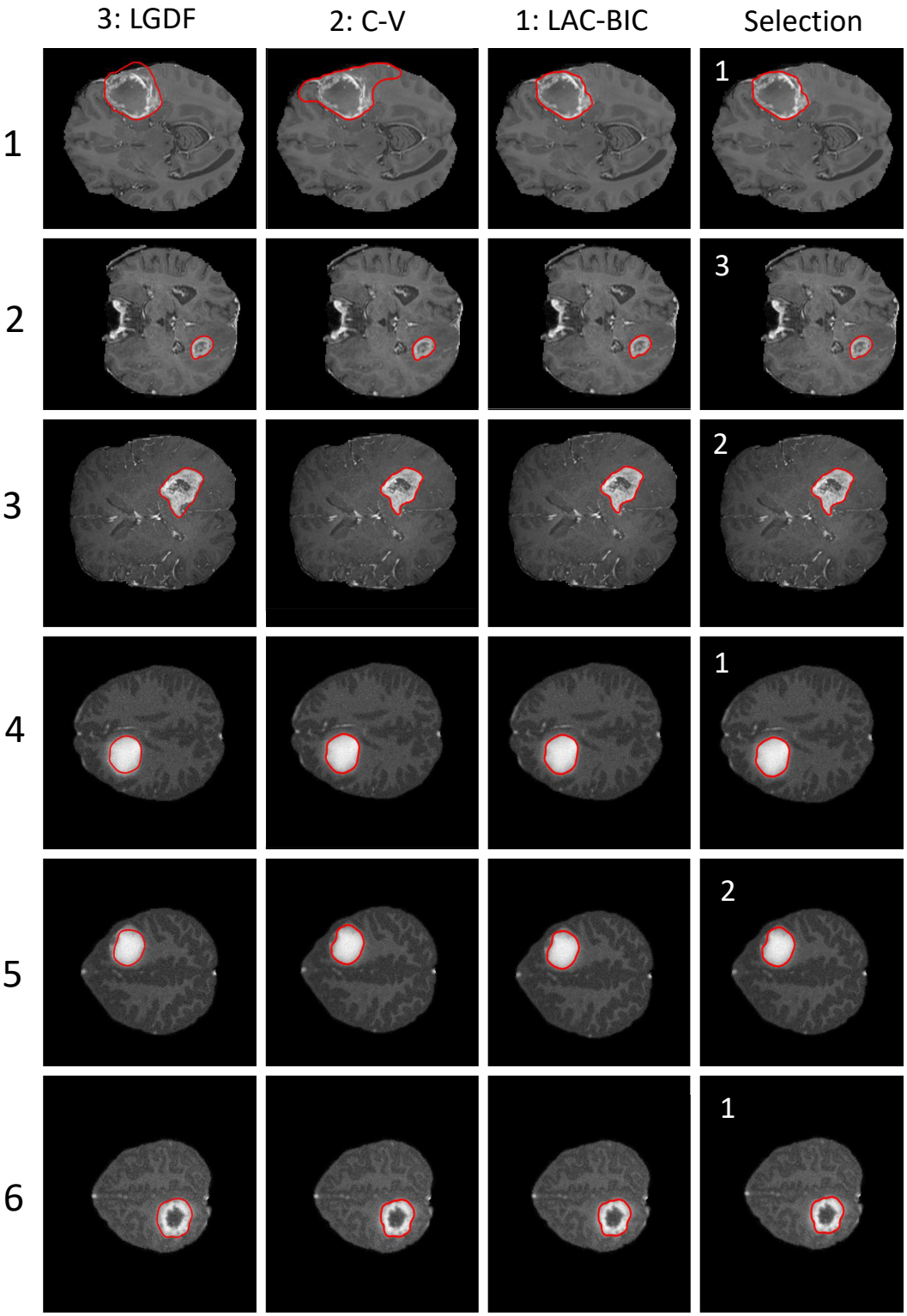

Figure 2.14: *Segmentation results of MRI data from patients 1 to 6: (from left to right) the Local Gaussian Distribution Fitting (LGDF), the localized Chan-Vese (C-V), the Localized Active Contour Model with Background Intensity Compensation (LACM-BIC), and the proposed algorithm.*

Table 2.9: *Accuracy comparison of each patient with different methods by using: Dice and Hausdorff distance metrics.*

Patient	Metric	LGDF [19]	C-V [15]	LACM-BIC [1]	Selection (RF)	Selection (k-NN)
1	D	0.8159	0.7833	**0.9618**	**0.9618**	**0.9618**
	d_H	3.3200	5.2736	**2.3678**	**2.3678**	**2.3678**
2	D	**0.9401**	0.9246	0.9077	**0.9401**	**0.9401**
	d_H	**1.8202**	1.8403	1.8571	**1.8202**	**1.8202**
3	D	0.9252	**0.9590**	0.9588	**0.9590**	**0.9590**
	d_H	2.3588	**2.0550**	2.1229	**2.0550**	**2.0550**
4	D	0.8721	0.9658	**0.9687**	**0.9687**	**0.9687**
	d_H	2.5413	1.8367	**1.8081**	**1.8081**	**1.8081**
5	D	0.6987	**0.9738**	0.9721	0.9721	**0.9738**
	d_H	3.2288	**1.9348**	2.0021	2.0021	**1.9348**
6	D	0.7062	0.7252	**0.7602**	**0.7602**	**0.7602**
	d_H	3.4082	3.3463	**3.0170**	**3.0170**	**3.0170**
7	D	0.7781	0.8203	**0.8619**	**0.8619**	**0.8619**
	d_H	2.8781	2.6834	**2.4012**	**2.4012**	**2.4012**
8	D	0.8645	**0.9316**	0.9291	0.9291	0.9291
	d_H	3.5260	**2.9321**	2.9861	2.9861	2.9861
9	D	0.8156	0.8601	**0.8938**	**0.8938**	**0.8938**
	d_H	2.9599	2.6702	**2.4067**	**2.4067**	**2.4067**
10	D	**0.8676**	0.6966	0.8197	0.8197	**0.8676**
	d_H	**2.5048**	3.7618	2.7707	2.7707	**2.5048**
11	D	0.6637	0.9502	**0.9602**	**0.9602**	**0.9602**
	d_H	3.3411	2.0866	**1.9819**	**1.9819**	**1.9819**

Table 2.10: *Average and standard deviation of similarity measures: the Dice index and Hausdorff distance*

Average and standard deviation of similarity measures		
Methods	Dice coefficient	Hausdorff distance
LGDF [19]	0.8134 ± 0.0927	2.8988 ± 0.5364
C-V [15]	0.8719 ± 0.1011	2.7655 ± 1.0506
LAC-BIC [1]	0.9085 ± 0.0696	2.3383 ± 0.4331
Selection (RF)	0.9115 ± 0.0702	2.3288 ± 0.4411
Selection (k-NN)	$\mathbf{0.9160 \pm 0.0654}$	$\mathbf{2.2985 \pm 0.4265}$

algorithm using a symmetric Lévy stable distribution [43, 44]. Equation (2.37) shows the basic form of Mantegna's algorithm,

$$\nu = z|y|^{-1/\rho} \tag{2.37}$$

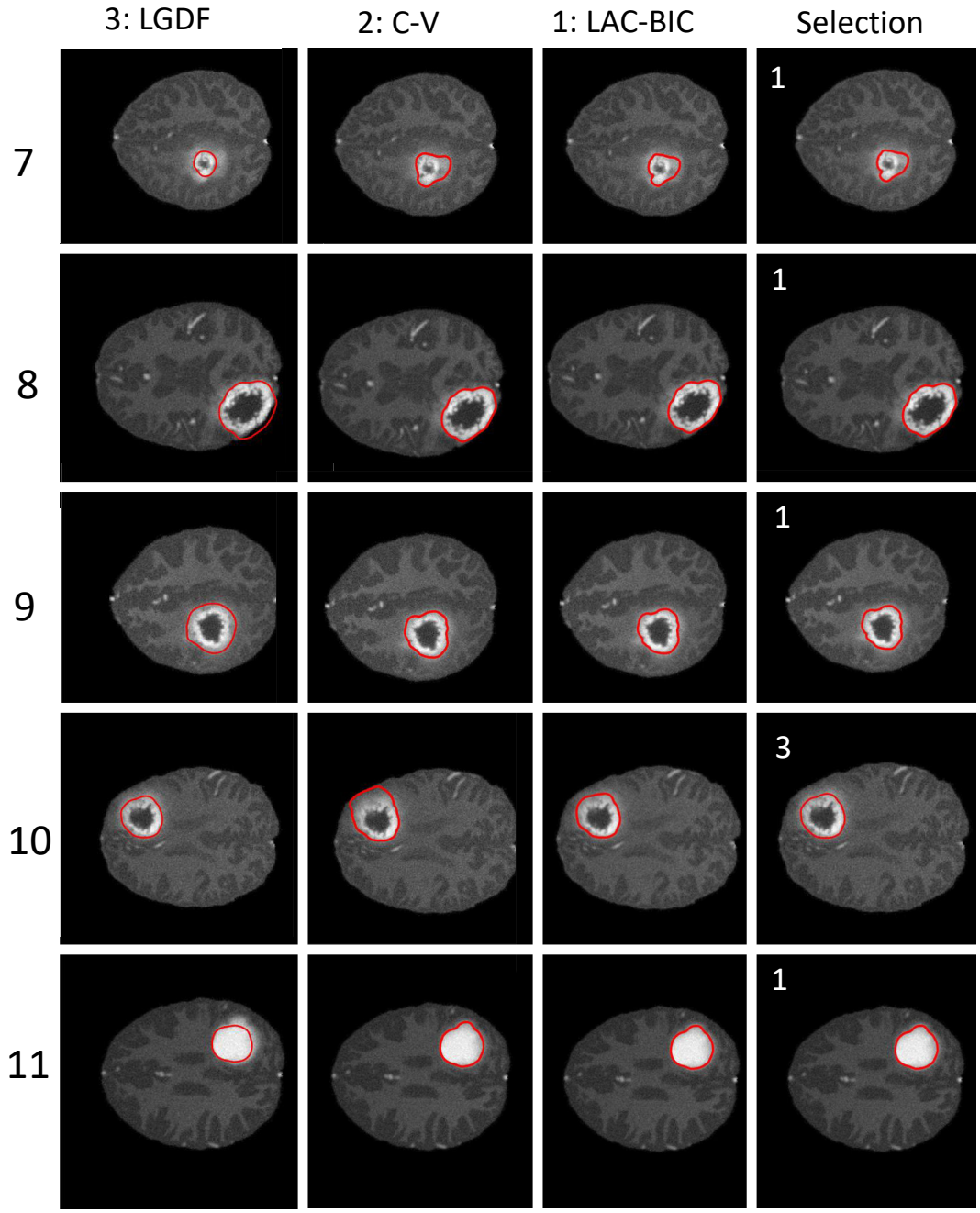

Figure 2.15: *Segmentation results of MRI data from patients 7 to 11: (from left to right) the Local Gaussian Distribution Fitting (LGDF), the localized Chan-Vese (C-V), the Localized Active Contour Model with Background Intensity Compensation (LACM-BIC), and the proposed method.*

where $\rho \in [0.3, 1.99]$ is a parameter of distribution and, z and y are random variables with normal distributions $\mathcal{N}(0, \sigma_z)$ and $\mathcal{N}(0, 1)$, respectively. σ_z is obtained with

$$\sigma_z = \left[\frac{\Gamma(\rho+1)\sin\left(\frac{\pi\rho}{2}\right)}{\rho\Gamma\left(\frac{\rho+1}{2}\right)2^{(\rho-1)/2}} \right]^{1/\rho}, \tag{2.38}$$

since $\Gamma(\cdot)$ is the Gamma function.

Additionally, if some cuckoo eggs are discovered by the host bird, then cuckoos have to find other available nests to hide their new eggs or candidates of solution. This event can occur with a probability of $p_a \in \mathcal{U}(0,1)$, for a defined number of nests, and new solutions are calculated using,

$$\mathbf{x}_i^{t+1} = \mathbf{x}_i^t + \mathbf{u}\mu(\mathbf{u} - p_a)(\mathbf{x}_j^t - \mathbf{x}_k^t), \tag{2.39}$$

where $\mathbf{u} = (u_1, \ldots, u_d)^T$ is a uniformly distributed random vector with size $d \times 1$; $\mu(\cdot)$ is the Heaviside function [44]; $\mathbf{x}_i^{t+1}$ is the i-th new solution and $\mathbf{x}_i^t$ is the i-th current solution; and $\mathbf{x}_j^t$ and $\mathbf{x}_k^t$ are two different solutions randomly chosen, $j \neq k$. The above process is done for a defined number of generations or iterations, until it reaches a stop criterion. The CS method is presented in Algorithm 4.

Data: Objective function $f(\mathbf{x}),\ \mathbf{x} = (x_1, \ldots, x_d)^T$
Parameters such as nests (N_a), probability (p_a), step size (ζ),
maximum generation number (M) and stop criterion (if it exists)
Result: Best solution, $\mathbf{x}^* = \arg\min_X\{f(\mathbf{x})\}$
Initialise N_a host nests as $\mathbf{x}_i\ \forall\ i = 1, \ldots, N_a$, and make $t = 0$.
while *($t < M$) and (stop criterion is not reached)* **do**
  $t = t + 1$
  For each host nest, calculate randomly by Lévy flights its new value ($\mathbf{x}_i$) with (2.36),
  and its fitness ($f(\mathbf{x}_i)$)
  if *New fitness is better than previous one* **then**
    Update by new solution
  else
    Maintain previous solution
  end
  Build a new nest if it is discovered, with (2.39)
  Find the current best solution
end

Algorithm 4: Cuckoo Search Algorithm

2.7.2 Tumor segmentation approach

An active contour problem is solved traditionally through a deterministic iterative method such as gradient descent [13]. But some non-deterministic modern strategies are also implemented to solve this problem. One of them is the multi-population strategy proposed by [45], which employs Particle Swarm Optimisation (PSO) algorithm and Rectangular Shaped Search Windows (RSSW). In general, the multi-population strategy can be implemented with several optimisation techniques and different geometries for the search windows. However, in this work Cuckoo Search algorithm is used as optimiser, which gives place to the so-called Multi-population Cuckoo Search Strategy (MCSS), and a windows shape alternative is proposed, i.e., Pizza-slice Shaped Search Windows (PSSW). Thus, the MCSS and the above mentioned search window geometries are described as follows.

Let $\mathbf{P}_i$ be the i-th control point (or snaxel) of an active contour (or snake), defined as $\mathbf{P}_i(s,t) = (x(s,t), y(s,t))^T$, inside of the i-th search window ($\mathbf{SW}_i$) with $s \in [0,1]$ and t is the time. And let $\mathbf{q}_{i,j}$ be the j-th candidate to control point in the i-th search window. Local energy function for each candidate in a given search window is defined

as

$$\begin{aligned} E_{i,j} =& \frac{1}{2}\left(\alpha\|\mathbf{P}_{i+1}-\mathbf{q}_{i,j}\|^2+\beta\|\mathbf{P}_{i+1}-2\mathbf{q}_{i,j}+\mathbf{P}_{i-1}\|^2\right), \\ =& \gamma_{line}C(\mathbf{q}_{i,j})-\gamma_{edge}|\nabla G * I(\mathbf{q}_{i,j})|^2+\gamma_{term}\left.\frac{C_{yy}C_x^2-2C_{xy}C_xC_y+C_{xx}C_y^2}{(C_x^2+C_y^2)^{3/2}}\right|_{\mathbf{q}_{i,j}}, \end{aligned} \tag{2.40}$$

where α, β, γ_{line}, γ_{edge} and γ_{term} are weight factors, and the external energy components are evaluated at the candidate position $\mathbf{q}_{i,j}$ via an interpolation process.

Using (2.40) we can set an optimisation problem for each search window, as is shown,

$$k_i = \arg\min_j\{E_{i,j}\},\ j\in\{1,\ldots,N_a\}\subset \mathbf{SW}_i, \tag{2.41}$$

where k_i is the best index such as $\mathbf{q}_{i,k_i}$ is the best candidate with minimum local energy, and N_a is the number of candidates in $\mathbf{SW}_i$. Therefore, the i-th control point shall be updated with $\mathbf{q}_{i,k_i}$, $\mathbf{P}_i=\mathbf{q}_{i,k_1}$. Equation (2.41) is solved for all N_p snaxels of the active contour using Cuckoo Search algorithm (or another optimisation method). Thus, total snake energy is estimated through the next equation [45],

$$E_{snake}\approx\sum_{i=1}^{N_p}E_{i,k_i}. \tag{2.42}$$

Finally, the above process is repeated until the total snake energy becomes stable, i.e, the energy value is the same or decreases slightly per each repetition or iteration. The overall process is summarised in Algorithm 5.

Data: Optimisation method (i.e., Cuckoo Search) and initial active contour (Snake)
Result: Best active contour
Initialise parameters of the optimisation method
while *(is evolving)* **do**
  for *(each control point P_i, $i=1,\ldots,N_p$)* **do**
    Set the window for P_i and define each P_i as the best solution for each search window
    Perform an optimisation process to solve (2.41)
    Update P_i with $\mathbf{q}_{i,k_i}$
  end
end

Algorithm 5: Multi-population Cuckoo Search Strategy (MCSS)

Furthermore, in order to implement the multi-population strategy, two geometries for search windows are described as follows, i.e., RSSW and PSSW. Figure 2.16 shows an illustrative example of these two geometries.

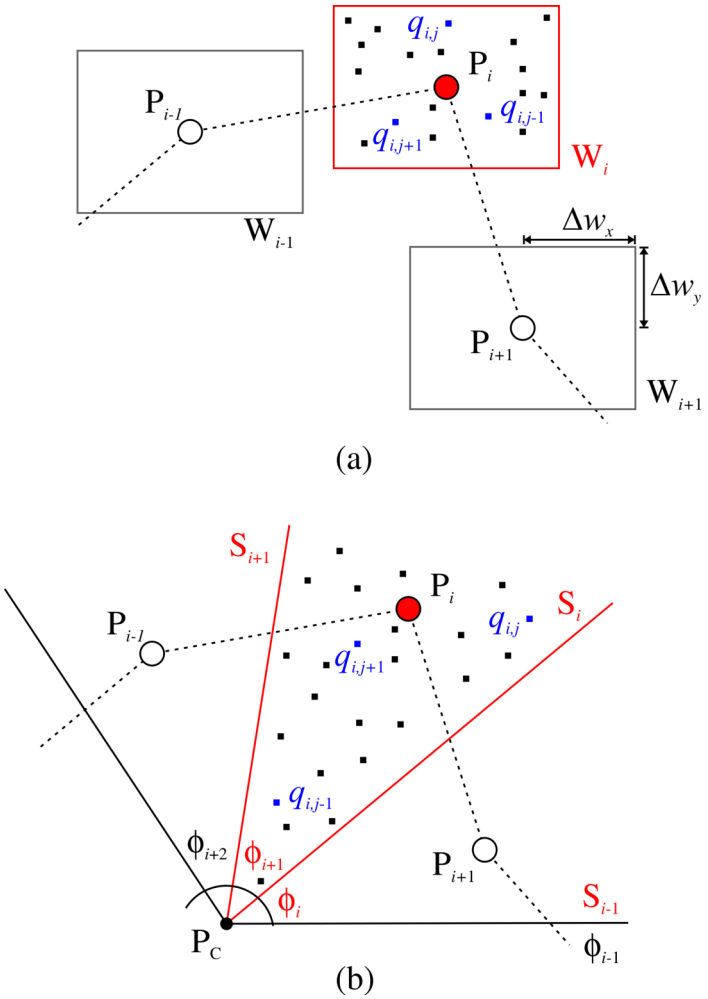

Figure 2.16: *Illustrative example of (a) Rectangular Shaped Search Window (RSSW) and (b) Pizza-slice Shaped Search Window (PSSW).*

2.7.3 Using Rectangular Shaped Search Windows (RSSW)

Let $\mathbf{W}_i$ be a rectangular shaped search window defined by

$$\mathbf{W}_i(\mathbf{P}_i, \Delta\mathbf{w}) = \{\mathbf{q}_{i,j} | \|\mathbf{q}_{i,j} - \mathbf{P}_i\|_1 \preceq_{\mathbb{R}^2} \Delta\mathbf{w}\}, \tag{2.43}$$

where $\mathbf{P}_i = (P_{i,x}, P_{i,y})^T$ is the i-th control point (or centre point of the search window), and $\Delta\mathbf{w} = (\Delta w_x, \Delta w_y)^T \in \mathbb{R}^2_{++}$ is a vector with half side lengths of the search window as components (cf. Figure 2.16.a).

Moreover, sometimes certain snaxels could be as close as to share their search space, thus generating unsuitable new control points, therefore an additional condition is required to preserve the snake structure. In order to avoid this issue, each candidate to a new control point must meet the following condition,

$$|\|\mathbf{P}_{i-1} - \mathbf{q}_{i,j}\| - \|\mathbf{P}_{i+1} - \mathbf{q}_{i,j}\|| < \epsilon, \tag{2.44}$$

where ϵ is constant value between 0.5 and 1 [45].

2.7.4 Using Pizza-slice Shaped Search Windows (PSSW)

Let $\mathbf{S}_i$ be a pizza-slice shaped search window defined by

$$\mathbf{S}_i(\mathbf{P}_c, \phi_l, \phi_u) = \{\mathbf{q}_{i,j} | \phi_l \leq \angle(\mathbf{q}_{i,j} - \mathbf{P}_c) \leq \phi_u\}, \tag{2.45}$$

where $\mathbf{P}_c = (P_{c,x}, P_{c,y})^T$ is the centroid point and, ϕ_l and ϕ_u are the lower and upper angles that delimit the polar section, respectively (cf. Figure 2.16.b). For this kind of search window, unlike RSSW, an additional condition is unnecessary.

2.7.5 Experimental Results and Discussion

The results discussed in this section were obtained from the proposed method implemented in a personal computer with the following specifications: CPU Intel® Pentium™ 1.9 GHz, 4 GB of RAM, Microsoft® Windows™ 10, 64-bit operating system, and MathWorks® Matlab™ R2014b platform. At first, all tests were performed for a set of common synthetic test images and, thereupon, for a set of T1-weigted MR images containing brain tumors.

At the beginning, a process of adjusting was performed for all the images before applying the active contour model based strategies. This process consisted of a noise removal step using a median filter with a 3×3 window size. It is followed by the edge detection using the Canny filter. Subsequently, aiming to improve the convergence of the active contour methods, a segmentation process was carried out via a Euclidean distance map, computed from the concerned images [46].

In order to demonstrate the effectiveness of the proposed method, the ACM driven by Particle Swarm Optimisation (PSO) was implemented as a Multi-population Particle Swarm Optimisation Strategy (MPSOS). Based on their performances, the proposed Multi-population Cuckoo Search Strategy (MCSS) was compared against the traditional active contour formulation (using the gradient descent) and MPSOS. Metaheuristic-based multi-population strategies (MCSS and MPSOS) were carried out with a number of 50 agents (nests or particles, respectively), using both geometries of search windows—RSSW with a window size of 40 $\times$ 40 pixels and PSSW with a polar section of $2\pi/N_p$ radians. The assessments of the ACM strategies were performed

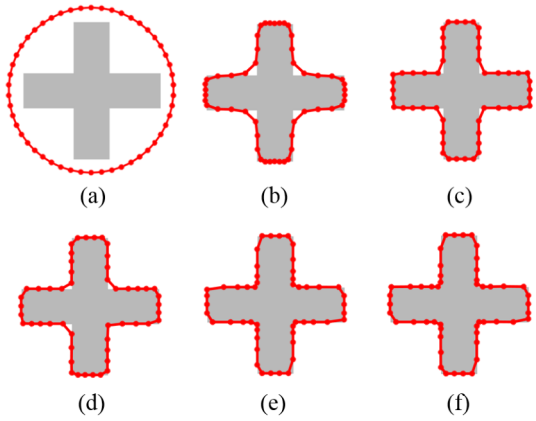

Figure 2.17: *(a) Initial contour for a symmetric cross image, and contours obtained via (b) traditional active contour method and, (c) MPSOS-RSSW, (d) MCSS-RSSW, (e) MPSOS-PSSW and (f) MCSS-PSSW.*

through three similarity metrics, i.e, Jaccard coefficient (J), Dice coefficient (D) and Hausdorff distance (d_{H}).

2.7.6 Synthetic test images

Two synthetic images (i.e., a cross and a star) were selected in order to perform the experiments, which were repeated 10 times for statistical purposes, using $\alpha = 0.004$ and $\beta = 0.001$. The external energy components for the synthetic cross image were set as $\gamma_{line} = 0.8$, $\gamma_{edge} = 0.1$ and $\gamma_{term} = 0.6$, and for the synthetic star image as $\gamma_{line} = 0.6$, $\gamma_{edge} = 0.8$ and $\gamma_{term} = 0.2$. Figure 2.17 presents the segmentation results of a symmetric cross of size 252 $\times$ 252 pixels with 50 control points ($N_p = 50$), achieved by the traditional technique and the multi-population strategies. All the ACM processes were initialised with the contour showed in Figure 2.17.a. At first glance, it is noticed that contours found by the multi-population strategies (Figure 2.17.c-f) are closer to the cross boundary than the one reached by the traditional technique (Figure 2.17.b). In addition, PSSW (cf. Figure 2.17.e-f) enhances the capability of the multi-population techniques to envelope better the object compared to RSSW (cf. Figure 2.17.c-d). Table 2.11 shows the performance reached by the studied ACM techniques. For this experiment,

Table 2.11: *Jaccard, Dice and Hausdorff distance rates obtained from the optimal contour of the synthetic cross image reached using the ACM strategies, i.e., the traditional technique and multi-population methods (MPSOS and MCSS) with RSSW and PSSW*

Strategy	J (AVG±SD×10^{-3})	D (AVG±SD×10^{-3})	d_H (AVG±SD×10^{-3})	Time (s) (AVG±SD)	Iterations (AVG±SD)
Traditional	0.8823±0.0	0.9375±0.0	7.4162±0.0	**86.2±80.4**	90±0
MPSOS-RSSW	0.9436±1.3	0.9710±0.6	5.4863±28.6	131.1±71.2	24±3
MCSS-RSSW	0.9392±3.1	0.9687±1.6	5.4407±575.7	186.5±106.9	30±4
MPSOS-PSSW	0.9474±2.3	0.9730±1.2	5.4399±90.4	109.8±56.0	**11±2**
MCSS-PSSW	**0.9476±2.8**	**0.9731±1.4**	**5.3837±133.3**	119.7±65.4	24±6

traditional snake was the fastest by spending an average time of 86.2 s for achieving its best contour, whilst the MCSS-PSSW was the most accurate with an average metric values of $J = 0.9476$, $D = 0.9731$ and $d_H = 5.3837$.

The second ACM experiment consisted on the segmentation of an horizontally symmetrical synthetic star of size 413×420 pixels, employing 70 control points for its initialization, as is shown in Figure 2.18.a. Its resulting contours, attained through the traditional and the multi-population methods, are displayed in Figure 2.18.b-f. It

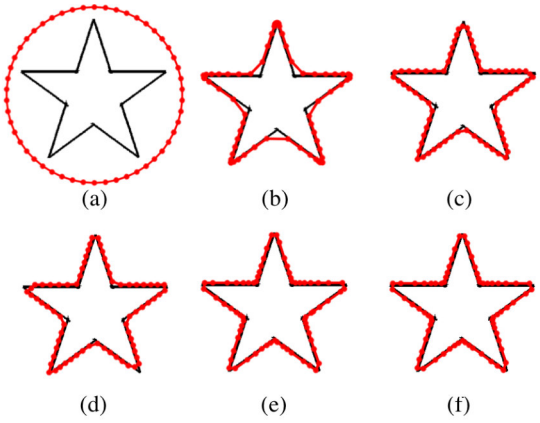

Figure 2.18: *(a) Initial contour for a horizontally symmetrical star image, and contours obtained via (b) traditional active contour method and, (c) MPSOS-RSSW, (d) MCSS-RSSW, (e) MPSOS-PSSW and (f) MCSS-PSSW.*

can be observed that the use of multi-population techniques improves the ACM behaviour in the segmentation task. Furthermore, in order to support the previous claim, a quantitative comparison of the proposed technique against the traditional and MPSOS methods, using the preselected metrics (Jaccard, Dice and Hausdorff rates), is presented in Table 2.12. Once more, the gradient descent method has required the shortest time (94.8 s) to evolve towards the object boundary. In addition, MCSS-PSSW performed better the star segmentation with accuracy values of $J = 0.9631$, $D = 0.9812$ and $d_H = 4.1351$.

Table 2.12: *Jaccard, Dice and Hausdorff rates obtained from the optimal contour of the synthetic star image reached using the ACM strategies, i.e., the traditional technique and multi-population methods (MPSOS and MCSS) with RSSW and PSSW.*

Strategy	J (AVG±SD×10^{-3})	D (AVG±SD×10^{-3})	d_H (AVG±SD×10^{-3})	Time (s) (AVG±SD)	Iterations (AVG±SD)
Traditional	0.9438±0.0	0.9711±0.0	7.4833±0.0	**94.8±102.0**	81±0
MPSOS-RSSW	0.9534±3.1	0.9761±1.6	4.3498±446.4	631.7±343.2	41±3
MCSS-RSSW	0.9559±1.1	0.9775±0.5	3.8312±155.1	849.0±483.0	45±4
MPSOS-PSSW	0.9621±1.3	0.9807±0.7	4.1829±63.0	372.1±184.5	**11±2**
MCSS-PSSW	**0.9631±0.1**	**0.9812±0.1**	**4.1351±37.8**	454.0±250.6	26±6

Indeed, in the cases of these two synthetic images, it was observed that the metric value results are consistent with contours observed in Figure 2.17.f and Figure 2.18.f. On the other hand, it is noticed that Pizza-slice Shaped Search Windows, for both MPSOS and MCSS, enhance the control points capability to detail vertices at concavities of the object boundary.

2.7.7 Medical test images

Magnetic Resonance Images (512 $\times$ 512 pixels) of 10 patients with brain tumors have been selected in order to test and compare the ACM strategies i.e., traditional active contour method, MPSOS and MCSS with RSSW and PSSW. Five consecutive MRI slices per patient giving a total of 50 images were used in this experiment. Tests were done by using 50 control points ($N_p = 50$), $\alpha = 0.001$, $\beta = 0.009$, $\gamma_{line} = 0.6$, $\gamma_{edge} = 0.8$ and $\gamma_{term} = 0.4$. Figure 2.19 presents 10 examples of brain tumor segmentation for each patient case, categorised into two types of tumors: *glioblastoma* (tumors 1, 2, 5, 8 and 9) and *metastasis* (tumors 3, 4, 6, 7 and 10). The first column shows initial contours used by each experiment and, from the second to the fifth column are presented the results obtained by the traditional ACM technique, MPSOS-RSSW, MCSS-RSSW, MPSOS-PSSW and MCSS-PSSW, respectively.

As mentioned at the beginning of this section, for all ten patient cases selected, five consecutive slices per patient with tumor were segmented by using the proposed method and comparative ones. Hence, for each patient, Table 2.13 depicts average metric values of these five tumors segmentations obtained by using the analysed ACM strategies. In comparison to the original snake formulation, the tests demonstrated an accuracy improvement in the use of multi-population methods in general, and specially by using the pizza-slice shaped search windows. Furthermore, for all tests done, the snake in its original formulation was in general the fastest whilst the MCSS-PSSW was the more accurate in most of cases. Table 2.14 shows the summary results of medical images segmentation through the metrics selected. An average of 74 iterations and 152.5 seconds was spent by the original snake formulation for solving the total snake energy minimisation problem. Although it was found as the fastest, it was classified as the less accurate with $J = 0.8005$, $D = 0.8867$ and $d_H = 3.6193$. Then, the ACM driven by MPSOS through the RSSW ($J = 0.8514$, $D = 0.9181$ and $d_H = 3.2101$) was outperformed by the ACM driven by MCSS through the RSSW with $J = 0.8556$, $D = 0.9207$ and $d_H = 3.2025$. Also, the methods assessment revealed an accuracy improvement of the MPSOS-PSSW outcomes ($J = 0.9067$, $D = 0.9506$ and $d_H = 2.5972$) by using the MCSS-PSSW which was found as the best one ($J = 0.9158$, $D = 0.9594$ and $d_H = 2.5792$). Likewise, it is crystal clear that the original snake formulation was faster than the multi-population strategies.

In Figure 2.20 relative computational times (RCT), considering classic gradient descend ACM as a reference, are presented. It is observed the proposed method uses the lowest RCT compared against other implemented methods (i.e., MPSOS-RSSW, MPSOS-PSSW and MCSS-RSSW). Whilst the most time demanding algorithm is MPSOS-PSSW. It is interesting to emphasise RCT follow a linear regression with respect to control points for all studied multi-population strategies. Particularly, MPSOS-RSSW, MCSS-RSSW and MCSS-PSSW have a similar tendency which means the required computational time is almost the same. Moreover, all implemented multi-population strategies spent proportional times with respect to the traditional technique. These proportional parameters depend on the control points, which were estimated and displayed in Figure 2.20.

Besides, as an additional study, six images of tumors with non-ovoid (or non-round) shapes were chosen to test the effectiveness of the proposal methodology. This kind of shapes is usually associated to malignant tumors, thus a detailed segmentation of these could avoid several post-surgery complications. Figure 2.21 shows the results achieved by segmenting the irregular tumor shape images through the multi-population strategies and the traditional method. It is visually evident that the multi-population strate-

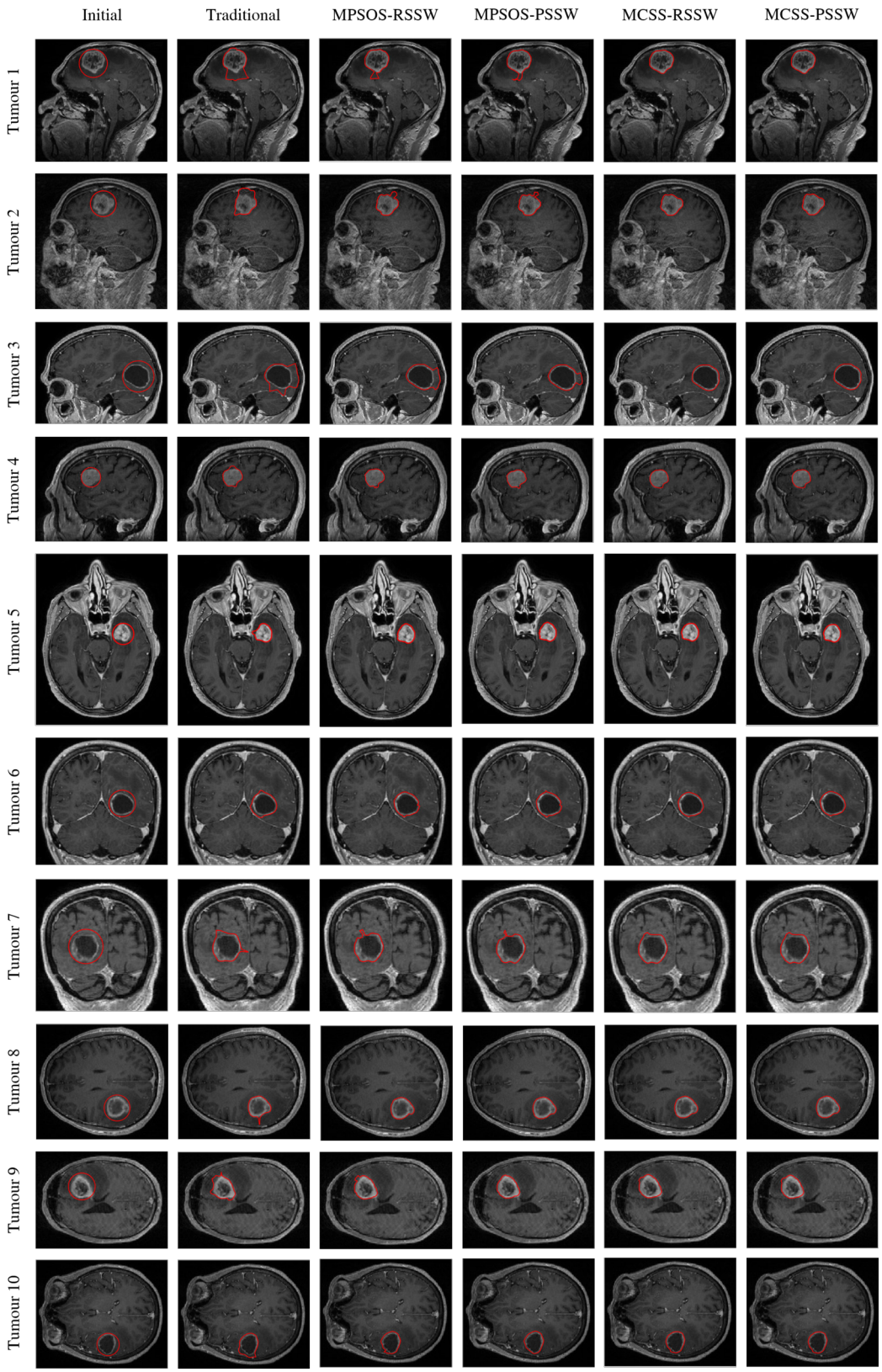

Figure 2.19: *Example of brain tumor images. Columns are organised for each tumor image as: initial contour, and contours obtained using the traditional technique, MPSOS-RSSW, MCSS-RSSW, MPSOS-PSSW and MCSS-PSSW techniques.*

Table 2.13: *Jaccard, Dice, Hausdorff, Computation time and iterations rates with their standard deviations obtained from the optimal contour of tumors in MRI images reached by using the ACM strategies, i.e., the traditional technique and multi-population methods (MPSOS and MCSS) with RSSW and PSSW. The expert is the neurosurgeon of the University Hospital, Department of Neurosurgery, University of Leipzig (Germany)*

	Strategy	J (AVG±SD$\times 10^{-3}$)	D (AVG±SD$\times 10^{-3}$)	d_H (AVG±SD$\times 10^{-3}$)	Time (s) (AVG±SD)	Iterations (AVG±SD)
1	Traditional	0.7443±80.7	0.8514±52.7	4.2358±1035.0	**291.9±15.4**	97±73
	MPSOS-RSSW	0.8119±90.5	0.8940±54.6	3.6520±1257.0	506.0±17.3	6±1
	MCSS-RSSW	0.8240±99.6	0.9009±59.9	3.6979±1287.0	557.7±19.0	9±1
	MPSOS-PSSW	**0.9471±6.9**	**0.9728±3.6**	2.2472±433.1	692.3±24.1	7±2
	MCSS-PSSW	0.9469±8.2	0.9727±4.3	**2.2408±472.6**	355.0±11.9	**5±1**
2	Traditional	0.8953±20.9	0.9446±11.6	2.7897±148.9	**250.1±13.3**	121±65
	MPSOS-RSSW	0.9042±25.0	0.9496±13.9	3.1657±472.3	451.3±15.4	5±1
	MCSS-RSSW	0.8987±16.4	0.9466±9.1	3.1041±453.5	496.6±18.5	8±1
	MPSOS-PSSW	0.9363±8.5	0.9671±4.5	**2.4240±394.2**	612.9±24.0	7±3
	MCSS-PSSW	**0.9369±9.9**	**0.9674±5.2**	2.5077±372.9	317.4±11.9	**4±0**
3	Traditional	0.7178±54.4	0.8348±36.7	4.3002±621.1	**212.2±9.8**	65±78
	MPSOS-RSSW	0.7767±80.7	0.8725±50.9	4.4790±650.7	391.0±20.8	6±1
	MCSS-RSSW	0.7939±52.4	0.8843±32.2	4.3570±877.7	439.8±16.2	8±1
	MPSOS-PSSW	**0.9282±25.4**	**0.9626±13.8**	**2.6707±764.4**	542.6±21.4	**5±1**
	MCSS-PSSW	0.9252±26.3	0.9610±14.4	**2.6707±764.4**	274.7±14.0	**5±1**
4	Traditional	0.7691±66.6	0.8682±42.2	3.2552±504.4	**138.9±14.5**	64±78
	MPSOS-RSSW	0.7701±72.8	0.8686±46.5	3.3865±815.3	235.4±15.5	5±1
	MCSS-RSSW	0.8298±87.0	0.9050±51.5	2.7829±263.6	270.3±18.6	9±3
	MPSOS-PSSW	0.9036±51.8	0.9487±29.3	**2.2663±283.0**	330.3±23.5	7±3
	MCSS-PSSW	**0.9058±49.2**	**0.9500±27.7**	2.3089±293.2	157.0±10.4	**4±0**
5	Traditional	0.8305±45.9	0.9069±27.5	3.5337±625.5	56.2±12.8	94±77
	MPSOS-RSSW	0.8798±59.5	0.9352±34.7	2.6472±490.2	87.9±14.3	6±1
	MCSS-RSSW	0.9019±18.0	0.9483±10.0	**2.5337±689.7**	93.4±17.5	9±1
	MPSOS-PSSW	0.8923±23.7	0.9429±13.3	2.8762±399.0	115.3±21.3	7±3
	MCSS-PSSW	**0.9199±21.9**	**0.9708±12.2**	2.9060±489.4	56.4±9.4	**4±1**
6	Traditional	0.8587±23.6	0.9239±13.7	3.1143±355.5	**188.4±12.0**	64±79
	MPSOS-RSSW	0.8700±37.4	0.9302±21.3	3.0566±266.7	332.3±16.4	5±1
	MCSS-RSSW	0.8582±32.2	0.9234±18.7	**2.9295±149.8**	385.2±19.5	8±1
	MPSOS-PSSW	0.8538±29.7	0.9209±17.4	3.0526±319.8	479.7±19.4	7±4
	MCSS-PSSW	**0.8851±31.6**	**0.9508±18.5**	2.9529±378.3	235.6±13.0	**4±1**
7	Traditional	0.7878±83.4	0.8793±54.6	2.5216±549.3	**117.5±11.6**	94±76
	MPSOS-RSSW	0.8379±61.9	0.9108±36.5	2.1884±513.7	188.9±14.7	6±1
	MCSS-RSSW	0.8298±67.7	0.9058±40.2	2.2753±727.1	212.4±16.2	8±1
	MPSOS-PSSW	0.8512±38.4	0.9193±22.4	2.0408±209.1	258.0±20.4	7±2
	MCSS-PSSW	**0.8827±39.7**	**0.9493±23.0**	**1.9493±336.2**	126.3±9.0	**4±1**
8	Traditional	0.8674±74.3	0.9275±44.9	4.1852±596.1	**165.6±2.2**	11±5
	MPSOS-RSSW	0.9012±27.6	0.9479±15.4	4.0182±260.6	283.5±15.4	5±1
	MCSS-RSSW	0.9049±22.0	0.9499±12.3	3.9357±371.4	328.9±19.1	9±2
	MPSOS-PSSW	**0.9249±9.1**	**0.9610±4.9**	**3.5465±527.6**	402.0±24.8	7±2
	MCSS-PSSW	0.9245±10.2	0.9608±5.5	3.5210±502.8	192.2±12.7	**4±1**
9	Traditional	0.7803±129.1	0.8716±85.6	4.009±640.4	**81.3±7.2**	38±63
	MPSOS-RSSW	0.8942±54.5	0.9435±30.6	2.9664±707.7	137.0±16.9	**5±0**
	MCSS-RSSW	0.8560±117.8	0.9187±73.6	3.3151±873.3	155.3±20.0	9±1
	MPSOS-PSSW	0.9301±13.8	0.9637±7.4	2.4461±144.9	188.9±25.7	6±1
	MCSS-PSSW	**0.9304±15.1**	**0.9639±8.0**	**2.4034±172.5**	93.4±11.9	**5±1**
10	Traditional	0.7534±60.4	0.8583±39.0	4.2488±827.3	**22.7±10.5**	95±75
	MPSOS-RSSW	0.8680±48.2	0.9288±27.7	2.5416±418.4	33.4±18.8	5±1
	MCSS-RSSW	0.8591±26.0	0.9240±15.0	3.0936±535.8	39.1±18.0	**8±1**
	MPSOS-PSSW	0.8996±18.5	0.9471±10.2	2.4020±536.7	49.4±24.8	**8 ±3**
	MCSS-PSSW	**0.9002 ±17.5**	**0.9474±9.7**	**2.3311±455.2**	24.0±12.0	5±1

Table 2.14: *Medical images: Comparison of the traditional technique, MPSOS-RSSW, MCSS-RSSW, MPSOS-PSSW and MCSS-PSSW versus an handwork of brain tumor delineation expert by using average values of Jaccard coefficient, Dice coefficient, Hausdorff distance, Computation time and iterations. The expert is the neurosurgeon of the University Hospital, Department of Neurosurgery, University of Leipzig (Germany)*

Strategy	J (AVG±SD×10^{-3})	D (AVG±SD×10^{-3})	d_H (AVG±SD×10^{-3})	Time (s) (AVG±SD)	Iterations (AVG±SD)
Traditional	0.8005±85.3	0.8867±54.3	3.6193±857.3	**152.5±83.1**	74±71
MPSOS-RSSW	0.8514±72.0	0.9181±43.5	3.2101±889.2	264.7±151.1	5±1
MCSS-RSSW	0.8556±68.3	0.9207±41.2	3.2025±883.0	297.9±167.7	9±1
MPSOS-PSSW	0.9067±398.7	0.9506±22.4	2.5972±584.2	367.1±208.1	7±2
MCSS-PSSW	**0.9158±38.8**	**0.9594±21.8**	**2.5792±592.8**	183.2±107.5	**4±1**

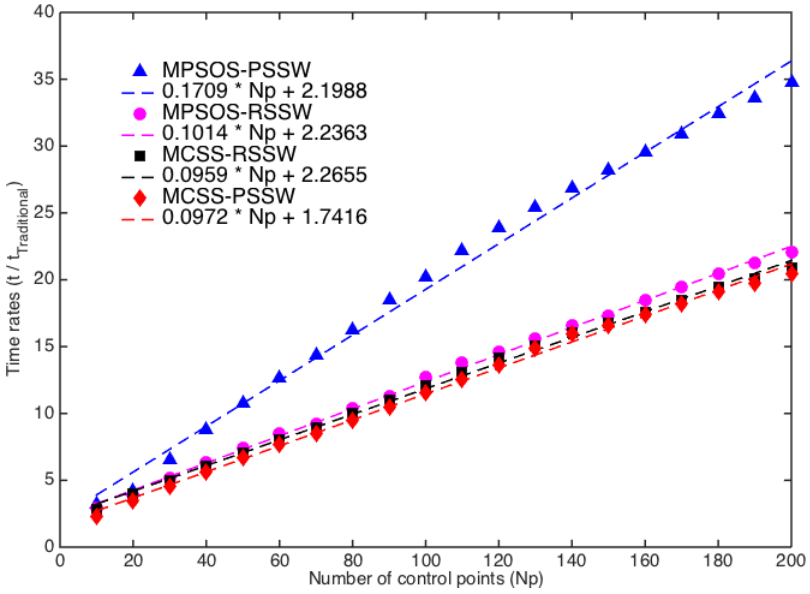

Figure 2.20: *Relative computational times versus number of control points.*

gies using PSSW reached the closest contour to tumor objects (cf. Figure 2.21). This observation was verified with the metric values $J = 0.8999$, $D = 0.9472$ and $d_H = 2.6008$ given by MCSS-PSSW, and $J = 0.8996$, $D = 0.9470$ and $d_H = 2.6008$ by MPSOS-PSSW; which are higher than the ones obtained via MCSS-RSSW ($J = 0.8470$, $D = 0.9158$ and $d_H = 3.2840$), MPSOS-RSSW ($J = 0.8320$, $D = 0.9067$ and $d_H = 3.3669$) and traditional ACM ($J = 0.7621$, $D = 0.8606$ and $d_H = 3.6137$). In addition, MCSS-PSSW found results slightly better than MPSOS-PSSW's ones. Therefore, it is noticed that multi-population strategies have a remarkable behaviour for tumor images segmentation, compared to the traditional ACM method.

Finally, it is noticed the average outcomes of the experiment carried out (synthetic and real medical images segmentation) employing MCSS enables the ACM to reach higher performance than the use of MPSOS. And based on their computational times, the comparison of ACM driven by metaheuristic optimization techniques studied in this work showed that the proposed MCSS-PSSW was the fastest. Thus, the metric values obtained are such as, in the case of RSSW, $J = 0.8741$, $D = 0.9309$, $d_H = 3.8578$, Time (s)$= 215.075$ for MPSOS versus $J = 0.8820$, $D = 0.9357$, $d_H = 3.7211$, Time (s)$= 283.3848$ for MCSS. And, in the case of PSSW, $J = 0.9192$, $D = 0.9576$, $d_H =$

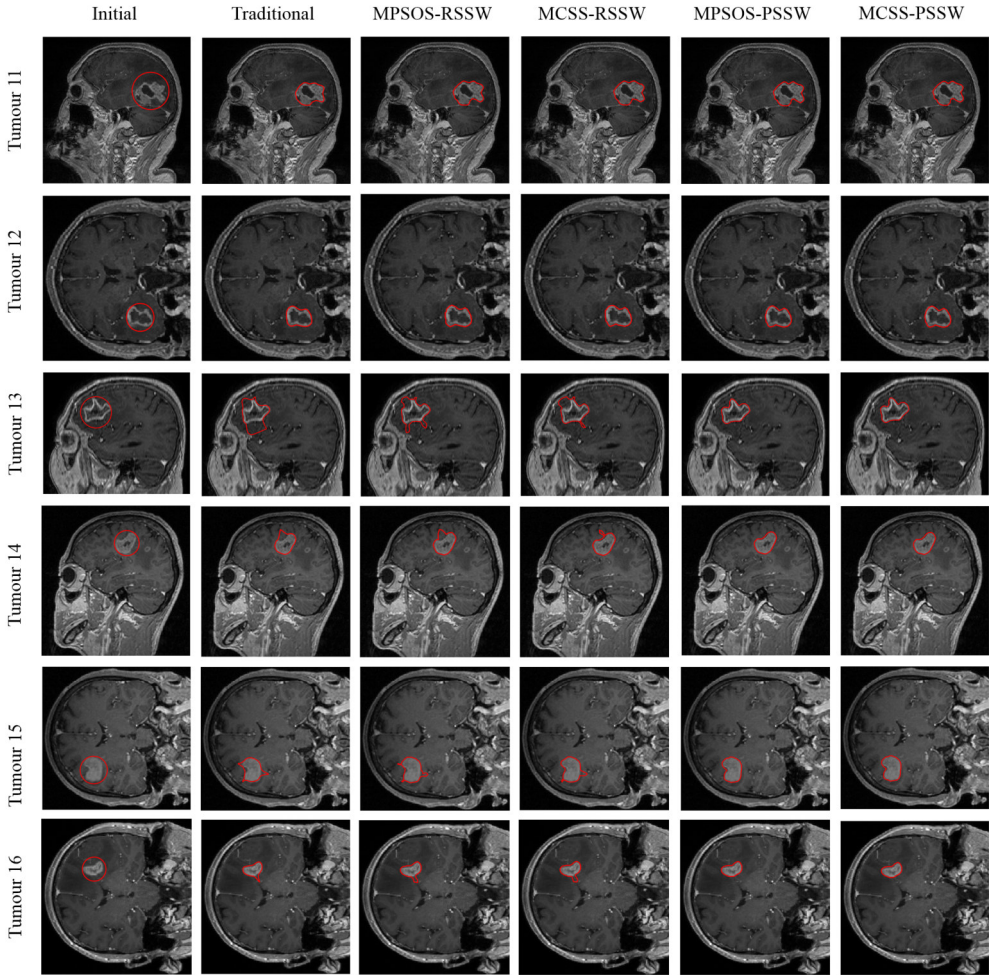

Figure 2.21: *Example of brain tumor images with irregular shapes. Columns are organised for each tumor image as: initial contour, and contours obtained using the traditional technique, MPSOS-RSSW, MCSS-RSSW, MPSOS-PSSW and MCSS-PSSW techniques.*

3.3371, Time (s)= 171.318 for MPSOS versus $J = 0.9211$, $D = 0.9592$, $d_H = 3.3168$ and Time (s)= 147.4934 for MCSS. Also, in this work, it is found that PSSW configuration consumed about 1.5 times less computational time than RSSW.

2.7.8 Conclusions

In this work, a Multi-population Cuckoo Search Strategy (MCSS) has been introduced to solve the snake energy minimisation problem for image segmentation. MCSS was successfully implemented and tested on medical images. Several human brain tumour tomographies were analysed. MCSS is an alternative approach of the traditional active contour model, which is usually solved by the gradient descent method as described earlier. The proposed method is a two stages algorithm. Here, two different search windows geometries were explored, the rectangular shaped search windows (RSSW) and the pizza-slice shaped search windows (PSSW). By using the MCSS in these kind of search windows, the new active contour model overcomes the traditional snake drawbacks, i.e., the stagnation tendency in a local minimum and the difficulty to converge in non-convex shaped objects. Nevertheless, MCSS is computationally more expensive than the traditional technique, although MCSS requires less number of iterations. The experimental results showed that the ACM driven by MCSS is robust and more efficient than the original version. In addition, the ACM guided by Multi-population Particle Swarm Optimisation Strategy (MPSOS) was implemented (with RSSW and PSSW) for comparison purposes. The results revealed that the proposed approach outperforms the comparative ACM driven by MPSOS. Besides, it has a better accuracy and requires shorter computational times. Furthermore, an additional set of experiments was performed using brain tumour images with irregular shapes, usually associated to malignant tumours. It was noticed that the proposed method (MCSS) represents a powerful alternative for the tumour images segmentation process, considering almost any kind of tumour shape. It was also demonstrated, according to some metric values, that MCSS has achieved similar results with RSSW and PSSW. However, the best performance was reached with PSSW.

Chapter 3

Brain tumor segmentation in intraoperative US data

3.1 Introduction

In this chapter, a brain tumor segmentation method in ultrasound data, based on the registration with MR models is presented. The aim is to improve the tumor visualization and to provide its geometrical parameters. The tumor segmentation in iUS images is a difficult task and still under improvement because of the low signal noise ratio. The success of automatic methods in ultrasound data is limited because of their noise sensibility. Hence, an alternative approach based on registration techniques is proposed to address this problem. Rigid and affine transformation were tested for the registration of iUS and MR Patient-specific model by using image gradient values. The method was successfully validated on a dataset of 33 patients (19 metastases and 14 glioblastoma) by comparing the tumor segmentation provided by the algorithm with manual delineations using the specificity, sensitivity, precision and Dice index. Limited computation time and interaction make the tool relevant for intraoperative use.

3.2 Related works

Ultrasound modality has become one of the most popular imaging technique in medicine. While offering the benefits of being a low cost, non-invasive and real-time imaging system, the US finds various clinical applications including diagnosis, image-guided interventions and therapy [47]. Hence, numerous studies were focused on ultrasound image segmentation, namely, for breast tumor extraction [48, 49, 50], delineating lateral ventricles of preterm neonates [51], prostate segmentation [52, 53, 54], renal delineation [55, 56, 57], blood vessels delineation in intravascular ultrasound images [58, 59], fetus segmentation [60, 61] and vertebrae extraction [62, 63].

In neurosurgery, intraoperative ultrasound imaging is used for brain tumor surgery to investigate the tumor state over time during the operation. Two-dimensional US images are commonly acquired and visualized on the monitor of the US device which offers a limited view of 3D objects. More sophisticated systems combine the US device within a navigation system and enable obtaining 3D US data [64, 65]. The examination of the brain tumor would be improved with its extraction from the 3D US image data. Hence, intraoperative brain tumor segmentation should improve the lesions visualization with respect to the surgeon for supporting the differentiation between tumor mass and other structures [66]. Furthermore, 3D visualization techniques enable to

show only anatomy of objects of interest, and geometrical parameters like tumor volume and distance to the brain surface or risk structures can be calculated. In fact, manual delineation is robust again noise. However, it is time consuming and cannot be performed in the operating room by the medical staff because of sterility constrains. On the other hand, automatic segmentation is complex in US data because of the low signal to noise ratio, artifacts, speckles, shadow, low contrast and the unclear definition of object boundaries [48, 49, 67].

Image registration is an important technique allowing to align two images. It consists by applying a proper spatial transformation to the moving image, so as to maximize the similarity measure between the moving and fixed images [68] [69]. It finds numerous applications in medicine including, ultrasoundâĂŞ-MRI brain registration [70] [71], Dynamic Contrast-Enhanced MRI (DCE-MRI) recording of moving kidney [68] [72], registering of colon surfaces extracted from prone and supine images [73], and prostate registration (in MRI-CT [74] and in MRI-transrectal US [75]). Several similarity measures were used in clinical setting in recent years. For instance, Linear Correlation of Linear Combination (LC^2) were introduced by Fuerst et al. [70] to align US slices or US volumes with MRI images. In [76], Rivaz et al. proposed to treat images as bag of words for registering MRI-US data by using the Contextual Conditioned Mutual Information (CoCoMI). Furthermore, Normalized Gradient Field (NGF) was suggested by Xu et al. [77] for the registration of real-time and prior MRI data in image-guided cardiac interventions. In the same fashion, NGF was used for nonlinear motion correction of DCE-MRI kidney time series [68].

3.3 Proposed method: patient specific model based segmentation of brain tumors in 3D-iUS

3.3.1 Patient image dataset

A total of 33 patients with different kind of tumors, 19 metastases and 14 glioblastoma cases, were included in this work. This patient data has been collected at the Department of Neurosurgery at the University Hospital of Leipzig, Germany in the context of a previous research project funded by the German Research Society (Deutsche Forschungsgemeinschaft) and accepted by the ethics commission of the University of Leipzig.

3.3.2 Preprocessing

The image filtering and histogram stretching were performed in this stage to enhance the image quality before the suggested method itself. Median filters of $3 \times 3 \times \times 3$ were used to reduce noise in the 3D-MR and 3D-iUS volumes while the histogram stretching was used to have the same contrast in the two image modalities. Let I be a given image with Min and Max its minimum and maximum intensity values. Histogram stretching consists in transforming a grayscale image I to a new one I_N such that $I : \{Min, \ldots, Max\} \rightarrow I_N : \{Min_{new}, \ldots, Max_{new}\}$. The image I_N was calculated as

$$I_N = (I - Min)\frac{Max_{new} - Min_{new}}{Max - Min} + Min_{new} \tag{3.1}$$

Technically, minimum and maximum intensity values from MR and US volumes, Min^{MR}, Max^{MR}, Min^{US} and Max^{US} were extracted. Then, the Min_{new} and Max_{new}

were computed as

$$Min_{new} = \min(Min^{MR}, Min^{US}) \tag{3.2}$$

$$Max_{new} = \max(Max^{MR}, Max^{US}) \tag{3.3}$$

3.3.3 Automatic segmentation method

The idea of the approach is to guide the iUS tumor segmentation process by using a MR patient specific model. This tumor model is obtained by semi-automatic segmentation of brain tumor in the preoperative MRI, available almost one day before the operation. If they are simply overlapped, the model is shifted relatively to the tumor in the 3D-iUS because of the brain tissue deformation. Therefore, the model has to be registered with the 3D-iUS data (Figure 3.1).

Local approach

The proposed system is described in Figure 3.2. It can be observed that, a region of interest is automatically defined based on the MR model and applied on the iUS volume. The aim of this local approach is to process only the MR and iUS sub-volumes containing expected features so as to minimize noises. By this way, the computation time is also optimized. The ROI size is such that it encloses not only the model, but it includes also a neighborhood of elven voxels in each direction in order to take into account the brain shift.

Extraction of hyperechogenic structures

Before the image registration itself, highlighted structures contained in the ROI, mainly tumor, are extracted by using the Otsu multilevel thresholding technique [**?**][33] in both modalities (MRI and iUS). The threshold levels in the Otsu method are settled to two. Therefore, based on their intensity values, voxels of MRI and iUS volumes are classified in three classes: background, brain tissues and hyperechogenic structures. Tissue classified in the high-level intensity class (third one) are kept for the registration.

Automatic registration

The proposed registration approach is conducted on extracted binary structures. Most of similarity measures are based on comparison of statistical intensity information. However, by registering binary structures, the NGF are selected here because it allows to align objects using a distance measure based on computed angles. Thus, the transformations are carried out based on gradient values used as key features in the registration process. Applied on binary volumes, the gradients computed inside the volume are zero. Only the edges contribute in the gradient calculation. In order to evaluate the performance of the proposed method, rigid and affine transformations are tested. Finally, the obtained transformation matrix T is applied on the MR model to align it to the tumor in the 3D-iUS. Consequently, the aligned patient specific model enables to improve the visualization of the tumor in iUS by highlighting the tumor borders.

The rigid and affine transformations have six and twelve degree of freedom, respectively. They are described by the following equation

$$T_{Rigid} = T_{trans}(t_1, t_2, t_3)T_{rot}(\theta_1, \theta_2, \theta_3) \tag{3.4}$$

$$T_{Affine} = T_{trans}(t_1, t_2, t_3)T_{scale}(\alpha_1, \alpha_2, \alpha_3)T_{rot}(\theta_1, \theta_2, \theta_3)T_{shear}(\beta_1, \beta_2, \beta_3) \tag{3.5}$$

where T_{Rigid} and T_{Affine} are rigid and affine transformations. Moreover, T_{trans}, T_{scale}, T_{rot} and T_{shear} are matrices of translation, scaling, rotation and shearing, respectively. The parameters t, α, θ and β represent the degree of freedom in the transformation.

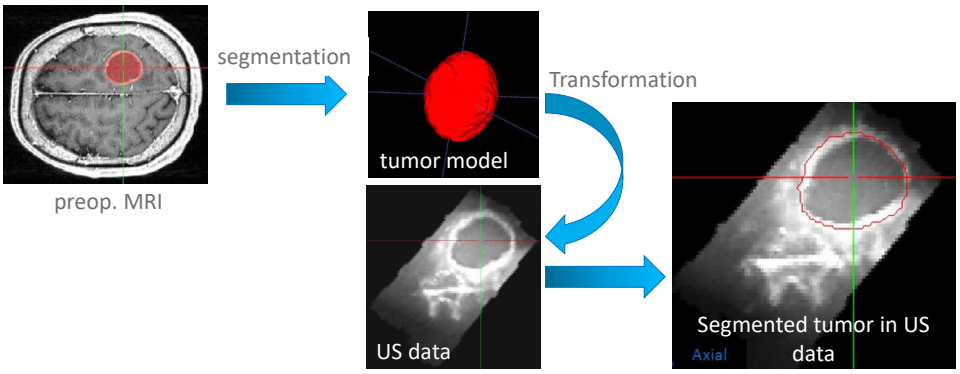

Figure 3.1: *Concept of patient specific MR model based tumor segmentation in iUS.*

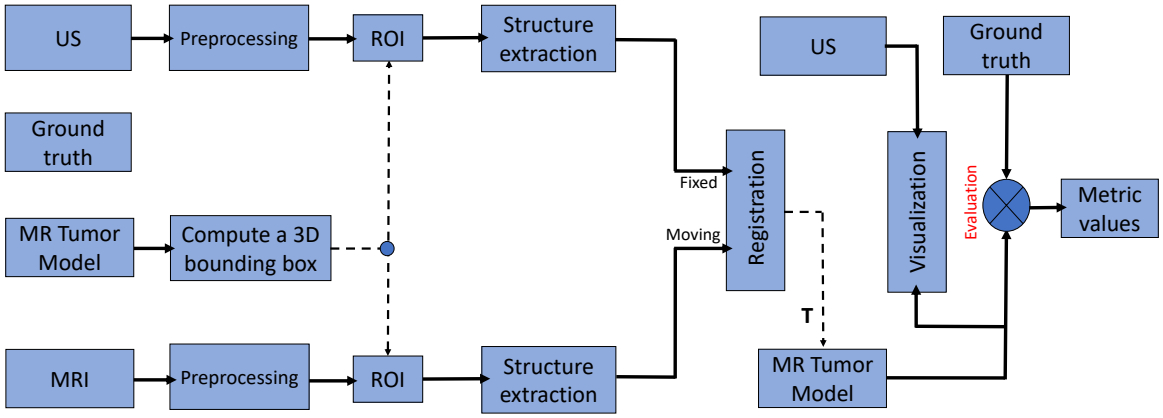

Figure 3.2: *Automatic tumor segmentation approach in iUS.*

Normalized gradient field

The Normalized Gradient Fields, proposed by Haber and Modersitzki [78] [79], is defined by the following distance measure

$$D(I_m, I_f) = -\frac{1}{2}\int_{\Omega} < \hat{\mathbf{n}}(I_m, x), \hat{\mathbf{n}}(I_f, x) >^2 dx \tag{3.6}$$

where I_m and I_f are the moving and fixed images, respectively. The normalized gra-

dient $\hat{\mathbf{n}}$ of the image I is computed as

$$\hat{\mathbf{n}}(I,x) := \begin{cases} \frac{\nabla I(x)}{||\nabla I(x)||\epsilon} & \nabla I(x) \neq 0; \\ 0 & otherwise. \end{cases} \tag{3.7}$$

where $||\nabla I(x)||\epsilon = \sqrt{\nabla I(x)^T \nabla I(x) + \epsilon^2}$ and ϵ is a soft thresholding that minimizes the effects of small gradients due to noise.

So, the registration process will consists in finding the transformation $T : \mathbb{R}^3 \rightarrow \mathbb{R}^3$ that minimizes the distance D as: $\arg\min_T \{D(I_m[T], I_f)\}$ (see [77]).

3.4 Experimental results and disccusion

This section provides the experimental results of the evaluation of the proposed iUS segmentation method. The implementation was performed using the Mevislab platform. Thirty-three patients, 19 with metastasis and 14 with glioblastoma, were included in this work. Four metrics were used for the quantitative assessment of the results, namely, the specificity (Spe), sensitivity (Sen), precision (Pre) and Dice coefficient (D).

3.4.1 Method accuracy evaluation

Figure 3.3 illustrates how the MR model does not match with the tumor in iUS before registration and how they become aligned after registration by using the proposed framework. The 2D and 3D images depict the position of the MR tumor model before and after registration.

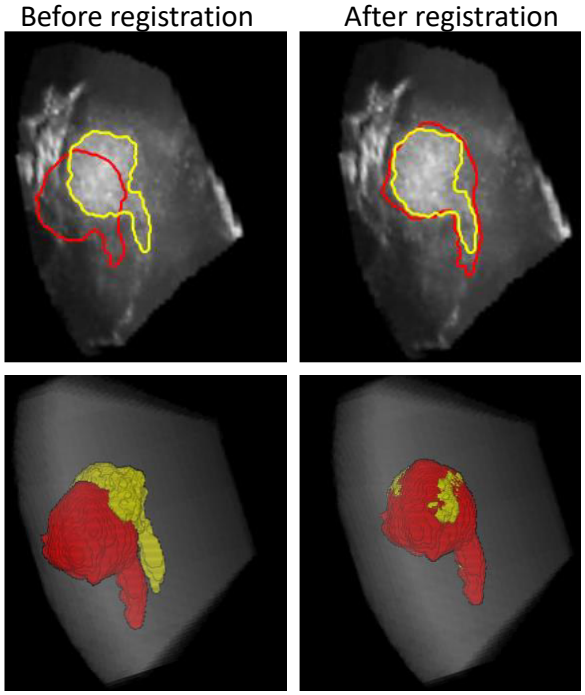

Figure 3.3: *Patient 3 (Glioblastoma cases). Position of the tumor model before and after registration. The ground truth is depicted in yellow and the tumor model in red.*

Figure 3.4 presents the segmentation results obtained for eight patients with metastasis. The algorithm outcomes (in red) and the ground truths (in yellow) are overlaid on a selected slice of the 3D-iUS images for visualization purposes. It can be observed that the segmentation results follow the manual delineations. Table 3.1 summarizes the outcomes achieved by using the proposed segmentation approach with the rigid and affine transformation.

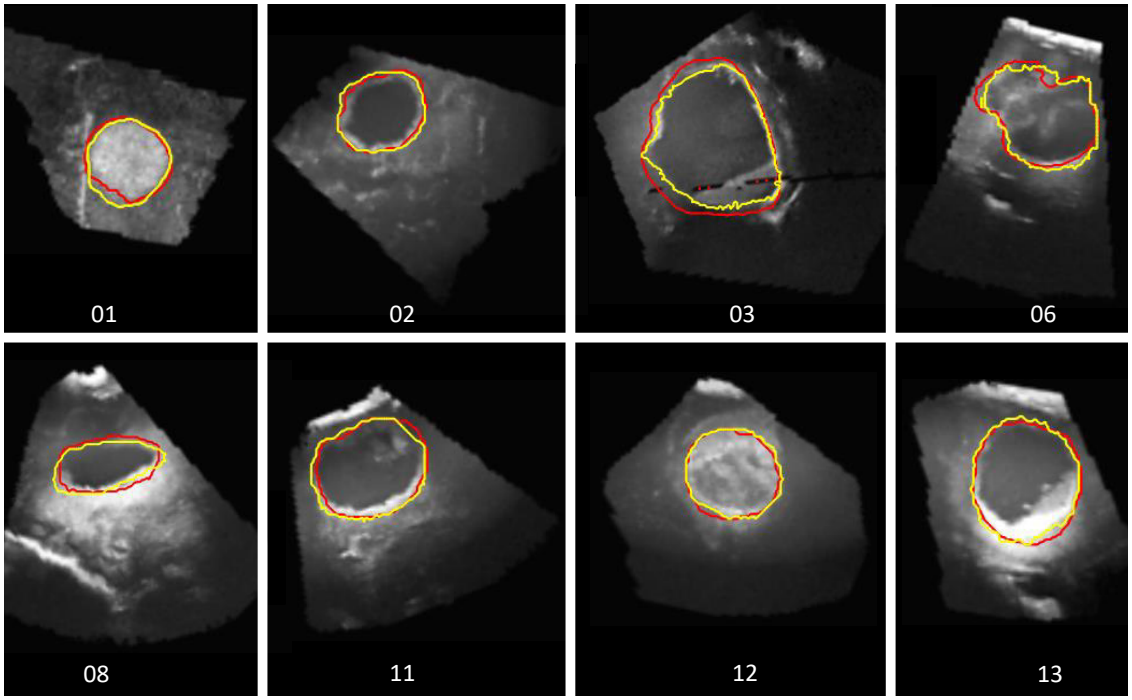

Figure 3.4: *Automatic segmentation of brain tumor metastasis in eight 3D-iUS patient data. The ground truth is depicted in yellow and the obtained result in red.*

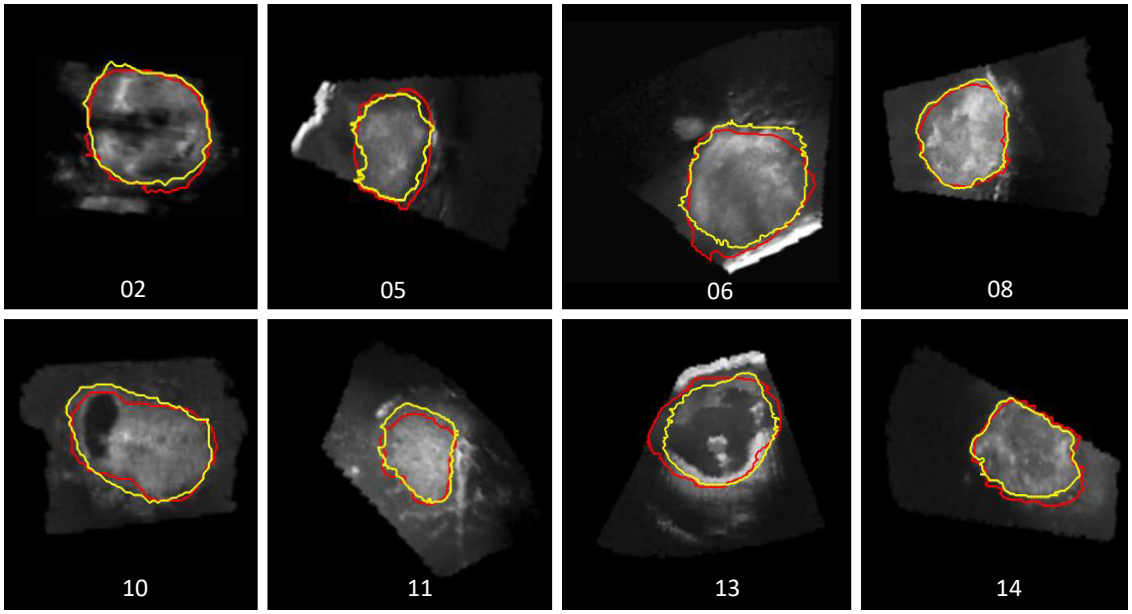

Figure 3.5: *Segmentation results of brain tumor glioblastomas in eight 3D-iUS patient data. The ground truth is depicted in yellow and the obtained result in red.*

Table 3.1: *Metric values achieved for patients with metastasis. The accuracy rates before the registration (initial) are compared to those of results obtained by using the proposed local binary registration approach. Rigid and affine transformations are tested.*

	Initial				Rigid				Affine			
Patient	Spe	Sen	Pre	D	Spe	Sen	Pre	D	Spe	Sen	Pre	D
1	0.9997	0.5367	0.5280	0.5323	0.9999	0.8461	0.8324	0.8392	0.9998	0.8592	0.7970	0.8270
2	0.9996	0.8000	0.7582	0.7788	0.9997	0.9039	0.8560	0.8793	0.9998	0.9133	0.8704	0.8913
3	0.9998	0.6649	0.7957	0.7244	0.9998	0.6646	0.7980	0.7252	0.9999	0.7734	0.9272	0.8434
4	0.9980	0.8150	0.6085	0.6988	0.9986	0.9794	0.7314	0.8374	0.9988	0.9641	0.7630	0.8519
5	0.9996	0.2972	0.4235	0.3493	0.9999	0.6226	0.8885	0.7321	0.9998	0.5226	0.7483	0.6154
6	0.9996	0.6822	0.7773	0.7267	0.9998	0.8883	0.8811	0.8847	0.9997	0.8642	0.8654	0.8648
7	0.9986	0.8556	0.6089	0.7115	0.9986	0.9008	0.6308	0.7420	0.9988	0.9597	0.6824	0.7976
8	0.9993	0.8440	0.6153	0.7118	0.9995	0.9279	0.7157	0.8081	0.9995	0.9260	0.7143	0.8065
9	0.9998	0.5251	0.5641	0.5439	0.9999	0.6759	0.7261	0.7001	0.9999	0.7300	0.7842	0.7561
10	0.9998	0.6589	0.5923	0.6239	0.9998	0.7126	0.5937	0.6478	0.9998	0.8872	0.7195	0.7946
11	0.9993	0.5273	0.5848	0.5546	0.9996	0.7144	0.7920	0.7512	0.9999	0.8492	0.9626	0.9023
12	0.9997	0.7036	0.7880	0.7434	0.9998	0.8255	0.9245	0.8722	0.9998	0.8019	0.8982	0.8473
13	0.9994	0.6213	0.6735	0.6464	0.9997	0.8075	0.8713	0.8382	0.9996	0.7396	0.7978	0.7676
14	0.9967	0.8291	0.7051	0.7621	0.9975	0.9279	0.7803	0.8477	0.9974	0.9350	0.7749	0.8475
15	0.9968	0.8715	0.7649	0.8147	0.9975	0.9339	0.8152	0.8705	0.9972	0.9329	0.7958	0.8589
16	0.9992	0.9030	0.7830	0.8387	0.9993	0.9382	0.8135	0.8715	0.9994	0.9279	0.8286	0.8754
17	0.9988	0.5143	0.4924	0.5031	0.9995	0.8400	0.8045	0.8219	0.9994	0.8067	0.7773	0.7917
18	0.9972	0.8414	0.6764	0.7500	0.9973	0.8437	0.6869	0.7573	0.9973	0.8414	0.6855	0.7555
19	0.9987	0.9504	0.7571	0.8428	0.9989	0.9832	0.7811	0.8706	0.9988	0.9743	0.7758	0.8638
Average	0.9989	0.7074	0.6577	0.6766	0.9992	0.8388	0.7854	0.8051	0.9992	0.8531	0.7983	0.8189

Table 3.2: *Metric values achieved for patients with glioblastoma. The accuracy rates before the registration (initial) are compared to those of results obtained by using the proposed local binary registration approach. Rigid and affine transformations are tested.*

	Initial				Rigid				Affine			
Patient	Spe	Sen	Pre	D	Spe	Sen	Pre	D	Spe	Sen	Pre	D
1	0.9990	0.5512	0.6655	0.6030	0.9991	0.6689	0.7332	0.6996	0.9993	0.7078	0.7735	0.7392
2	0.9982	0.3586	0.4265	0.3896	0.9983	0.5496	0.5496	0.5451	0.9991	0.7546	0.7714	0.7629
3	0.9995	0.3702	0.2895	0.3249	0.9997	0.8693	0.6798	0.7630	0.9997	0.8619	0.6689	0.7532
4	0.9989	0.6032	0.6360	0.6192	0.9990	0.6126	0.6510	0.6312	0.9993	0.7311	0.7582	0.7444
5	0.9995	0.9286	0.8025	0.8610	0.9995	0.9275	0.7822	0.8487	0.9995	0.9162	0.7766	0.8406
6	0.9976	0.6787	0.6420	0.6598	0.9981	0.7782	0.7198	0.7479	0.9980	0.7913	0.7100	0.7485
7	0.9969	0.4512	0.5461	0.4941	0.9988	0.6773	0.8253	0.7440	0.9958	0.2697	0.3424	0.3018
8	0.9987	0.6215	0.6636	0.6418	0.9997	0.8714	0.9291	0.8993	0.9996	0.8413	0.9093	0.8740
9	0.9975	0.8527	0.6792	0.7561	0.9976	0.8576	0.6848	0.7615	0.9979	0.8750	0.7208	0.7904
10	0.9994	0.5334	0.7683	0.6297	0.9994	0.8731	0.8575	0.8652	0.9995	0.8570	0.8851	0.8708
11	0.9997	0.8611	0.7923	0.8253	0.9997	0.8545	0.7859	0.8188	0.9996	0.8101	0.7454	0.7764
12	0.9980	0.8668	0.6666	0.7536	0.9980	0.8809	0.6619	0.7559	0.9980	0.8986	0.6723	0.7692
13	0.9978	0.7841	0.6892	0.7336	0.9985	0.8891	0.7928	0.8382	0.9987	0.8981	0.8199	0.8572
14	0.9990	0.8671	0.6771	0.7604	0.9991	0.9105	0.7207	0.8045	0.9992	0.9223	0.7294	0.8146
Average	0.9985	0.6663	0.6388	0.6465	0.9988	0.8014	0.7409	0.7659	0.9988	0.7953	0.7345	0.7602

Figure 3.5 shows the segmentation results reached in the case of eight patients with glioblastoma. The outcomes reached by the proposed algorithm (in red) and the ground truths (in yellow) are superimposed for illustration. It is difficult to draw the limits of this kind of tumors. However, the outcomes reveal that the tumor boundaries can be outlined in a promising manner, and the discrimination between healthy and tumorous regions is enhanced. Table 3.2 presents the outcomes obtained by using the suggested segmentation approach with the rigid and affine transformation.

Experiments showed that the proposed method is effective for segmenting tumor in 3D-iUS by using the patient specific model. In general, the quantitative evaluation supports the visual observation. Also, it reveals how the final results are improved compared to the initial tumor position. The mean rate values from initial contours are $Spe = 0.9989$, $Sen = 0.7074$, $Pre = 0.6577$, $D = 0.6766$ for metastasis and $Spe = 0.9985$, $Sen = 0.6663$, $Pre = 0.6388$, $D = 0.6465$ for glioblastoma. It was found that there is no significant difference between the outputs reached through the two types of transformations. For metastasis cases, mean values of $Spe = 0.9992$, $Sen = 0.8388$, $Pre = 0.7854$, $D = 0.8051$ and $Spe = 0.9992$, $Sen = 0.8531$, $Pre = 0.7983$, $D = 0.8189$ were obtained for the rigid and the affine transformations, respectively. In the same fashion, the average rates of $Spe = 0.9988$, $Sen = 0.8014$, $Pre = 0.7409$, $D = 0.7659$ and $Spe = 0.9988$, $Sen = 0.7953$, $Pre = 0.7345$, $D = 0.7602$ were achieved for glioblastoma by testing the two mentioned transformations, respectively. These results show that our approach is able to correctly delineate tumorous tissues in 3D-iUS. The achieved values in the metastasis segmentation are higher than those obtained in the glioblastoma delineation can be explained by the difference in the representation of these two kinds of tumors in B-mode ultrasound. Metastases are encapsulated tumors whose boundary is well depicted. In case of image artifacts, the model enables to supplement the missing boundary information. Whereas, glioblastomas are diffused tumors whose margins can look blurred in B-mode US. Thus, the contour delineation of this types of tumors is difficult.

The automatically segmented tumor matches more accurately the manually delineated tumor for metastasis than for glioblastomas. Metastasis boundary is generally sharply represented in B-mode US imaging. This explains the great success of the method. On the other hand, glioblastoma boundary looks blurred in B-mode US. The manual delineation itself is in this case a complex task and represents a limitation in terms of accuracy in the validation method. The task was supported by the use of preoperative MR data.

The main advantage of the tumor model is the ability to locally supplement missing boundary information mostly due to image artifacts. Based on automatic thresholding technique, the relevance of the method is dependent of image quality. For example, in the case of glioblastomas, the missing highlighted borders can lead to the method failure. One of the strong point of the suggested method is that binary elements used for registration included not only tumor tissues, but also surrounding hyperechogenic structures like blood vessels and cerebral falx. Thus, it is important to note that the size of the ROI plays a major role in the registration process. A big ROI is preferable for taking into account large deformation and several surrounding hyperechogenic structures. But, according to the tumor position, it could lead to the extraction of many noises and the failure of the method. In the contrast, a small ROI is concentrated to tumorous tissues and can lead to the failure of the method in case of lack of information. The ROI defined by adding eleven voxels in each direction was experimentally found as a good trade-off between these two constraints.

3.4.2 Computation time assessment

The experiments were conducted in a personal computer with the following specifications: CPU Intel® Pentium™ 1.9 GHz, 4 GB of RAM, Microsoft® Windows™ 10 and 64-bit operating system. The proposed registration methodology used for tumor segmentation is referred here as local binary approach or simply local approach. Registration of entire 3D-MR and 3D-iUS volumes were also used to evaluate the overlap of tumors from these two modalities. And, it is presented as traditional approach. The computation time necessary to obtain segmentation outcomes by employing the local binary and traditional approach were calculated. It was found that, for rigid transformation, an average time of 1.925 and 639.75 seconds were respectively spent by using the first and the second approach. And, for affine transformation, a mean time value of 7.25 seconds was spent employing the local binary approach versus 2878.75 seconds using the traditional approach. These results reveal clearly two points. First, the rigid transformation is performed in a lower time than the affine transformation. This observation is sustained by the fact that, twelve degrees of freedom are allowed in affine transformation while there is only six for rigid transformation. Second, the proposed local binary approach consumes lesser time versus the traditional approach. The time required to obtain results, in the traditional approach, depends on the total size of the volume. However, in the local binary approach, it depends only on the size of the specific model of the MR patient.

3.4.3 Proposed method versus traditional approach

Additional experiments were carried out in order to compare the segmentation performances reached through the proposed method and the traditional approach. This comparison was performed in term of Dice indexes. Figures 3.6 and 3.7 present the results, which report the comparison between the proposed method and the traditional approach, obtained from patients with metastasis and glioblastoma, respectively.

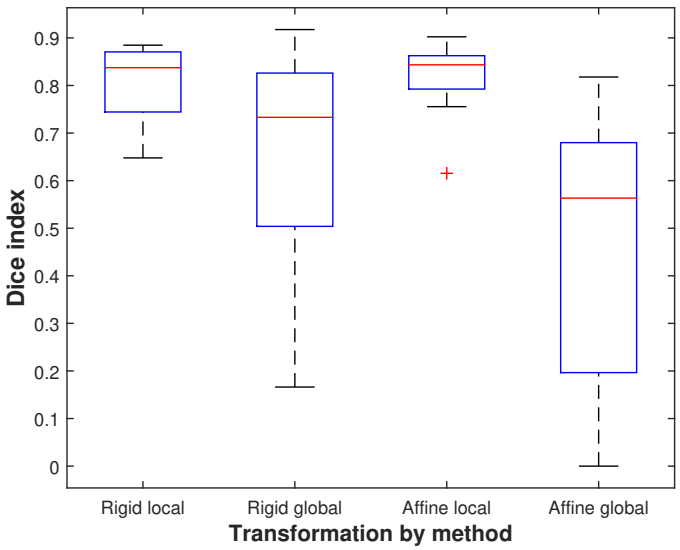

Figure 3.6: *Dice indexes comparison between the proposed method and the traditional approach. Rigid and affine transformations were tested on the dataset of patients with metastases.*

It can be clearly observed that the local method achieves higher Dice coefficients

than the traditional approach for any transformation type and for each kind of tumor. In the case of patients with metastasis and for rigid transformation, the mean Dice coefficient of 0.8051 was obtained by using the suggested approach versus 0.6551 employing the comparative method. And, regarding affine transformation, the average Dice values of 0.8188 versus 0.4565 were obtained by using the local binary approach and the comparative method, respectively. In the case of patients with glioblastoma and for rigid transformation, the average Dice coefficient of 0.7659 was reached via the proposed method versus 0.5691 achieved by the traditional approach. And, concerning affine transformation, the mean Dice indexes of 0.7602 versus 0.5945 were obtained via the suggested and the comparative method, respectively.

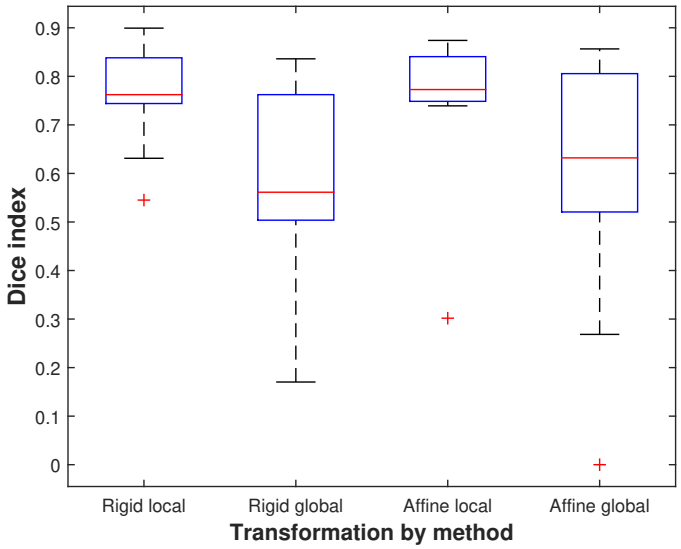

Figure 3.7: *Comparison of Dice rates from the proposed method and the traditional approach. Rigid and affine transformations were tested on the dataset of patients with glioblastoma.*

3.5 Conclusion

In this chapter, a local method for brain tumor segmentation in 3D-iUS data based on the patient specific MR model was presented. The method has consisted in registering the MR tumor model available almost one day before the operation with the tumor in iUS. To achieve this goal, first, a region of interest enclosing the model was automatically defined. Eleven voxels were added in each direction to find a ROI taking into account the brain shift deformation in iUS. Thus, the ROI size was enough large to include the tumor location in iUS. Second, the hyperechogenic structures contained in the ROI and from both modalities (MRI and iUS) were extracted by using the Otsu segmentation method. Third, these binary structures were registered based on gradient values used as key features in the registration task. By using the NGF similarity measure, the rigid and affine transformations were used for testing the method. The experiment results showed that the proposed approach was able to correctly segment the brain tumor in iUS. In the case of metastases, average Dice values of 0.8051 and 0.8189 were reached by employing the rigid and affine transformations, respectively. For patients with glioblastoma, average Dice values of 0.7659 and 0.7602 were reached by using the rigid and affine transformations, respectively. These achieved

rates demonstrate how the initial Dice values 0.6766 and 0.6465 are increased using the proposed method.

Chapter 4

Automatic Identification of Residual Brain Tumors

4.1 Introduction

In the context of brain tumor surgery, residual tumors are still a problem for neurosurgeons. Due to the invasiveness of the treatment and the fact that tumor remnant cells are potential sources of new tumor growth; the removal of the maximum quantity of these abnormal cells is important to save lives. Thus, after initial resection, the real-time tissue analysis is fundamental for supporting the physician decision about the presence or absence of residual tumor cells. We propose an image processing approach that can provide additional information for helping to improve medical decision. In fact, tumor tissues and vessels are highlighted in CEUS while the resection cavity is depicted well in B-mode US. By combining this relevant information, the brain structures could be discriminated and classified as residual tumor. Besides during surgery, the mental representation of the information obtained from these two modalities is difficult for neurosurgeons, and the proposed image fusion technique might be an adequate alternative. The method was tested on an image dataset of 23 patients suffering from glioblastoma. The detection rate of brain areas with tumor residuals reached by the algorithm was qualitatively and quantitatively compared with manual annotations provided by experts. The results showed that the assistance tool was able to successfully identify areas with suspicious tissue.

4.2 Theory

In neurosurgery, intraoperative ultrasound (iUS) imaging provides the benefit of real time visualization of the brain anatomical structures. Ultrasound devices have the advantage of being easy to use in the operating room. Hence, extra image acquisitions may modify the surgical workflow a little. Additionally, they are relatively low costs in comparison to other medical imaging systems. This intraoperative modality is routinely used to guide brain tumor operations. Particularly, iUS aims at identifying the presence of possible tumor residuals at the end of the operation, in order to remove as much tumor tissue as possible [80, 81]. This is a crucial aspect since several studies showed that a gross-total resection has a positive impact on the progression-free survival of patients.

Intraoperative B-mode ultrasound (iB-mode) remains the most popular modality used to support brain tumor surgery but is not always suitable. Hence, specific brain

tumors (e.g. the glial tumors) are often represented by a weak contrast and the exact position of tumor boundaries is hard to define. Furthermore, the tumor residuals, which are located beyond the borders of the resection cavity, are hardly differentiable from blood and artifacts. The use of an ultrasound contrast agent to enhance brain tumor tissue and residual tumor is currently being developed. The technique is not new; contrast enhanced ultrasound (CEUS) imaging is routinely performed and it was already tested in other medical areas like breast tumor diagnosis [82, 83], liver lesions [84, 85], renal masses [86, 87, 88] or blood vessels identification [89, 90, 91]. Additionally, improvements of brain tumor tissues and tumor residuals enhancement by using CEUS was effectively demonstrated by several recent studies [92, 93, 94, 95, 96].

However, the identification of tumor residuals in the iUS data remains in general complex for the expert-eye. Depending on the position of the tumor within the patientâĂŹs head, the resection cavity as well as other cerebral structures like blood vessels; potentially ventricles and bone structures are usually well depicted in the iB-mode image data. But the possible tumor residuals are hardly differentiable from other hyperechogenic structures, like the border of the resection cavity, blood or artifacts (Figure 4.1 left). Furthermore, only the blood vessels and vascularized structures, like tumors, are attempted to be enhanced in the iCEUS image data. Also, the borders of the resection cavity, which are important structures that are needed to analyze the images correctly, are hardly or not visible (Figure 4.1 right). Combination of the information in the iB-mode and iCEUS image data, also called data fusion, can support the identification of tumor residuals.

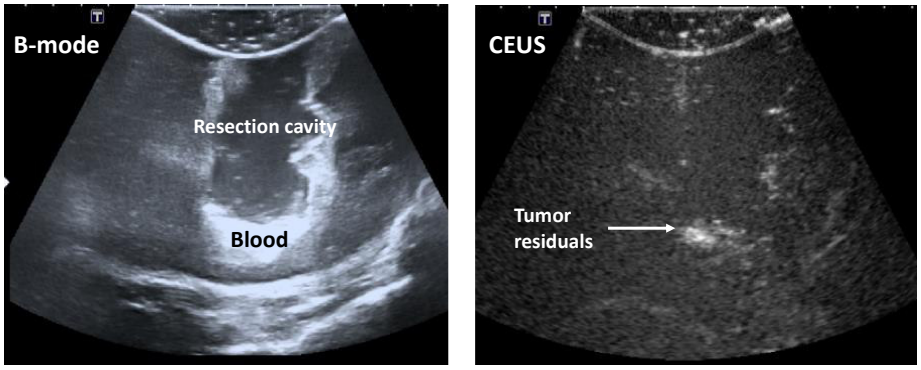

Figure 4.1: *Intraoperative B-mode ultrasound (iB-mode) (**left**) and iCEUS (contrast enhanced ultrasound (CEUS)) (**right**) patient image data acquired at the end of a brain tumor operation.*

Image fusion consists of combining relevant information from various source images of the same scene into a single resulting image called the "fused image". The aim of fusion is to preserve specific details of the source images within the fused image to obtain a better representation and understanding of the scene. In theory, three levels of image fusion can be distinguished: the pixel level, the feature level and the decision level [97, 98]. The initial level is known as the lowest level because it directly involves the pixels of the source images. The second level utilizes features or objects extracted from source images. The highest level involves decision rules. This technique is largely used in many applications like remote sensing [99, 100], computer vision [101, 102] and medical imaging [103, 104]. In the medical field, image fusion is mainly applied to provide a high quality in patient data representation by using images from different modalities. The objectives of image fusion are mainly the improvement of the image's contrast and rectification of image degradation. Image fusion is performed using various fundamental methods. Das et al. [105] combined a

non-subsampled contourlet transform (NSCT) with a reduced pulse-coupled neural network and fuzzy logic technique to overcome the image fusion problems such as contrast reduction and image degradations. Zhu et al. employed a dictionary learning approach [106]. Due to the limited and redundant information in image patches created by using traditional dictionary learning methods, an alternative scheme of image patch sampling and clustering was proposed. Then, the K-SVD algorithm was used for training of patch groups into compact sub-dictionaries, which were then combined into a complete dictionary. Furthermore, a multimodal (CT/MRI) image fusion method based on NSCT was introduced by Bhatnagar et al. [107]. The resultant low and high-frequency coefficients were respectively combined through the phase congruency and directive contrast-based models. Then, the inverse NSCT was applied on composite coefficients to recover the fused image. Since nature-inspired techniques became popular in computer vision, they have been applied extensively in medical image fusion. Xu et al. [108] have fused multimodal medical images by means of adaptive pulse-coupled neural networks (PCNN). They proposed automatic and optimum parameters tuning of the PCNN model by using the quantum-behaved particle swarm optimization algorithm. In the same fashion, the swarm intelligence of the ant colony and neural network was used for fusing images from PET, MRI, SPECT and MRI modalities [109]. The loss of edges and directional information often occurs during feeding of neural network inputs. Therefore, to solve this problem, the ant colony optimization and statistical scaling techniques were respectively used to detect and enhance the image's edges before the neural network training and testing. Above all, the image fusion has demonstrated its effectiveness for planning and intraoperative interventions, especially in neurosurgery. Fusion techniques allow, in this context, augmenting the visualization of anatomical structures that are depicted only in one imaging modality or to monitor in time the evolution of a disease. For instance, the CT-MR fusion images were used by Nemec et al. [110] for supporting the surgeon to improve the surgical performance of temporal bone tumors. Furthermore, Prada et al. [111] presented the fusion imaging between preoperative MRI and iUS for intra-operative ultrasound-based navigation in the context of brain tumor removal. The combination of the MRI, characterized by good spatial resolution and a wide field of view, and the iUS that provides real-time status of the brain enables improvement of surgical outcomes. By the same token, an interesting review concerning image fusion for precise target detection in radiosurgery, neurosurgery and hypofractionated radiotherapy was presented in [112]. It is pointed out that the mixture of images such as MR and CT is useful to avoid the damage to the nerves and blood vessels, to accurately locate tumors and to follow-up on the postoperative treatment.

4.3 Main contributions

In this technical paper, we are concerned with the development of an image-processing approach to aid the surgeon with the identification of brain areas including residual brain tumor based on both 3D iB-mode and 3D-iCEUS imaging. Our approach retraces the neurosurgeon's process for interpreting the iUS image data. It is based on two assumptions. The tumor residuals are located beyond the resection cavity wall (for patients who overcame a gross total resection). Additionally, the tumor residuals are enhanced in the iUS image data. However, they are hardly distinguishable from blood, cavity borders and artifacts in the iB-mode image data. Therefore, the method consists of extracting relevant information from both iB-mode and CEUS modalities using auto-

matic segmentation techniques and of fusing them according to rules to keep the tumor residuals. This procedure corresponds to the second and third level fusion methods. In the proposed methodology, the suspect tissues are overlaid on the original 3D B-mode US to facilitate clinical interpretation. In this way, the physician decision regarding the tumor removal task can be optimized. To the best of available knowledge, this is the first time that a computer-assisted approach has been proposed to aid neurosurgeons in the detection of residual tumor cells based on iUS imaging. However, it is important to note that this work was tested "offline" on a limited database of patient images.

4.4 Proposed method: Image Fusion for Residual Brain Tumor Identification

4.4.1 Patient Image Dataset

Twenty three patients with glioblastoma WHO Grade IV, who overcame a gross total or subtotal resection, were included in this "offline" analysis based on intraoperative ultrasound images. Glioblastomas are tumors that infiltrate the brain tissues, and their borders with healthy tissues are unclear. Therefore, the removal of the whole tumor is a complex task for the surgeon. Possible tumor residuals in the 3D i-Bmode and iCEUS data were manually segmented by four experts (neurosurgeons and scientists), who have had experience with intraoperative ultrasound imaging of brain tumors. The task was performed using radiological findings and postoperative MR image data. For four patients, no tumor was visible in the iUS and MR image data. Radiological findings are medical reports provided by radiologists in which possible operation complications (for example blooding) and the presence of possible remnants of tumor tissue are described. These reports are routinely achieved based on postoperative MR data.

4.4.2 Image Fusion for Residual Brain Tumor Identification

The approach to automatically identify tumor residuals based on iUS image data is depicted in (Figure 4.2). It consists of automatically segmenting target structures in the image data and then of optimally fusing them to keep only those that provide relevant information. The target structures, i.e., the residual tumors, are highlighted in both B-mode and CEUS modalities. Therefore, gray-level intensities were chosen as the feature for extracting tumor tissue.

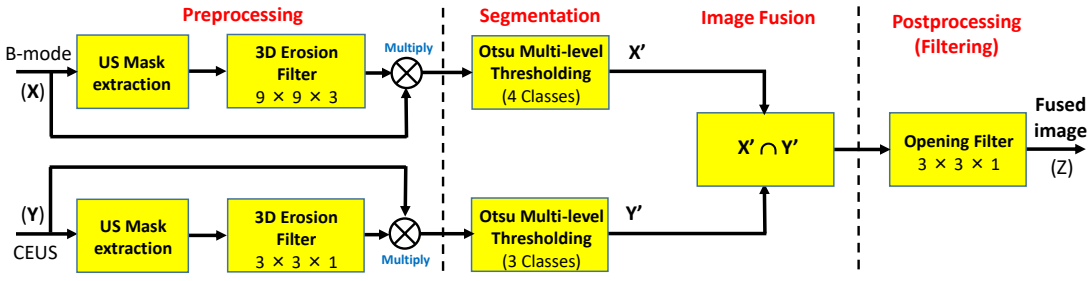

Figure 4.2: *Image processing approach for brain tumor residual identification. The method is subdivided into four main steps. First, an image preprocessing is performed for removing the ultrasound image border by using erosion filters. Second, highlighted structures are extracted in both imaging modalities by applying the Otsu multi-level thresholding method. Third, segmented structures are combined via a fused rule defined by Equation (4.1). Finally, a post-processing stage is performed to remove small structures detected that are in general false positives.*

A preprocessing stage was previously carried out by extracting foreground masks for both images (i.e., B-mode and CEUS). Given an image $I(i,j,k)$ where the background contains voxels of value zero, the mask M is obtained as $M = I(i,j,k) > 0$. Then, erosion filters (with cubic/quadratic structuring elements of $9\times9\times3$ and $3\times3\times1$ for B-mode and CEUS, respectively) were applied on these masks. The multiplication of original images by the filtered masks was performed for removing artifacts located at the image's border and due to the contact of the ultrasound transducer with the brain surface.

In a second step, high intensity structures in the iUS data were automatically extracted using the Otsu multilevel thresholding method [33, 113]. The Otsu method is one of the better and stable thresholding algorithms, which can be reliably applied on real images. Its uniformity results in bi-level thresholding allowing one to separate the objects and background by maximizing the between class variance [114]. Multilevel thresholding segments a level gray image into several distinct homogeneous regions by increasing the number N of estimated thresholds (T_i). The quantity of segmented classes is related to the number of estimated thresholds by $N-1$. It should be noticed that N should have a moderate value in order that multi-thresholding algorithms could get reliable results. In the proposed implementation, N is not recommended to go higher than five; unfortunately, thresholding algorithms cannot automatically determine the number of thresholds [115], and the number of thresholds has to be fixed, focalizing the targeted regions.

In the 3D iB-mode images the highlighted structures are mainly borders of the resection cavity including blood and possible tumor residuals, but also blood vessels, bone structures and artifacts. In the 3D iCEUS images, they mainly consist of tumor residuals and vascular structures. The number of classes for Otsu thresholding method was experimentally set to four and three for iB-mode and iCEUS, respectively. Additionally, the voxels classified in the highest intensity class were kept as the target (i.e., tumor remnant). Lastly, a post-processing stage based on the opening filter (with structuring element of $3\times3\times1$) was applied to reduce small false positive regions detected by the algorithm. The opening operation consists of an erosion followed by a dilation step, such that $f\circ g = (f\ominus g)\oplus g$, where f is the image and g the structuring function.

For identifying suspicious brain tissue, the decision level fusion is performed based on expert knowledge. The main idea consists of selecting the structures that are enhanced in the 3D iCEUS images and that are located in the neighborhood of the cavity border as depicted in the 3D iB-mode images (Figure 4.3). This operation is performed by keeping the intersection of the segmented regions in both modalities. Let X' and Y' be the extracted structures from X and Y, respectively. With $X'\subset X$ and $Y'\subset Y$, the fused image is obtained via the decision rules described as follows:

$$Z(i,j,k) = \begin{cases} 1, & \text{if } X'(i,j,k)\cap Y'(i,j,k)\text{=1;} \\ 0, & \text{otherwise} \end{cases} \tag{4.1}$$

where $Z(i,j,k)$, $X'(i,j,k)$ and $Y'(i,j,k)$ represent the voxels of volume Z, X' and Y', respectively.

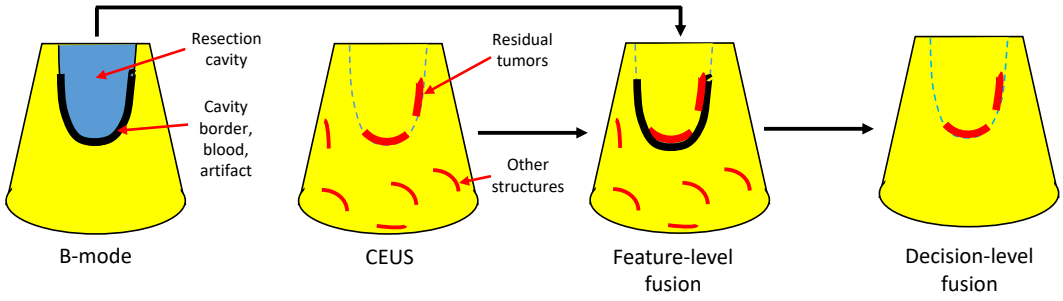

Figure 4.3: *Image fusion approach for residual brain tumor identification. The border of the resection cavity and highlighted structures are respectively extracted from B-mode and CEUS. Afterwards, they are combined on the feature-level fusion step. Finally, the expected result is obtained by selecting only specific structures based on the rules defined in the decision-level fusion step.*

4.4.3 Validation

Qualitative Validation

The brain areas' locations, automatically detected by the algorithm, are compared with the manual annotations of tumor residuals (i.e., ground truth). The following code, A/B, was used to qualitatively assess the performance of the approach. The score A provides the degree of success of the algorithm for the detection of residual tumors. A score of 1 indicates that all areas including tumor tissue were identified. A score of 0 means that a part of the total number of manually-annotated regions was detected. Additionally, a score of -1 indicates the failure of the algorithm. The second score B (-1 or 1) reveals the additional detection of false positives (FP) by the algorithm, i.e., healthy structures misclassified as remnant tumorous structures. The score of +1 indicates the presence of FP, while the value of -1 shows the absence of FP. It is noteworthy that in the case of patients without tumor residuals, the first score A is omitted. Hence:

$1\ /-1$: all tumorous regions detected;

$0\ /-1$: a part of tumor residuals detected;

$-1/-1$: detection failure;

$1\ /\ 1$: all tumorous regions detected and extra suspect regions (FP), as well;

$0\ /\ 1$: a part of tumorous structures detected and FP, as well;

$-1\ /\ 1$: extraction only of FP;

$/-1$: patient without tumor residuals and no FP detected;

$/\ 1$: patient without tumor residuals and FP extracted.

Quantitative Validation

Residuals of tumor extracted by the suggested algorithm were quantitatively compared with manual annotations considered as ground truth. Manual segmentation in the iUS data is a complex task due to the unclear representation of tumorous structure borders. Therefore, the method validation was done in two steps, namely the comparison of (1) the localization of areas containing the tumor residuals and (2) voxel classification.

First, the tumorous structures detected by the algorithm and the manual annotations were enclosed in 3D bounding boxes. The overlap coefficient ($Overlap$) of these boxes was used as a similarity measure to assess the spatial localization of tumor residuals as proposed by Dollar et al. [116]. Indeed, an $Overlap$ value of 1 is reached when one box is completely enclosed in the other one. Moreover, a value of 0 occurs when there is no intersection between both boxes. Several boxes were used when different disconnected regions were detected. The final $Overlap$ index was the average of indices calculated for each box. According to the application, this coefficient allows one to evaluate detection methods through a binary output based on a threshold value (i.e., detected or no detected). For instance, threshold values of 0.3 and 0.5 were set for target detection in [117] and [118], respectively. Thus, here, a threshold value of 0.5 has been selected for evaluating the proposed approach. The task of tumor residuals' detection was considered as succeed when $Overlap \geq 0.5$ and failed otherwise. This evaluation methodology, as illustrated in the 3D iUS images in Figure 4.4 for 3 patients (1, 6 and 16), provides information about the intersection rate between the two volume boxes. The green and red bounding boxes encompass respectively the brain areas identified by the algorithm and the ground truths. This similarity measure is described as follows:

$$Overlap = \frac{BB_{al} \cap BB_{gt}}{min(BB_{al}, BB_{gt})} \tag{4.2}$$

where BB_{al} and BB_{gt} are the bounding boxes enclosing the brain areas detected by the algorithm and those manually annotated (ground truth), respectively.

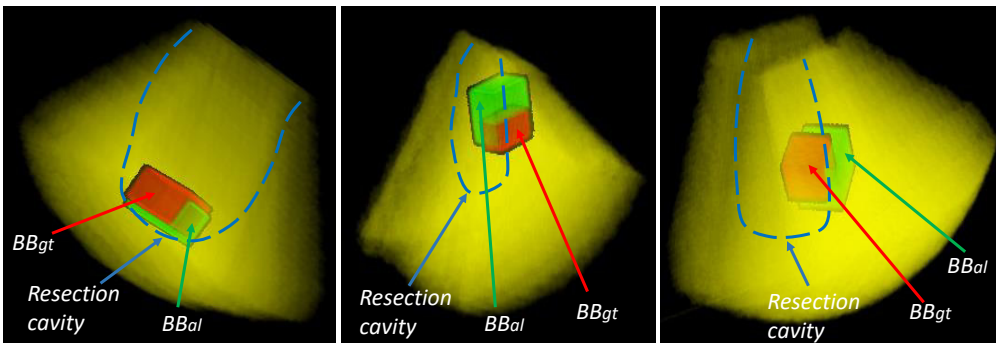

Figure 4.4: *3D representation of the quantitative evaluation approach on Patients 1, 6 and 16. BB_{al} is the algorithm result's bounding box, and BB_{gt} is the ground truth's bounding box.*

Second, the additional metrics, including accuracy (Acc), area under the ROC curve (AUC) [9] and error rate (Err) or percentage of wrong classifications [10], were calculated to evaluate the voxels classification as the tumor residual or healthy tissue by the method. This evaluation was carried out by interactively defining a region of interest enclosing the resection cavity where the remnant tumors can be found. Furthermore, these metrics were computed only for the cases where the method succeeds to identify tumor residuals based on the first quantitative metric (i.e. $Overlap \geq 0.5$). These similarity measures take values in the interval [0,1]. Acc and AUC values of 1, and Err of 0 value represent the best performance of the algorithm.

It is important to note that the Acc is correlated to the Err, but they were used for easy interpretation of the final results in term of accuracy or error rates.

4.5 Experimental Results

This section provides the evaluation results of the proposed method for automatically identifying possible brain tumor residuals. The implementation was performed with the Mevislab software development kit. The method was tested "offline" on the data of 23 patients with glioblastoma where 19 patients (Set A, Patients 1 to 19) presented tumor residuals, while no remnant tumor tissue was indicated for the remaining four patients (Set B, Patients 20 to 23).

4.5.1 Evaluation of the Influence of the Class Number in the Segmentation Step

The performance of the system is dependent on the setting of parameters such as the class number (multilevel thresholding Otsu method) and the filter window sizes in the erosion and opening operations. The influence of the class number on the segmentation results was estimated. Eight setting possibilities of class numbers were analyzed. Additionally, the notation α–β was adopted to represent the class numbers in B-mode and CEUS, respectively. Figure 4.5 shows the mean values of AUC and Acc calculated on the patient set using these eight configurations. It can be clearly observed that the highest Acc is achieved by selecting a large number of classes (e.g., 5–5). On the other hand, the highest AUC is obtained with a low number of classes (e.g., 3–2). When α and β increase, the system becomes more selective or less sensitive. This means that the probability to detect highlighted structures, including tumor residuals and other hyperechogenic structures, is reduced. On the contrary, it becomes more sensitive when α and β decrease (large values of AUC). Here, the probability to detect these highlighted structures is maximized. The first objective of the tool is rather the tumor remnants' localization and not accurate segmentation. Therefore, the optimal number of classes should be obtained when a balance between high values of both Acc and AUC is reached. A trade-off was obtained by setting α and β to the values of 4 and 3.

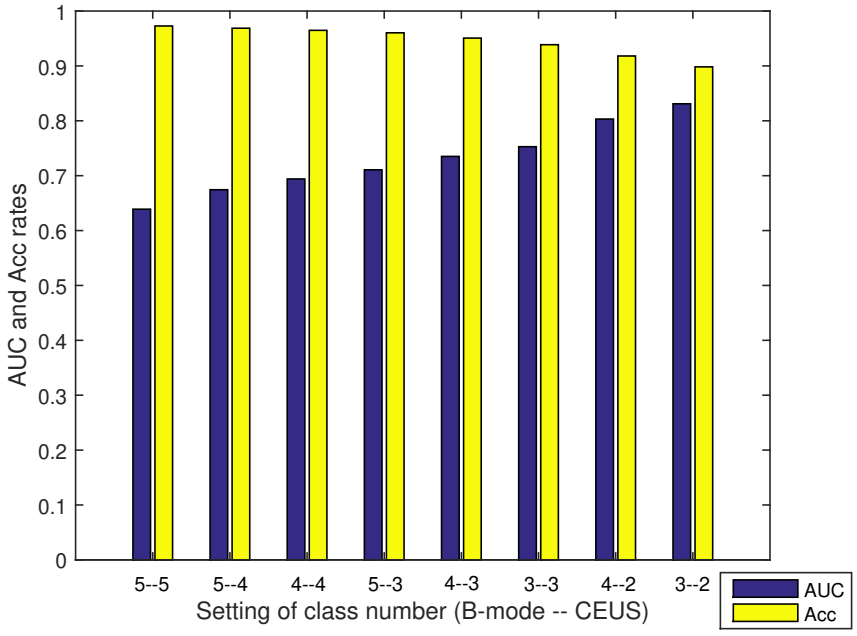

Figure 4.5: *AUC and Acc performance rates computed for several numbers of class configurations in B-mode and CEUS.*

4.5.2 Method Evaluation

The outcomes, obtained by the automatic proposed method, are presented in Figures 4.6 to 4.8. In addition, the algorithm results (in green) and the ground truths (in red) are overlaid on a selected slice of the 3D iB-mode images for visualization purposes. Table 4.1 summarizes the qualitative and quantitative evaluation. The former is based on expert observations, and the latter is performed by using the overlap, accuracy, area under the curve and error rate measures. The experiments showed that the proposed approach succeeded in detecting the position of all tumor remnant areas in 15 out of 19 patients ($Overlap \geq 0.5$). For these cases, a qualitative coding of $1/-1$ (all tumorous regions were detected) or $1/1$ (all tumorous regions were detected and extra suspected regions, as well) was observed. Regarding the four unsuccessful cases, the areas with tumorous tissue were partially detected in two patients (Patients 2 and 7, where $Overlap < 0.5$), and the algorithm failed in the two other cases (Patients 14 and 18, where $Overlap = 0$). One failure reason is the position of tumor residuals near the image top (Patients 7 and 18). These areas are removed in the preprocessing steps to eliminate artifacts caused by the US probe. The method was also tested on patient data from the set B where false positives were detected in the cases of Patients 20 and 23 and none for Patients 21 and 22.

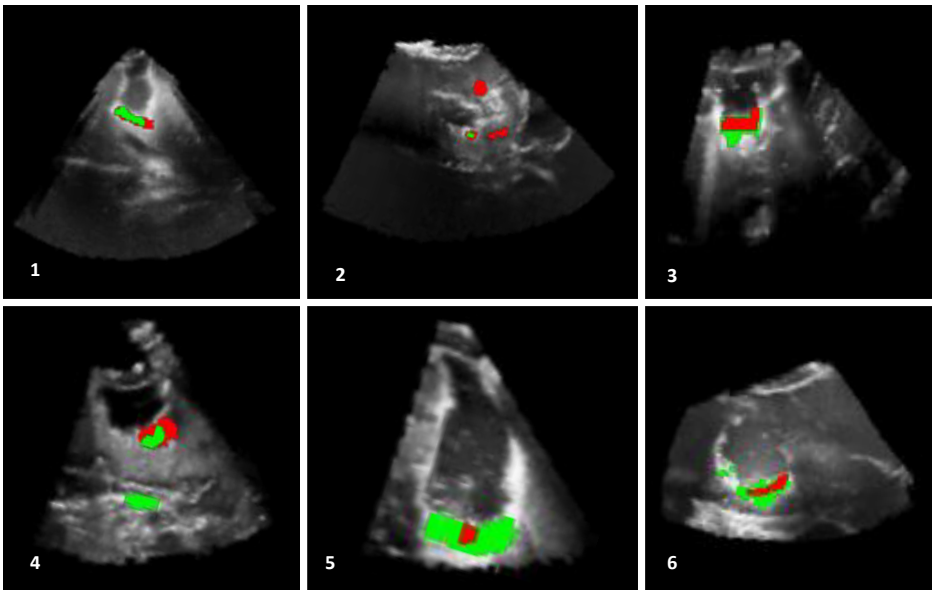

Figure 4.6: *Results of residual tumor identification from Patients 1 to 6. The results obtained with the proposed automatic method (in green) and in the manual segmentation (in red) are overlaid on a selected slice of the 3D iB-mode image data. The algorithm missed tumorous structures in Patient 2 and identified extra regions in Patient 4.*

Additionally, three cases that include false positives were found (Patients 4, 14, 18). These areas correspond to hyperechogenic structures (for example, bone and blood on the cavity border) in both iB-mode and iCEUS image data, and they are therefore extracted by the method. However, when the false positives are detected in areas far away from the resection cavity (e.g., Patients 4 and 18), these outcomes do not affect the clinical interpretation of the data because tumor residuals can be found only in the cavity.

In general, the quantitative metric used for estimating the tumor residuals' localization sustains the expert classifications. $Overlap$ values lower than 0.5 were obtained

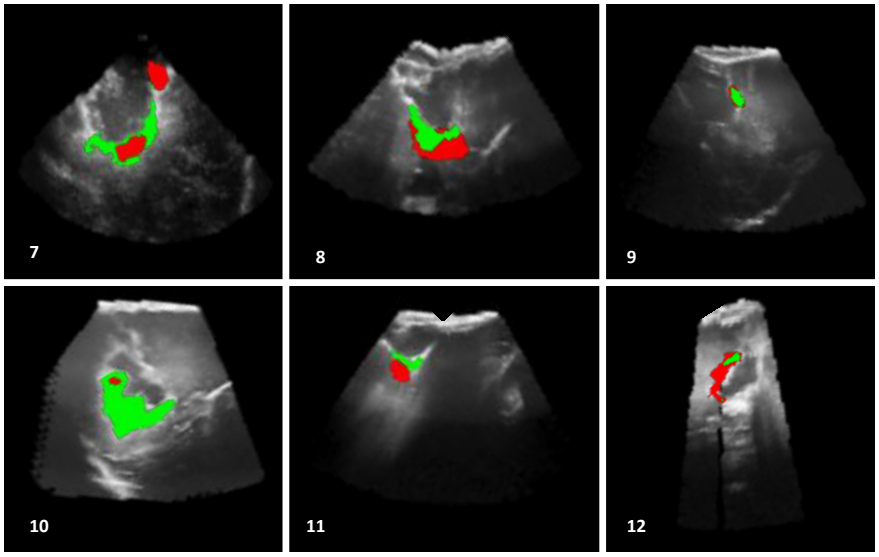

Figure 4.7: *Results of residual tumor identification from Patients 7 to 12. The results obtained by using the proposed automatic method (in green) are superimposed with the expert manual segmentation (in red). The algorithm missed the detection of other tumorous structures in the case of Patient 7, and it identified a large region in the case of Patient 10.*

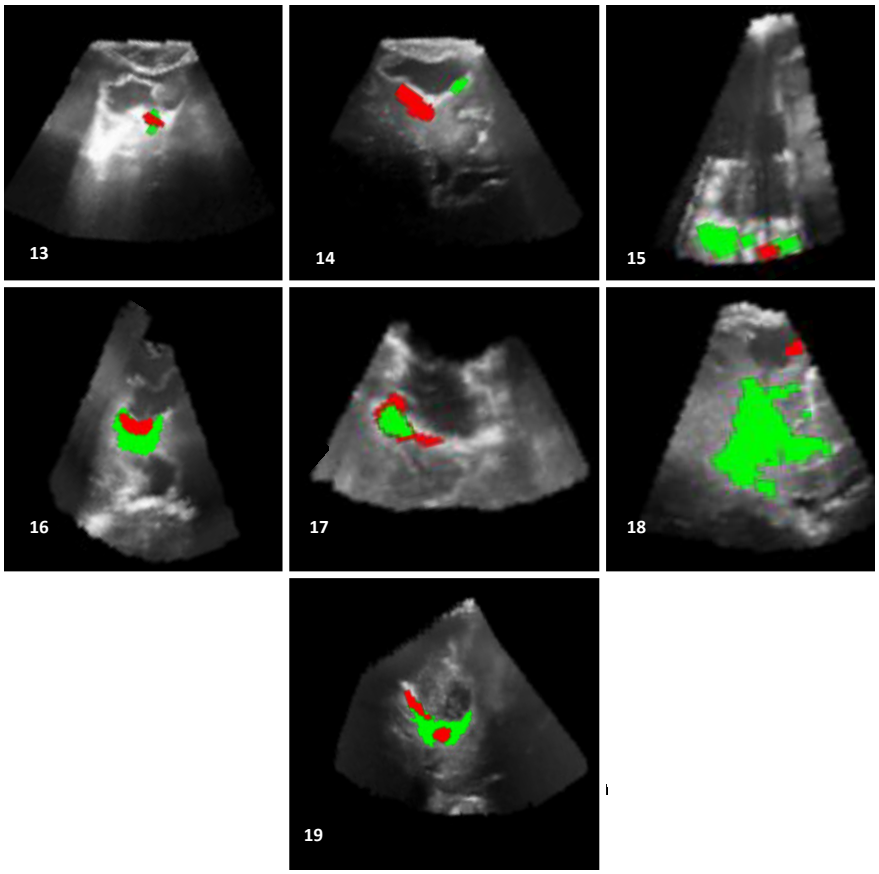

Figure 4.8: *Results of residual tumor identification from Patients 13 to 19. The results obtained by using the proposed automatic method (in green) are overlaid with the expert manual segmentation (in red). The algorithm missed completely the target in the case of Patients 14 and 18. In addition, it detected an extra region in the case of Patient 15.*

Patient	Qualitative	$Overlap$	Success	Acc	AUC	Err
1	$1/-1$	0.5307	1	0.9879	0.8405	0.0121
2	$0/-1$	0.3000	0	–	–	–
3	$1/-1$	0.6875	1	0.9795	0.899	0.0205
4	$1/1$	0.6666	1	0.9493	0.7650	0.0507
5	$1/-1$	0.7551	1	0.8105	0.8442	0.1895
6	$1/-1$	0.6913	1	0.9777	0.8803	0.0223
7	$0/-1$	0.2571	0	–	–	–
8	$1/-1$	0.8888	1	0.9618	0.6296	0.0382
9	$1/-1$	0.8500	1	0.9699	0.6642	0.0301
10	$1/-1$	1.0000	1	0.8794	0.8954	0.1206
11	$1/-1$	0.5053	1	0.9528	0.5367	0.0472
12	$1/-1$	1.0000	1	0.9522	0.5269	0.0478
13	$1/-1$	0.7173	1	0.9697	0.6257	0.0303
14	$-1/1$	0	0	–	–	–
15	$1/-1$	0.7222	1	0.9347	0.6571	0.0653
16	$1/-1$	0.7741	1	0.9864	0.7869	0.0135
17	1/-1	0.8000	1	0.9721	0.5914	0.0279
18	$-1/1$	0	0	–	–	–
19	$1/-1$	0.6464	1	0.9766	0.8837	0.0234
20	$/1$	–	–	–	–	–
21	$/-1$	–	–	–	–	–
22	$/-1$	–	–	–	–	–
23	$/1$	–	–	–	–	–

Table 4.1: *$Overlap$, accuracy (Acc), area under the curve (AUC) and error rate (Err) measures obtained from the identification of residual brain tumors by using the proposed data fusion approach. $Overlap$ values above 0.5 indicate the successful localization of the residual tumor (success = 1), and those under this threshold value mean failure (success = 0). Patients 1 to 19 presented tumor residuals, while tumor tissue was completely removed during the operation for Patients 20 to 23.*

when areas with tumor residuals were partly or not detected by the approach (Patients 2, 7, 14 and 18). However, the absolute value of the $Overlap$ coefficients does not provide a quality rate about the segmentation of tumor remnants. For instance, a value of 1 was reached for Patient 10 because the boxes were included in each other, but this case does not show the best visual result. The other metrics measure objectively the voxel classification quality. The highest accuracy values ($Acc \geq 0.97$) and lowest error rate ($Err < 0.03$) were obtained for Patients 1, 3, 6, 16, 17 and 19, because the algorithm detected correctly most of the true positives. Moreover, good accuracy scores ($0.93 \leq Acc \leq 0.96$) and error rates ($Err < 0.08$) were reached in the cases of Patients 4, 8, 9, 11, 12, 13 and 15. Additionally, the lowest scores (Acc of 0.8105 and 0.8794, Err of 0.1895 and 0.1206) were achieved for Patients 5 and 10. In addition, the AUC rates show how well true positives and false positives can be properly distinguished by the method.

The manual and quantitative validation results showed three limitations in the approach of tumor residual detection. Firstly, the current algorithm may miss residual tumors. Secondly, the algorithm extracts extra regions, which were not labeled as residual tumors by the expert. Thirdly, regions including tumor remnants segmented by the algorithm and in the ground truth have different sizes and positions. These three

points are discussed in the next paragraphs.

The method failed at identifying the residual tumors correctly in four out of 19 patients (Patients 2, 7, 14 and 18). A first reason for failing is the image quality. The approach was tested on 3D US volumes built based on acquired 2D images. The 3D reconstruction algorithm makes use of smoothing functions; therefore, hyperechogenic structures appear to have lower contrasts in the 3D volumes. Moreover, the time window of maximal contrast agent enhancement in the CEUS image data is short, and the 3D acquisition requires a couple of seconds. This maximal enhancement time point may be missed during the acquisition. This image quality drawback can be addressed by using directly raw data (2D images). However, with the current neuronavigation system used at the clinical University of Leipzig, we have only access to the 3D iUS reconstructed volume and not to the original 2D iUS data. A second reason is due to the algorithm itself. Artifacts located at the image borders are removed in the preprocessing step (Section 4.4.2). In addition, through this process, tumor areas can be lost, as well. Therefore, improvements in the pre-processing step and in the characterization of tumor residuals in the iUS images are needed.

Figure 4.9 depicts an example where extra regions, here the falx, are identified by the fusion method. These structures are obviously not tumorous tissue because they are located far from the resection cavity. Moreover, the elongated and indented shape of the extracted region is not characteristic of tumor residuals whose shape is rather compact. However, this area was enhanced in the 3D iB-mode and iCEUS image data and therefore extracted by the algorithm. A semi-automatic approach could be suggested by interactively defining a region of interest enclosing the surrounding of the resection cavity in order to limit the search volume of tumor residuals. Furthermore, Figure 4.9 gives an illustration of the results reached with the automatic and semi-automatic methods for a specific case. The first and second rows show the results obtained by using the automatic and semi-automatic methods, respectively. The automatic method result is sufficient for the neurosurgeon, because he/she refers to his knowledge to extract the correct information among the set that the algorithm suggests. Moreover, the semi-automatic process could be automated by extracting the hole of the cavity.

The quantitative evaluation showed that brain areas detected by the algorithm and segmented by the experts have different positions and sizes. The algorithm extracts essentially image regions with high intensities. On the other hand, the experts considered in addition the postoperative MR data and the radiological findings to refine the regions including tumor tissue. The extraction of additional features (e.g., texture and shape) could improve the tissue classification by using the automatic approach. In conclusion, the suggested approach is capable, at this current step, to point out suspicious brain areas in the iUS images rather than to segment the residuals of tumors. A better characterization of tumor tissue by using shape descriptors and additional intraoperative ultrasound modalities, like ultrasound perfusion, should improve the performance of automatic methods.

4.6 Conclusions

The problem of identifying the presence or the absence of residual brain tumor in iUS image data was addressed in this work. Our hypothesis is: (1) residual tumorous tissue is most of the time located beyond the borders of the resection cavity, which is well visible in B-mode modality and (2) tumor tissue is highlighted in B-mode and CEUS

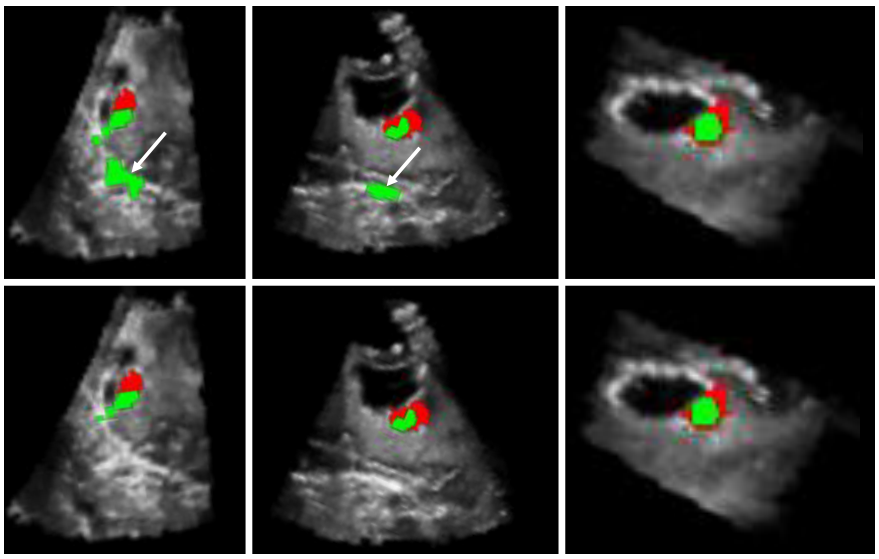

Figure 4.9: *Results of residual tumor identification from Patient 4: automatic versus semi-automatic approaches. The automatic proposed method where the white arrows show extra regions detected by the algorithm (Row 1). Correction of over residual tumor identification by using a semi-automatic method based on an ROI (Row 2). The algorithm outcomes (in green) are superimposed with the expert manual segmentation (in red).*

modalities. Firstly, the approach consists of extracting relevant information from the iUS image data. Moreover, secondly, it allows keeping possible tumor remnants using image fusion techniques. Two kinds of evaluation were performed, i.e., in terms of region localization containing the tumor residuals and in terms of the voxel being correctly classified. The experiment showed that the method was able to successfully localize brain regions, which possibly include tumor residuals for 15 out of 19 patients (Set A). Average values of the accuracy, the area under the ROC curve and the error rate were 0.9507, 0.7351 and 0.0493, respectively. A better characterization of the tumor residuals including texture descriptors, for example, and additional intraoperative ultrasound modalities should improve the performance of the new automatic approaches. Our approach represents a considerable advance in the computer-assisted surgery field for automatic detection of residual brain tumors. Nevertheless, at this stage, it is important to note that the method was tested "offline", and it is still far from clinical application. Future works will focus on method improvements and on its validation of a large patient database.

Chapter 5

General conclusions and future perspectives

This work was subdivided in three main stages. In the first part, the study was focused on the brain tumor segmentation in MR data. Alternative methods applied to brain tumor segmentation were proposed. A localized active contour model integrating an additional step of background intensity compensation (LACM-BIC) and an active contour powered by multi-population cuckoo search strategy (ACM MCSS) were introduced. Conducted experiments demonstrated that the LACM-BIC outperforms comparative methods (i.e, local binary fitting, local Gaussian distribution fitting, localized Chan-Vese and localized mean separation energy), while the ACM-MCSS achieves better results than parametric active contour driven by gradient descent and ACM guided by multi-population particle swarm optimization strategy in the second case). Specifically, it was shown that the pizza-slice shaped is preferable than rectangular shaped search window.

The second part dealt with the problem of brain tumor segmentation in US data. A method based on registration techniques was suggested. The tumor segmentation was carried out by registering the patient specific model (tumor extracted from MRI) with tumorous tissue in iUS data. Rigid and affine transformation were tested in the registration task and the results showed that they reached similar performances. This approach has proven to be effective for the improved visualization of tumor borders in iUS volumes of patients with metastasis and glioblastoma.

In the third part, the identification of tumor residuals in US data is addressed. Detection of the possible presence of residual tumors at the end of the intervention is crucial for the operation outcome. Hence, a tool for supporting physician decision about the presence or absence of residual tumor cells become imperative. To resolve this issue, a technique combining relevant information automatically extracted from intraoperative B-mode and CEUS data was proposed. The obtained results sustained that this approach was able to successfully identify areas with suspicious tissue.

Two major limitations can be found in this work, (1) brain tumor segmentation in MRI was performed by employing proposed 2D active contour models, and (2) experiments on tumor segmentation and tumor residual identification in US were conducted offline. Hence, future works could be oriented on the 3D implementation of proposed ACM and the online test of the methods in operating room. These orientation should provide useful tools for assisting neurosurgeons in clinical setting. To achieve this goal, first, a permission from an ethical comission is necessary to perform experiments. Second, the developed tools have to pass the process of certification for intraoperative

use.

Bibliography

[1] E. Ilunga-Mbuyamba, J. G. Avina?Cervantes, A. Garcia?Perez, R. de Jesus Romero?Troncoso, H. Aguirre?Ramos, I. Cruz?Aceves, and C. Chalopin, "Localized active contour model with background intensity compensation applied on automatic {MR} brain tumor segmentation," *Neurocomputing*, vol. 220, pp. 84 – 97, 2017, recent Research in Medical Technology Based on Multimedia and Pattern Recognition. [Online]. Available: http://www.sciencedirect.com/science/article/pii/S092523121630902X

[2] N. R. Pal and S. K. Pal, "A review on image segmentation techniques," *Pattern Recognition*, vol. 26, no. 9, pp. 1277 – 1294, 1993. [Online]. Available: http://www.sciencedirect.com/science/article/pii/003132039390135J

[3] F. E. Bleeker, R. J. Molenaar, and S. Leenstra, "Recent advances in the molecular understanding of glioblastoma," *Journal of Neuro-Oncology*, vol. 108, no. 1, pp. 11–27, 2012. [Online]. Available: http://dx.doi.org/10.1007/s11060-011-0793-0

[4] I. Scholl, T. Aach, T. Deserno, and T. Kuhlen, "Challenges of medical image processing," *Computer Science - Research and Development*, vol. 26, no. 1-2, pp. 5–13, 2011.

[5] E. Ilunga-Mbuyamba, J. G. Avina-Cervantes, D. Lindner, J. Guerrero-Turrubiates, and C. Chalopin, "Automatic brain tumor tissue detection based on hierarchical centroid shape descriptor in tl-weighted mr images," in *2016 International Conference on Electronics, Communications and Computers (CONIELECOMP)*, Feb 2016, pp. 62–67.

[6] E. Ilunga-Mbuyamba, J. M. Cruz-Duarte, J. G. Avina-Cervantes, C. R. Correa-Cely, D. Lindner, and C. Chalopin, "Active contours driven by cuckoo search strategy for brain tumour images segmentation," *Expert Systems with Applications*, vol. 56, pp. 59 – 68, 2016. [Online]. Available: http://www.sciencedirect.com/science/article/pii/S0957417416300872

[7] B. Menze, A. Jakab, M. Reyes, S. Bauer, M. Prastawa, and K. V. Leemput, Eds., *Proceedings of the MICCAI Challenge on Multimodal Brain Tumor Image Segmentation (BRATS) 2012*. Nice, France: MICCAI, Oct 2012. [Online]. Available: https://hal.inria.fr/hal-00912935

[8] M. Havaei, H. Larochelle, P. Poulin, and P.-M. Jodoin, "Within-brain classification for brain tumor segmentation," *International Journal of Computer Assisted Radiology and Surgery*, pp. 1–12, 2015. [Online]. Available: http://dx.doi.org/10.1007/s11548-015-1311-1

[9] M. Sokolova and G. Lapalme, "A systematic analysis of performance measures for classification tasks," *Information Processing & Management*, vol. 45, no. 4, pp. 427 – 437, 2009. [Online]. Available: //www.sciencedirect.com/science/article/pii/S0306457309000259

[10] M. J. Shafiee, P. Siva, P. Fieguth, and A. Wong, "Embedded motion detection via neural response mixture background modeling," in *2016 IEEE Conference on Computer Vision and Pattern Recognition Workshops (CVPRW)*, June 2016, pp. 837–844.

[11] S. Bauer, R. Wiest, L.-P. Nolte, and M. Reyes, "A survey of MRI-based medical image analysis for brain tumor studies," *Physics in Medicine and Biology*, vol. 58, no. 13, pp. 97 – 129, 2013.

[12] M. M. Abdelsamea, G. Gnecco, and M. M. Gaber, "An efficient self-organizing active contour model for image segmentation," *Neurocomputing*, vol. 149, Part B, pp. 820 – 835, 2015.

[13] M. Kass, A. Witkin, and D. Terzopoulos, "Snakes: Active contour models," *International Journal of Computer Vision*, vol. 1, no. 4, pp. 321–331, 1988.

[14] T. Chan and L. Vese, "Active contours without edges," *Image Processing, IEEE Transactions on*, vol. 10, no. 2, pp. 266–277, Feb 2001.

[15] S. Lankton and A. Tannenbaum, "Localizing region-based active contours," *Image Processing, IEEE Transactions on*, vol. 17, no. 11, pp. 2029–2039, Nov 2008.

[16] A. Y. Jr., A. Tsai, and A. Willsky, "A fully global approach to image segmentation via coupled curve evolution equations," *Journal of Visual Communication and Image Representation*, vol. 13, no. 1âĂŞ2, pp. 195 – 216, 2002.

[17] C. Li, C. Y. Kao, J. C. Gore, and Z. Ding, "Minimization of region-scalable fitting energy for image segmentation," *IEEE Transactions on Image Processing*, vol. 17, no. 10, pp. 1940–1949, Oct 2008.

[18] ——, "Implicit active contours driven by local binary fitting energy," in *2007 IEEE Conference on Computer Vision and Pattern Recognition*, June 2007, pp. 1–7.

[19] L. Wang, L. He, A. Mishra, and C. Li, "Active contours driven by local gaussian distribution fitting energy," *Signal Processing*, vol. 89, no. 12, pp. 2435 – 2447, 2009, special Section: Visual Information Analysis for Security.

[20] X. Xie, "Active contouring based on gradient vector interaction and constrained level set diffusion," *IEEE Transactions on Image Processing*, vol. 19, no. 1, pp. 154–164, Jan 2010.

[21] Y. Tian, F. Duan, M. Zhou, and Z. Wu, "Active contour model combining region and edge information," *Machine Vision and Applications*, vol. 24, no. 1, pp. 47–61, 2013. [Online]. Available: http://dx.doi.org/10.1007/s00138-011-0363-7

[22] L. Chen, Y. Zhou, Y. Wang, and J. Yang, "Gacv: Geodesic-aided c-v method," *Pattern Recognition*, vol. 39, no. 7, pp. 1391 – 1395, 2006. [Online]. Available: http://www.sciencedirect.com/science/article/pii/S0031320306000380

[23] H. Wang, T.-Z. Huang, Z. Xu, and Y. Wang, "A two-stage image segmentation via global and local region active contours," *Neurocomputing*, pp. – , 2016. [Online]. Available: http://www.sciencedirect.com/science/article/pii/S0925231216302600

[24] H. Zhang and X. Xie, "Divergence of gradient convolution: Deformable segmentation with arbitrary initializations," *IEEE Transactions on Image Processing*, vol. 24, no. 11, pp. 3902–3914, Nov 2015.

[25] S. Zhou, J. Wang, S. Zhang, Y. Liang, and Y. Gong, "Active contour model based on local and global intensity information for medical image segmentation," *Neurocomputing*, vol. 186, pp. 107 – 118, 2016. [Online]. Available: http://www.sciencedirect.com/science/article/pii/S0925231215020469

[26] Q. Wu, Y. Gan, B. Lin, Q. Zhang, and H. Chang, "An active contour model based on fused texture features for image segmentation," *Neurocomputing*, vol. 151, Part 3, pp. 1133 – 1141, 2015. [Online]. Available: http://www.sciencedirect.com/science/article/pii/S0925231214013526

[27] K. Zhang, H. Song, and L. Zhang, "Active contours driven by local image fitting energy," *Pattern Recognition*, vol. 43, no. 4, pp. 1199 – 1206, 2010. [Online]. Available: http://www.sciencedirect.com/science/article/pii/S0031320309003835

[28] Z. Ji, Y. Xia, Q. Sun, G. Cao, and Q. Chen, "Active contours driven by local likelihood image fitting energy for image segmentation," *Information Sciences*, vol. 301, pp. 285 – 304, 2015. [Online]. Available: http://www.sciencedirect.com/science/article/pii/S0020025515000262

[29] A. Sexton, A. Todman, and K. Woodward, "Font recognition using shape-based quad-tree and kd-tree decomposition," in *Proceedings Of The Joint Conference On Information Sciences*, vol. 5, no. 2, 2000, pp. 212 – 215.

[30] S. Armon, "Handwriting Recognition and Fast Retrieval for Hebrew Historical Manuscripts," Master's thesis, The Hebrew University of Jerusalem, 2011.

[31] D. Mumford and J. Shah, "Optimal approximations by piecewise smooth functions and associated variational problems," *Communications on Pure and Applied Mathematics*, vol. 42, no. 5, pp. 577–685, 1989. [Online]. Available: http://dx.doi.org/10.1002/cpa.3160420503

[32] S. Osher and J. A. Sethian, "Fronts propagating with curvature-dependent speed: Algorithms based on hamilton-jacobi formulations," *Journal of Computational Physics*, vol. 79, no. 1, pp. 12 – 49, 1988. [Online]. Available: http://www.sciencedirect.com/science/article/pii/0021999188900022

[33] N. Otsu, "A Threshold Selection Method from Gray-level Histograms," *IEEE Transactions on Systems, Man and Cybernetics*, vol. 9, no. 1, pp. 62–66, 1979.

[34] E. Ilunga-Mbuyamba, J. G. Avina-Cervantes, D. Lindner, J. Guerrero-Turrubiates, and C. Chalopin, "Automatic brain tumor tissue detection based on hierarchical centroid shape descriptor in tl-weighted mr images," in *2016 International Conference on Electronics, Communications and Computers (CONIELECOMP)*, Feb 2016, pp. 62–67.

[35] P. R. Jethwa, J. H. Lee, R. Assina, I. A. Keller, and S. F. Danish, "Treatment of a supratentorial primitive neuroectodermal tumor using magnetic resonance?guided laser-induced thermal therapy," *Journal of Neurosurgery: Pediatrics*, vol. 8, no. 5, pp. 468–475, 2011, pMID: 22044371. [Online]. Available: http://dx.doi.org/10.3171/2011.8.PEDS11148

[36] J. J. Corso, E. Sharon, S. Dube, S. El-Saden, U. Sinha, and A. Yuille, "Efficient multilevel brain tumor segmentation with integrated bayesian model classification," *IEEE Transactions on Medical Imaging*, vol. 27, no. 5, pp. 629–640, May 2008.

[37] L. Wang, Y. Chen, X. Pan, X. Hong, and D. Xia, "Level set segmentation of brain magnetic resonance images based on local gaussian distribution fitting energy," *Journal of Neuroscience Methods*, vol. 188, no. 2, pp. 316 – 325, 2010. [Online]. Available: http://www.sciencedirect.com/science/article/pii/S0165027010001226

[38] J. Cepeda-Negrete and R. E. Sanchez-Yanez, "Automatic selection of color constancy algorithms for dark image enhancement by fuzzy rule-based reasoning," *Applied Soft Computing*, vol. 28, pp. 1 – 10, 2015. [Online]. Available: http://www.sciencedirect.com/science/article/pii/S1568494614005961

[39] P. Du, A. Samat, B. Waske, S. Liu, and Z. Li, "Random forest and rotation forest for fully polarized {SAR} image classification using polarimetric and spatial features," *{ISPRS} Journal of Photogrammetry and Remote Sensing*, vol. 105, pp. 38 – 53, 2015. [Online]. Available: http://www.sciencedirect.com/science/article/pii/S0924271615000611

[40] P. Olofsson, G. M. Foody, M. Herold, S. V. Stehman, C. E. Woodcock, and M. A. Wulder, "Good practices for estimating area and assessing accuracy of land change," *Remote Sensing of Environment*, vol. 148, pp. 42 – 57, 2014. [Online]. Available: http://www.sciencedirect.com/science/article/pii/S0034425714000704

[41] Z. Sun, G. Bebis, and R. Miller, "Monocular precrash vehicle detection: features and classifiers," *IEEE Transactions on Image Processing*, vol. 15, no. 7, pp. 2019–2034, July 2006.

[42] X.-S. Yang and S. Deb, "Cuckoo Search via Levy flights," in *2009 World Congress on Nature & Biologically Inspired Computing (NaBIC)*. IEEE, 2009, pp. 210–214. [Online]. Available: http://ieeexplore.ieee.org/lpdocs/epic03/wrapper.htm?arnumber=5393690

[43] H. Soneji and R. C. Sanghvi, "Towards the improvement of Cuckoo search algorithm," *International Journal of Computer Information Systems and Industrial Management Applications*, vol. 6, pp. 77–88, 2014.

[44] M. Marichelvam, T. Prabaharan, and X. Yang, "Improved cuckoo search algorithm for hybrid flow shop scheduling problems to minimize makespan," *Applied Soft Computing*, vol. 19, pp. 93–101, Jun. 2014.

[45] C.-C. Tseng, J.-G. Hsieh, and J.-H. Jeng, "Active contour model via multi-population particle swarm optimization," *Expert Systems with Applications*, vol. 36, no. 3, pp. 5348 – 5352, 2009.

[46] P.-E. Danielsson, "Euclidean distance mapping," *Computer Graphics and Image Processing*, vol. 14, no. 3, pp. 227 – 248, 1980. [Online]. Available: http://www.sciencedirect.com/science/article/pii/0146664X80900544

[47] J. A. Noble and D. Boukerroui, "Ultrasound image segmentation: a survey," *IEEE Transactions on Medical Imaging*, vol. 25, no. 8, pp. 987–1010, Aug 2006.

[48] M. Xian, Y. Zhang, and H. Cheng, "Fully automatic segmentation of breast ultrasound images based on breast characteristics in space and frequency domains," *Pattern Recognition*, vol. 48, no. 2, pp. 485 – 497, 2015. [Online]. Available: http://www.sciencedirect.com/science/article/pii/S0031320314002854

[49] Q. Huang, X. Bai, Y. Li, L. Jin, and X. Li, "Optimized graph-based segmentation for ultrasound images," *Neurocomputing*, vol. 129, pp. 216 – 224, 2014. [Online]. Available: http://www.sciencedirect.com/science/article/pii/S0925231213009648

[50] Q.-H. Huang, S.-Y. Lee, L.-Z. Liu, M.-H. Lu, L.-W. Jin, and A.-H. Li, "A robust graph-based segmentation method for breast tumors in ultrasound images," *Ultrasonics*, vol. 52, no. 2, pp. 266 – 275, 2012. [Online]. Available: http://www.sciencedirect.com/science/article/pii/S0041624X11001703

[51] W. Qiu, Y. Chen, J. Kishimoto, S. de Ribaupierre, B. Chiu, A. Fenster, and J. Yuan, "Automatic segmentation approach to extracting neonatal cerebral ventricles from 3d ultrasound images," *Medical Image Analysis*, vol. 35, pp. 181 – 191, 2017. [Online]. Available: http://www.sciencedirect.com/science/article/pii/S1361841516301153

[52] Y. Yu, Y. Chen, and B. Chiu, "Fully automatic prostate segmentation from transrectal ultrasound images based on radial bas-relief initialization and slice-based propagation," *Computers in Biology and Medicine*, vol. 74, pp. 74 – 90, 2016. [Online]. Available: http://www.sciencedirect.com/science/article/pii/S001048251630110X

[53] X. Li, C. Li, A. Fedorov, T. Kapur, and X. Yang, "Segmentation of prostate from ultrasound images using level sets on active band and intensity variation across edges," *Medical Physics*, vol. 43, no. 6, pp. 3090–3103, 2016. [Online]. Available: http://dx.doi.org/10.1118/1.4950721

[54] S. Ghose, A. Oliver, J. Mitra, R. Martí, X. Lladó, J. Freixenet, D. Sidibé, J. C. Vilanova, J. Comet, and F. Meriaudeau, "A supervised learning framework of statistical shape and probability priors for automatic prostate segmentation in ultrasound images," *Medical Image Analysis*, vol. 17, no. 6, pp. 587 – 600, 2013. [Online]. Available: http://www.sciencedirect.com/science/article/pii/S1361841513000455

[55] J. Bersvendsen, F. Orderud, R. J. Massey, K. Fosså, O. Gerard, S. Urheim, and E. Samset, "Automated segmentation of the right ventricle in 3d echocardiography: A kalman filter state estimation approach," *IEEE Transactions on Medical Imaging*, vol. 35, no. 1, pp. 42–51, Jan 2016.

[56] O. Bernard, J. G. Bosch, B. Heyde, M. Alessandrini, D. Barbosa, S. Camarasu-Pop, F. Cervenansky, S. Valette, O. Mirea, M. Bernier, P. M. Jodoin, J. S. Domingos, R. V. Stebbing, K. Keraudren, O. Oktay, J. Caballero, W. Shi, D. Rueckert, F. Milletari, S. A. Ahmadi, E. Smistad, F. Lindseth, M. van Stralen, C. Wang, . Smedby, E. Donal, M. Monaghan, A. Papachristidis, M. L. Geleijnse, E. Galli, and J. D'hooge, "Standardized evaluation system for left ventricular segmentation algorithms in 3d echocardiography," *IEEE Transactions on Medical Imaging*, vol. 35, no. 4, pp. 967–977, April 2016.

[57] J. Huang, X. Yang, Y. Chen, and L. Tang, "Ultrasound kidney segmentation with a global prior shape," *Journal of Visual Communication and Image Representation*, vol. 24, no. 7, pp. 937 – 943, 2013. [Online]. Available: http://www.sciencedirect.com/science/article/pii/S1047320313001132

[58] F. Destrempes, M.-H. R. Cardinal, L. Allard, J.-C. Tardif, and G. Cloutier, "Segmentation method of intravascular ultrasound images of human coronary arteries," *Computerized Medical Imaging and Graphics*, vol. 38, no. 2, pp. 91 – 103, 2014, special Issue on Computing and Visualisation for Intravascular Imaging. [Online]. Available: http://www.sciencedirect.com/science/article/pii/S0895611113001456

[59] S. Sun, M. Sonka, and R. R. Beichel, "Graph-based ivus segmentation with efficient computer-aided refinement," *IEEE Transactions on Medical Imaging*, vol. 32, no. 8, pp. 1536–1549, Aug 2013.

[60] S. Rueda, S. Fathima, C. L. Knight, M. Yaqub, A. T. Papageorghiou, B. Rahmatullah, A. Foi, M. Maggioni, A. Pepe, J. Tohka, R. V. Stebbing, J. E. McManigle, A. Ciurte, X. Bresson, M. B. Cuadra, C. Sun, G. V. Ponomarev, M. S. Gelfand, M. D. Kazanov, C. W. Wang, H. C. Chen, C. W. Peng, C. M. Hung, and J. A. Noble, "Evaluation and comparison of current fetal ultrasound image segmentation methods for biometric measurements: A grand challenge," *IEEE Transactions on Medical Imaging*, vol. 33, no. 4, pp. 797–813, April 2014.

[61] S. Dahdouh, E. D. Angelini, G. Grangé, and I. Bloch, "Segmentation of embryonic and fetal 3d ultrasound images based on pixel intensity distributions and shape priors," *Medical Image Analysis*, vol. 24, no. 1, pp. 255 – 268, 2015. [Online]. Available: http://www.sciencedirect.com/science/article/pii/S1361841514001893

[62] F. Berton, F. Cheriet, M.-C. Miron, and C. Laporte, "Segmentation of the spinous process and its acoustic shadow in vertebral ultrasound images," *Computers in Biology and Medicine*, vol. 72, pp. 201 – 211, 2016. [Online]. Available: http://www.sciencedirect.com/science/article/pii/S0010482516300725

[63] M. Aventaggiato, F. Conversano, P. Pisani, E. Casciaro, R. Franchini, A. Lay-Ekuakille, M. Muratore, and S. Casciaro, "Validation of an automatic segmentation method to detect vertebral interfaces in ultrasound images," *IET Science, Measurement Technology*, vol. 10, no. 1, pp. 18–27, 2016.

[64] A. Müns, J. Meixensberger, S. Arnold, A. Schmitgen, F. Arlt, C. Chalopin, and D. Lindner, "Integration of a 3d ultrasound probe into neuronavigation," *Acta Neurochirurgica*, vol. 153, no. 7, pp. 1529–1533, 2011. [Online]. Available: http://dx.doi.org/10.1007/s00701-011-0994-5

[65] G. Unsgaard, T. Selbekk, T. Brostrup Müller, S. Ommedal, S. H. Torp, G. Myhr, J. Bang, and T. A. Nagelhus Hernes, "Ability of navigated 3d ultrasound to delineate gliomas and metastases – comparison of image interpretations with histopathology," *Acta Neurochirurgica*, vol. 147, no. 12, pp. 1259–1269, 2005. [Online]. Available: http://dx.doi.org/10.1007/s00701-005-0624-1

[66] N. Farhat, T. Kapur, and R. Kikinis, "Chapter 6 - role of computers and image processing in image-guided brain tumor surgery," in *Image-Guided Neurosurgery*, A. J. Golby, Ed. Boston: Academic Press, 2015, pp. 143 – 161. [Online]. Available: http://www.sciencedirect.com/science/article/pii/B9780128008706000066

[67] H. Chang, Z. Chen, Q. Huang, J. Shi, and X. Li, "Graph-based learning for segmentation of 3d ultrasound images," *Neurocomputing*, vol. 151, Part 2, pp. 632 – 644, 2015. [Online]. Available: http://www.sciencedirect.com/science/article/pii/S0925231214013873

[68] E. Hodneland, A. Lundervold, J. Rørvik, and A. Z. Munthe-Kaas, "Normalized gradient fields for nonlinear motion correction of dce-mri time series," *Computerized Medical Imaging and Graphics*, vol. 38, no. 3, pp. 202 – 210, 2014.

[69] B. Fischer and J. Modersitzki, "Ill-posed medicine?an introduction to image registration," *Inverse Problems*, vol. 24, no. 3, p. 034008, 2008.

[70] B. Fuerst, W. Wein, M. Müller, and N. Navab, "Automatic ultrasound?mri registration for neurosurgery using the 2d and 3d {LC2} metric," *Medical Image Analysis*, vol. 18, no. 8, pp. 1312 – 1319, 2014, special Issue on the 2013 Conference on Medical Image Computing and Computer Assisted Intervention.

[71] H. Rivaz, Z. Karimaghaloo, V. S. Fonov, and D. L. Collins, "Nonrigid registration of ultrasound and mri using contextual conditioned mutual information," *IEEE Transactions on Medical Imaging*, vol. 33, no. 3, pp. 708–725, March 2014.

[72] E. Hodneland, A. Lundervold, J. Rørvik, and A. Z. Munthe-Kaas, "Normalized gradient fields and mutual information for motion correction of dce-mri images," in *2013 8th International Symposium on Image and Signal Processing and Analysis (ISPA)*, Sept 2013, pp. 516–521.

[73] Z. Lai, J. Hu, C. Liu, V. Taimouri, D. Pai, J. Zhu, J. Xu, and J. Hua, "Intra-patient supine-prone colon registration in ct colonography using shape spectrum," in *Medical Image Computing and Computer-Assisted Intervention – MICCAI 2010: 13th International Conference, Beijing, China, September 20-24, 2010, Proceedings, Part I*, T. Jiang, N. Navab, J. P. W. Pluim, and M. A. Viergever, Eds. Berlin, Heidelberg: Springer Berlin Heidelberg, 2010, pp. 332–339.

[74] F. Commandeur, A. Simon, R. Mathieu, M. Nassef, J. D. Ospina, Y. Rolland, P. Haigron, R. D. Crevoisier, and O. Acosta, "Mri to ct prostate registration for improved targeting in cancer external beam radiotherapy," *IEEE Journal of Biomedical and Health Informatics*, vol. PP, no. 99, pp. 1–1, 2016.

[75] J. F. Liu, F. S. Cui, Z. J. Liu, and J. M. Liu, "A technique for prostate registration by finite element modeling," in *World Congress on Medical Physics and Biomedical Engineering, June 7-12, 2015, Toronto, Canada*, D. A. Jaffray, Ed. Cham: Springer International Publishing, 2015, pp. 870–873.

[76] H. Rivaz, Z. Karimaghaloo, V. S. Fonov, and D. L. Collins, "Nonrigid registration of ultrasound and mri using contextual conditioned mutual information," *IEEE Transactions on Medical Imaging*, vol. 33, no. 3, pp. 708–725, March 2014.

[77] R. Xu, P. Athavale, A. Nachman, and G. A. Wright, "Multiscale registration of real-time and prior mri data for image-guided cardiac interventions," *IEEE Transactions on Biomedical Engineering*, vol. 61, no. 10, pp. 2621–2632, Oct 2014.

[78] E. Haber and J. Modersitzki, "Intensity gradient based registration and fusion of multi-modal images," in *Medical Image Computing and Computer-Assisted Intervention – MICCAI 2006: 9th International Conference, Copenhagen, Denmark, October 1-6, 2006. Proceedings, Part II*, R. Larsen, M. Nielsen, and J. Sporring, Eds. Berlin, Heidelberg: Springer Berlin Heidelberg, 2006, pp. 726–733.

[79] J. Modersitzki, "Fair: Flexible algorithms for image registration." Philadelphia, PA, USA: Society for Industrial and Applied Mathematics, 2009.

[80] A. V. Moiyadi and P. Shetty, "Direct navigated 3d ultrasound for resection of brain tumors: a useful tool for intraoperative image guidance," *Neurosurgical Focus*, vol. 40, no. 3, p. E5, 2016, pMID: 26926063. [Online]. Available: http://dx.doi.org/10.3171/2015.12.FOCUS15529

[81] T. Selbekk, A. S. Jakola, O. Solheim, T. F. Johansen, F. Lindseth, I. Reinertsen, and G. Unsgård, "Ultrasound imaging in neurosurgery: approaches to minimize surgically induced image artefacts for improved resection control," *Acta Neurochirurgica*, vol. 155, no. 6, pp. 973–980, 2013. [Online]. Available: http://dx.doi.org/10.1007/s00701-013-1647-7

[82] X. Xiao, L. Dong, Q. Jiang, X. Guan, H. Wu, and B. Luo, "Incorporating contrast-enhanced ultrasound into the bi-rads scoring system improves accuracy in breast tumor diagnosis: A preliminary study in china," *Ultrasound in Medicine & Biology*, vol. 42, no. 11, pp. 2630–2638, 2016. [Online]. Available: http://www.sciencedirect.com/science/article/pii/S0301562916301648

[83] N. Masumoto, T. Kadoya, A. Amioka, K. Kajitani, H. Shigematsu, A. Emi, K. Matsuura, K. Arihiro, and M. Okada, "Evaluation of malignancy grade of breast cancer using perflubutane-enhanced ultrasonography," *Ultrasound in Medicine & Biology*, vol. 42, no. 5, pp. 1049–1057, 2016. [Online]. Available: http://www.sciencedirect.com/science/article/pii/S0301562916000089

[84] M. Friedrich-Rust, T. Klopffleisch, J. Nierhoff, E. Herrmann, J. Vermehren, M. D. Schneider, S. Zeuzem, and J. Bojunga, "Contrast-enhanced ultrasound for the differentiation of benign and malignant focal liver lesions: a meta-analysis," *Liver International*, vol. 33, no. 5, pp. 739–755, 2013. [Online]. Available: http://dx.doi.org/10.1111/liv.12115

[85] T. Kim and H. Jang, "Contrast-enhanced ultrasound in the diagnosis of nodules in liver cirrhosis," *World J Gastroenterol*, vol. 13, no. 20, pp. 3590–3596, 2014.

[86] R. G. Barr, C. Peterson, and A. Hindi, "Evaluation of indeterminate renal masses with contrast-enhanced us: A diagnostic performance study," *Radiology*, vol. 271, no. 1, pp. 133–142, 2014, pMID: 24475802. [Online]. Available: http://dx.doi.org/10.1148/radiol.13130161

[87] Y. Cai, L. Du, F. Li, J. Gu, and M. Bai, "Quantification of enhancement of renal parenchymal masses with contrast-enhanced ultrasound," *Ultrasound in Medicine & Biology*, vol. 40, no. 7, pp. 1387–1393, 2014. [Online]. Available: http://www.sciencedirect.com/science/article/pii/S0301562914000763

[88] S. Houtzager, H. Wijkstra, J. J. M. C. H. de la Rosette, and M. P. Laguna, "Evaluation of renal masses with contrast-enhanced ultrasound," *Current Urology Reports*, vol. 14, no. 2, pp. 116–123, 2013. [Online]. Available: http://dx.doi.org/10.1007/s11934-013-0309-x

[89] E. Ilunga-Mbuyamba, J. G. Avina-Cervantes, D. Lindner, I. Cruz-Aceves, F. Arlt, and C. Chalopin, "Vascular structure identification in intraoperative 3d contrast-enhanced ultrasound data," *Sensors*, vol. 16, no. 4, pp. 497,1–14, 2016. [Online]. Available: http://www.mdpi.com/1424-8220/16/4/497

[90] F. Prada, M. Del Bene, M. Saini, P. Ferroli, and F. DiMeco, "Intraoperative cerebral angiosonography with ultrasound contrast agents: how i do it," *Acta Neurochirurgica*, vol. 157, no. 6, pp. 1025–1029, 2015. [Online]. Available: http://dx.doi.org/10.1007/s00701-015-2412-x

[91] C. Chalopin, K. Krissian, J. Meixensberger, A. Müns, F. Arlt, and D. Lindner, "Evaluation of a semi-automatic segmentation algorithm in 3d intraoperative ultrasound brain angiography," *Biomedizinische Technik/ Biomedical Engineering*, vol. 58, no. 3, pp. 293–302., Jun 2013.

[92] W. He, X.-Q. Jiang, S. Wang, M. zhi Zhang, J. zong Zhao, H. zhao Liu, J. Ma, D. ying Xiang, and L. shu Wang, "Intraoperative contrast-enhanced ultrasound for brain tumors," *Clinical Imaging*, vol. 32, no. 6, pp. 419–424, 2008. [Online]. Available: http://www.sciencedirect.com/science/article/pii/S0899707108001939

[93] F. Prada, A. Perin, A. Martegani, L. Aiani, L. Solbiati, M. Lamperti, C. Casali, F. Legnani, L. Mattei, A. Saladino, M. Saini, and F. Dimeco, "Intraoperative contrast-enhanced ultrasound for brain tumor surgery," *Neurosurgery*, vol. 74, no. 5, pp. 542–552, 2014.

[94] K. Ritschel, I. Pechlivanis, and S. Winter, "Brain tumor classification on intraoperative contrast-enhanced ultrasound," *International Journal of Computer Assisted Radiology and Surgery*, vol. 10, no. 5, pp. 531–540, 2015. [Online]. Available: http://dx.doi.org/10.1007/s11548-014-1089-6

[95] F. Arlt, C. Chalopin, A. Müns, J. Meixensberger, and D. Lindner, "Intraoperative 3d contrast-enhanced ultrasound (ceus): a prospective study of 50 patients with brain tumours," *Acta Neurochirurgica*, vol. 158, no. 4, pp. 685–694, 2016. [Online]. Available: http://dx.doi.org/10.1007/s00701-016-2738-z

[96] F. Prada, M. D. Bene, R. Fornaro, I. G. Vetrano, A. Martegani, L. Aiani, L. M. Sconfienza, G. Mauri, L. Solbiati, B. Pollo, and F. DiMeco, "Identification of residual tumor with intraoperative contrast-enhanced ultrasound during glioblastoma resection," *Neurosurgical Focus*, vol. 40, no. 3, p. E7, 2016, pMID: 26926065. [Online]. Available: http://dx.doi.org/10.3171/2015.11.FOCUS15573

[97] G. Piella, "A general framework for multiresolution image fusion: from pixels to regions," *Information Fusion*, vol. 4, no. 4, pp. 259–280, 2003. [Online]. Available: http://www.sciencedirect.com/science/article/pii/S1566253503000460

[98] J. Ma, C. Chen, C. Li, and J. Huang, "Infrared and visible image fusion via gradient transfer and total variation minimization," *Information Fusion*, vol. 31, pp. 100–109, 2016. [Online]. Available: http://www.sciencedirect.com/science/article/pii/S156625351630001X

[99] C. Han, H. Zhang, C. Gao, C. Jiang, N. Sang, and L. Zhang, "A remote sensing image fusion method based on the analysis sparse model," *IEEE Journal of Selected Topics in Applied Earth Observations and Remote Sensing*, vol. 9, no. 1, pp. 439–453, Jan 2016.

[100] H. Ghassemian, "A review of remote sensing image fusion methods," *Information Fusion*, vol. 32, Part A, pp. 75–89, 2016. [Online]. Available: http://www.sciencedirect.com/science/article/pii/S1566253516300173

[101] Z. Lu, X. Jiang, and A. C. Kot, "A color channel fusion approach for face recognition," *IEEE Signal Processing Letters*, vol. 22, no. 11, pp. 1839–1843, Nov 2015.

[102] C. Chen, R. Jafari, and N. Kehtarnavaz, "Improving human action recognition using fusion of depth camera and inertial sensors," *IEEE Transactions on Human-Machine Systems*, vol. 45, no. 1, pp. 51–61, Feb 2015.

[103] G. Bhatnagar, Q. J. Wu, and Z. Liu, "A new contrast based multimodal medical image fusion framework," *Neurocomputing*, vol. 157, pp. 143–152, 2015. [Online]. Available: http://www.sciencedirect.com/science/article/pii/S0925231215000466

[104] X. Liu, W. Mei, and H. Du, "Multimodality medical image fusion algorithm based on gradient minimization smoothing filter and pulse coupled neural network," *Biomedical Signal Processing and Control*, vol. 30, pp. 140–148, 2016. [Online]. Available: http://www.sciencedirect.com/science/article/pii/S1746809416300659

[105] S. Das and M. K. Kundu, "A neuro-fuzzy approach for medical image fusion," *IEEE Transactions on Biomedical Engineering*, vol. 60, no. 12, pp. 3347–3353, Dec 2013.

[106] Z. Zhu, Y. Chai, H. Yin, Y. Li, and Z. Liu, "A novel dictionary learning approach for multi-modality medical image fusion," *Neurocomputing*, vol. 214, pp. 471–482, 2016. [Online]. Available: http://www.sciencedirect.com/science/article/pii/S0925231216306749

[107] G. Bhatnagar, Q. M. J. Wu, and Z. Liu, "Directive contrast based multimodal medical image fusion in nsct domain," *IEEE Transactions on Multimedia*, vol. 15, no. 5, pp. 1014–1024, Aug 2013.

[108] X. Xu, D. Shan, G. Wang, and X. Jiang, "Multimodal medical image fusion using pcnn optimized by the qpso algorithm," *Applied Soft Computing*, vol. 46, pp. 588–595, 2016. [Online]. Available: http://www.sciencedirect.com/science/article/pii/S1568494616301570

[109] C. Kavitha and C. Chellamuthu, "Medical image fusion based on hybrid intelligence," *Applied Soft Computing*, vol. 20, pp. 83–94, 2014, hybrid intelligent methods for health technologies. [Online]. Available: http://www.sciencedirect.com/science/article/pii/S1568494613004043

[110] S. F. Nemec, M. A. Donat, S. Mehrain, K. Friedrich, C. Krestan, C. Matula, H. Imhof, and C. Czerny, "Ct?mr image data fusion for computer assisted navigated neurosurgery of temporal bone tumors," *European Journal of Radiology*, vol. 62, no. 2, pp. 192 – 198, 2007, update in Small Bowel and Abdominal Imaging. [Online]. Available: http://www.sciencedirect.com/science/article/pii/S0720048X06005171

[111] F. Prada, M. Del Bene, L. Mattei, C. Casali, A. Filippini, F. Legnani, A. Mangraviti, A. Saladino, A. Perin, C. Richetta, I. Vetrano, A. Moiraghi, M. Saini, and F. DiMeco, "Fusion imaging for intra-operative ultrasound-based navigation in neurosurgery," *Journal of Ultrasound*, vol. 17, no. 3, pp. 243–251, 2014. [Online]. Available: http://dx.doi.org/10.1007/s40477-014-0111-8

[112] H. K. Inoue, A. Nakajima, H. Sato, S. Noda, J. Saitoh, and Y. Suzuki, "Image fusion for radiosurgery, neurosurgery and hypofractionated radiotherapy," *Cureus*, vol. 7, no. 3, 2015.

[113] N. Hui-Fuang, "Automatic thresholding for defect detection," *Pattern Recognition Letters*, vol. 27, no. 14, pp. 1644–1649, 2006. [Online]. Available: http://www.sciencedirect.com/science/article/pii/S016786550600119X

[114] P. K. Sahoo, S. Soltani, A. K. Wong, and Y. C. Chen, "A survey of thresholding techniques," *Comput. Vision Graph. Image Process.*, vol. 41, no. 2, pp. 233–260, feb 1988. [Online]. Available: http://dx.doi.org/10.1016/0734-189X(88)90022-9

[115] S. Arora, J. Acharya, A. Verma, and P. K. Panigrahi, "Multilevel thresholding for image segmentation through a fast statistical recursive algorithm," *Pattern Recognition Letters*, vol. 29, pp. 119–125, 2008.

[116] P. Dollar, Z. Tu, P. Perona, and S. Belongie, "Integral channel features," in *Proc. BMVC*, 2009, pp. 91.1–91.11, doi:10.5244/C.23.91.

[117] I. Cherif, V. Solachidis, and I. Pitas, *A Tracking Framework for Accurate Face Localization*. Boston, MA: Springer US, 2006, pp. 385–393. [Online]. Available: http://dx.doi.org/10.1007/978-0-387-34747-9_40

[118] M. Everingham, S. M. A. Eslami, L. Van Gool, C. K. I. Williams, J. Winn, and A. Zisserman, "The pascal visual object classes challenge: A retrospective," *International Journal of Computer Vision*, vol. 111, no. 1, pp. 98–136, 2015. [Online]. Available: http://dx.doi.org/10.1007/s11263-014-0733-5